الجمهورية الجزائرية الديمقراطية الشعبية
République Algérienne Démocratique et Populaire
وزارة التعليم العالي والبحث العلمي
Ministère de l'enseignement supérieur et de la recherche scientifique

Université Mohamed Khider – Biskra
Faculté des Sciences et de la technologie
Département de Génie Electrique
Ref :

جامعة محمد خيضر بسكرة
كلية العلوم والتكنولوجيا
قسم: الهندسة الكهربائية
المرجع : 2023./

Thèse présentée en vue de l'obtention
Du diplôme de

Doctorat LMD

Spécialité : Génie Electrique

Option

Energie renouvelable et photovoltaïque

Contribution à l'amélioration des performances d'un système de dessalement d'eau alimenté par une source photovoltaïque

Présentée par :

BOUKAHIL Fatima Zohra

Soutenue publiquement le …/…/2023.

Devant le jury composé de :

Dr. GHAMRI Ahmed	Professeur	Université de Biskra	Président
Dr. ABDEDDAIM Sabrina	Professeur	Université de Biskra	Rapporteur
Dr. DRID Said	Professeur	Université de Batna	Examinateur
Dr. GOLEA Amar	Professeur	Université de Biskra	Examinateur
Dr. BETKA Achour	Professeur	Université de Biskra	invité
Dr. CHAROUF Omar	Maitre de Conférences MCA	Université de Biskra	invité

الجمهورية الجزائرية الديمقراطية الشعبية
People's Democratic Republic of Algeria
وزارة التعليم العالي والبحث العلمي
Ministry Of Higher Education & Scientific Research

University Mohamed Khider – Biskra
Faculty of Science and Technology
Department of Electrical Engineering
Ref :

جامعة محمد خيضر بسكرة
كلية العلوم والتكنولوجيا
قسم: الهندسة الكهربائية
المرجع :   2023./

A thesis submitted for the fulfillment of

The degree of

Doctorate in Electrical Engineering

The thesis has been prepared in the Electrical Engineering Laboratory of Biskra LGEB

Option

Renewable energy and photovoltaic

Contribution to the improvement of the performance of a water desalination system powered by a photovoltaic source

Présentée par :

Fatima Zohra BOUKAHIL

The public thesis defense on: …/…/2023.

Board of Examiners :

Dr. GHAMRI Ahmed	Professor	University of Biskra	Chairman
Dr. ABDEDDAIM Sabrina	Professor	University of Biskra	Supervisor
Dr. DRID Said	Professor	University of Batna	Examiner
Dr. GOLEA Amar	Professor	University of Biskra	Examiner
Dr. BETKA Achour	Professor	University of Biskra	Guest
Dr. CHAROUF Omar	Lecturer ‘MCA’	University of Biskra	Guest

ملخص

تقدم هذه الرسالة دراسة تهدف إلى تحسين كفاءة نظام تحلية المياه باستخدام مصدر ضوئي. تم تحقيق هذا التحسن من خلال تطبيق DTC

على جانب مضخة المحرك وعلى الجانب الكهروضوئي تطبيق ESC في ظل ظروف مناخية صحية ومظللة.

تضمنت الدراسة تصميم وتنفيذ نموذج أولي لنظام تحلية المياه يستخدم مصدر طاقة كهروضوئية. تم تقييم أداء النظام من خلال قياس معدل رفض الملح واستهلاكه النوعي للطاقة. أظهرت النتائج أن زيادة تدفق المياه قليلة الملوحة وتحسين عناصر التحكم على جانب الطاقة الكهروضوئية وجانب المضخة الحركية أدى إلى تحسن كبير في أداء النظام.

وخلصت الدراسة إلى أن استخدام مصدر الطاقة الكهروضوئية لنظام تحلية المياه هو نهج واعد لمواجهة تحديات ندرة المياه، خاصة في المناطق التي لا تتوفر فيها الكهرباء بسهولة. يمكن أن يقلل هذا النهج من البصمة الكربونية المرتبطة بالطرق التقليدية لتحلية المياه ويكون له تأثير إيجابي على البيئة. يوفر البحث رؤى قيمة لتصميم وتحسين أنظمة تحلية المياه التي تعمل بالطاقة الكهروضوئية، مما يساهم في الإدارة المستدامة لموارد المياه.

الكلمات المفتاحية:

، التحكم في البحث عن (MPPT) تحلية المياه، المولد الكهروضوئي ، محول التيار المستمر، تتبع نقطة الطاقة القصوى ، والتظليل ، ووحدة التحكم في الوضع الانزلاقي ، والتناضح العكسي الطاقة القصوى

Résumé

Cette thèse présente une étude visant à améliorer l'efficacité d'un système de dessalement d’eau en utilisant une source photovoltaïque. Cette amélioration a été réalisée en appliquant l’ESC côté PV, la DTC 12 sectors côté motopompe et l'optimisation côté membrane dans des conditions climatiques saines et ombragées.

L'étude a impliqué la conception et la mise en œuvre d’un prototype de système de dessalement d'eau qui utilise une source d'énergie photovoltaïque. Les performances du système ont été évaluées en mesurant son taux de rejet de sel et sa consommation d'énergie spécifique. Les résultats ont montré que l'augmentation du débit d'eau saumâtre et l'amélioration des contrôles sur le côté PV et motopompe a considérablement amélioré les performances du système.

L'étude a conclu que l'utilisation d'une source d'énergie photovoltaïque pour un système de dessalement de l'eau est une approche prometteuse pour répondre aux défis de la pénurie d'eau, en particulier dans les zones où l'électricité n'est pas facilement disponible. Cette approche peut réduire l'empreinte carbone associée aux méthodes traditionnelles de dessalement de l'eau et avoir un impact positif sur l'environnement. La recherche fournit des indications précieuses pour la conception et l'optimisation des systèmes de dessalement d'eau alimentés par l'énergie photovoltaïque, contribuant à la gestion durable des ressources en eau.

Mots-clés :

Générateur photovoltaïque, convertisseur DC-DC, MPPT, ESC, MATLAB/Simulink, PO, bus continu, Osmose Inverse (OI), Commande directe du couple (DTC), Dspace 1104.

Abstract

This thesis presents a study aimed at improving the efficiency of a water desalination system using a photovoltaic source. This improvement was achieved by applying Extremum Seeking Control (ESC) on the PV side, DTC 12 vector on the motor pump side, and optimizing the membrane side under healthy and shaded weather conditions.

The study involved designing and implementing a prototype water desalination system that utilizes a photovoltaic power source. The system's performance was evaluated by measuring its salt rejection rate and specific energy consumption. The results showed that increasing the flow rate of brackish water and improving the controls on the PV and moto-pump side significantly improved the system's performance.

The study concluded that using a photovoltaic power source for a water desalination system is a promising approach to address water scarcity challenges, especially in areas where electricity is not readily available. This approach can reduce the carbon footprint associated with traditional water desalination methods and have a positive impact on the environment. The research provides valuable insights for the design and optimization of photovoltaic-powered water desalination systems, contributing to the sustainable management of water resources.

Key-words:

Desalination, Photovoltaic generator, DC-DC converter, Maximum power point tracking (MPPT), Extremum Seeking Control (ESC), MATLAB/Simulink, Perturb and Observe (PO), sliding mode controller, Reverse Osmosis (RO), shading, DTC (12 vectors), Linear Quadrature Regulator (LQR), Dspace 1104.

….ACKNOWLEDGMENTS

ACKNOWLEDGMENTS

This thesis becomes a reality with the kind support of many individuals. I would like to extend my sincere thanks to all of them.

Foremost, I would like to thank the almighty ***Allah*** *for the wisdom he bestowed upon me, empowering and giving me the internal courage and strength to accomplish this research.*

I owe to express my sincere gratitude to my esteemed supervisor ***Professor Sabrina Abdeddaim*** *for her kind and continuous support in providing technical and scientific guidance throughout this research.*

I would like to express my thanks to everyone that makes achieved this work. My great gratitude goes to ***Dr. Omar Charrouf****,* ***Dr. Abdelkrim Menadi****, and* ***Pr. Achour Betka*** *members of the electrical engineering laboratory of Biskra LGEB, and* ***Pr. Amar Golea****,* ***Pr. Med Toufik Benchouia****, and* ***Dr. Mohamed Chebaani*** *for their continuous support, guidance, and encouragement throughout my project, extensive knowledge, and diligent work. It has been also a great honor and real pleasure to work under their supervision, as they were generous with their expertise and friendly to work together.*

I want to express my special appreciation to ***Pr. Zouzou Salaheddine*** *the Head of the electrical engineering laboratory of Biskra (LGEB) for providing the appropriate environment for research and experimental work in the laboratory.*

I also address my sincere thanks to ***Mehdi TURKI****, a permanent researcher at the Laboratory of Electrical Systems (LSE) at ENIT and assistant professor at the Higher School of Engineering of Medjez el Bab, University of Jendouba, Tunisia.*

Further, I thank the members of LGEB and my colleagues' Ph.D. students. It was great to share the laboratory with all of you during the last five years. I would particularly like to thank while expressing my deep gratitude to ***Mrs. Meriem Saadi*** *Engineer of the Lab LGEB, for her encouragement and assistance. In addition, I also thank* ***Abdelali Lamri****.*

Finally, I am grateful to my mother for her prayers, guidance, and support throughout my education. Her inspiration and encouragement have been invaluable.

Fatima Zohra Boukahil

Dedication

I dedicate this thesis to my mother "Aziza Benbedia" who has taken the biggest part in sacrificing for my education, may Allah protect her. I also dedicate it to all my friends, in my social and academic life.

I do not forget to dedicate this work to Ikram and her mother, May God protects her.

Fatima Zohra Boukahil

إهداء

أهدي هذا العمل إلى والدتي "بن كدية عزيزة " التي كان لها النصيب الأكبر من التضحيات من اجل تربيتي وتعليمي، اسال الله العظيم ان يحفظها.

أهدي هذا العمل أيضا الي مرزوق احمد

أهدي هذا العمل أيضا الي جميع أصدقائي في حياتي الاجتماعية والأكاديمية.

أهدي هذا العمل أيضا لإكرام ووالدتها حفظها الله.

بوكحيل فاطمة الزهراء

List of Publications Related to the Thesis

Journal Publications

1. **Boukahil, Fatima Zohra**, et al. "The Shading Effect on Photovoltaic Generator (GPV) Based on Reverse Osmosis (RO) Desalination System in Algeria." European Journal of Electrical Engineering 24.4 (2022): 185.

2. **Boukahil, F. Z.**, et al. "Experimental validation of Extremum Seeking and Sliding Model-based Control for an Autonomous PV System under partial shading conditions." Journal of Electrical Systems 18.4 (2022): 520-532.

Conferences

1. **Fatima Zohra Boukahil,** S.Abdedaim, O. Charrouf, A.Betka, "Comparative study between the vector control with PI regulator and second order sliding mode for speed control to improve the electrical performance of the PMSM". The 2nd International Conference on Electrical Engineering (ICEE-B) December 2018, Biskra, Algerie.

2. **Fatima Zohra Boukahil**, S.Abdedaim, O. Charrouf, A.Betka, "Brackish water desalination by renewable energy“. Participation in AAF Summer University August 2019, Batna

3. **Fatima Zohra Boukahil**, S.Abdedaim, O. Charrouf, A.Betka, A.Menadi, "Implementation and simulation of sliding mode control for PV system“. International Conference on Energy, Materials, Applied Energetics and Pollution, ICEMAEP 2019, October 22-24, 2019, Constantine, Algeria.

4. **Fatima Zohra Boukahil**, S.Abdedaim, O. Charrouf, A.Betka, M.Sellali, "Comparative study of maximum power point tracking algorithms using Matlab/Simulink for PV system“. International Conference ICEREGA 2019, Istanbul, Turkey. 28-30 October 2019.

5. **Fatima Zohra Boukahil**, Participate in the American University in Cairo, March 2022.

6. **Fatima Zohra Boukahil**, "40 training hours in Advanced training in renewable energies“. Certificate from Cambridge Academy June 2022

List of Figures

List of figures:

Chapter 1

Chapter 2

Chapter 3

Chapter 4

Chapter 5

List of tables

Chapter 1

Chapter 2

Chapter 3

Chapter 4

Nomenclature

Chapter 1

MSF: Multi-Stage Flash distillation.

MED: Multi-Effects distillation.

VC: Vapor Compression.

MVC: Mechanical Vapor Compression.

TVC: Thermo Vapor Compression.

ED: Electro-Dialysis.

RO: Reverse Osmosis.

SWRO: Seawater Reverse Osmosis.

BWRO: Brackish Water Reverse Osmosis.

WES: Wind Energy System.

Chapter 2

I_{PV}**:** Photovoltaic generator current (A)

V_{PV}**:** Photovoltaic generator voltage (V)

P_{PV}: Photovoltaic generator power (W)

I_{ph}**:** Photocurrent (A)

I_o**:** Reverse saturation current (A)

V_{th} **:** Thermal voltage (V)

I_{op} **:** Optimal current of the photovoltaic generator (A)

V_{op}**:** Optimal voltage of the photovoltaic generator (V)

V_{oc}: Open circuit voltage of the photovoltaic generator (V)

I_{sc}: Photovoltaic short circuit (A).

n_s: Cellule numbers

N_s, N_p: Series and shunt panel numbers.

R_s, R_p: array series, shunt resistance (Ω)

T, T_{ref}: Cell temperature (°C)

E, E_r: measured and referenced solar irradiance (W/m²)

I_{pvG}: Array output current (A).

V_{pvG}: Array output voltage (V).

V_{mpp}: Optimal voltage of the photovoltaic generator (V).

P_{mpp}: Optimal power of the photovoltaic generator (W).

MPPT: Maximum Power Point Tracking

q: Electronic charge$(1.6 \times 10^{-19}\ \mathrm{C})$

γ : Temperature coefficient of the photo-current (mA/°C)

β : Temperature coefficient of the open circuit voltage (mV/°C)

Kb: Boltzmann constant$(\mathbf{1.38 \times 10^{-23}\ J/K})$.

A: diode ideality factor $(\mathbf{1} < \boldsymbol{A} < \mathbf{5})$.

K_{nacl}: Osmotic constant

C: DC bus capacitor

D: Parallel chopper diode

L: Parallel chopper input inductance.

S: Parallel chopper switch

I_D: Diode current (A).

I_C: Current of the DC bus capacity (A)

I_L: Inductance current at the input of the parallel chopper (A)

V_{DC}, V_{DC-ref}: DC bus voltage and its reference (V)

I_{PVs}: Current at the output of the parallel chopper (A)

I_{inv}: Inverter input current (A)

I_a, I_b, I_c: Inverter output currents (A)

P_{dc}: DC bus power (W)

R_L: Load resistance (Ω)

I_d, I_q: The d-q transformation of inverter output current (A).

V_d , V_q: d-q transformation of inverter output voltage (V)

V_a , V_b, V_c : Inverter output voltages (V)

F_1, F_2, F_3: Switching states of the inverter switches

α: The duty cycle of the parallel chopper.

T_{nacl}: concentrated solution temperature (°C)

C_{nacl}: Salt concentration in the water to be desalinated (mg/l)

Pf, Pp: feed and permeate water pressure (bar)

Q_f, Q_p: feed and permeate water flow (l/min)

A: water permeability coefficient.

R: Recovery (%).

Chapter 3

MPP: Maximum Power Point.

GMPP: Global maximum Power Point.

LMPP: Local maximum Power Point.

UIC: Uniform Irradiance Conditions.

PSC: Partially Shaded Conditions.

PO or P&O: Perturb and Observe.

ESC: Extremum Seeking Control.

SMC: Sliding Mode Control.

SM-ESC: Sliding Mode-Extremum Seeking Control.

SM-ESC-mod: Sliding Mode-Extremum Seeking Control-modified.

ANN: Artificial Neural Networks.

GA: Genetic Algorithm.

GWO: Gray Wolf Optimisation.

PSO: Particle Swarm Optimization.

α: The duty cycle of the parallel chopper.

S: Sliding surface of the MPPT by the sliding mode.

Kmcc: The control gain of the sliding mode control.

HPF: High Pass Filter.

LPF: Low Pass Filter.

P_{max}: Maximum power (W).

Chapter 4

PVG: Photovoltaic generator.

DTC: Direct Torque Control.

ESC: Extremum Seeking Control.

RO: Reverse Osmosis.

TIADS: Technical Institute for Agricultural Development in the South.

e: The tracking error.

V_{DC}, V^*_{DC}: DC bus voltage and its reference (V)

PI: Proportional Integrator.

Te: Estimated torque.

IT/DT: Torque large increase/decrease.

sIT/sDT: Torque small increase/decrease.

IF/DF: Flux large increase/decrease.

WQL: Water Quantity Losses.

PWQ: Permeate Water Quantity.

FWQ: Feed Water Quantity.

E: Solar irradiance (W/m2).

Ppv: Photovoltaic power (W).

Pf: Feed water pressure (bar).

Qf: Feed water flow (l/min).

Qp: Freshwater flow (l/min).

R: Recovery (%).

Chapter 5

IM: Induction Machine.

LQR: Linear Quadratic Regulator.

LGEB: Laboratory of Electrical Engineering of Biskra.

STC: Standard Test Conditions.

HP: High-pressure pump.

MIMO: Multi-Input Multi-Output.

Pf: Feed water pressure (bar).

Pp: Permeate pressure (bar).

Qp: Freshwater flow (l/min).

Qf/Qb: Brine or feed flow rate (l/min).

Cp: Permeate conductivity.

TABLE of Contents

Table of Contents

CHAPTER 01: STAT OF THE ART

CHAPTER 02 : MODELING OF THE PHOTOVOLTAIC DESALINATION SYSTEM COMPENENTS

CHAPTER 03 : PARTIAL SHADING EFFECTS ON PV GENERATOR

CHAPTER 04 : CONTROLS THE APPROACH OF THE DESALINATION SYSTEM POWERED BY A PHOTOVOTAIC SOURCE

CHAPTER 05 : EXPIREMENTAL RESULTS

References

ANNEXE 01

ANNEXE 02

General Introduction

General Introduction

The demand for freshwater is increasing rapidly to meet the needs of growing populations, industries, households, and agriculture. Ensuring adequate supplies of fresh water is critical for human health and economic development, and addressing freshwater demand is an urgent priority for communities and governments around the world. However, in many areas, there is limited access to freshwater sources. Desalination, the process of removing salt and other minerals from seawater or brackish water, is one approach to addressing this challenge.

Desalination technology has been used for decades in arid regions with limited access to freshwater sources, such as the Middle East and North Africa. There are several types of desalination processes used to produce fresh water from seawater or brackish water, including thermal distillation and membrane processes.

Thermal distillation uses heat to evaporate the water, leaving behind the salt and other impurities, while membrane processes use a semi-permeable membrane to filter out the salts and other contaminants. One advantage of thermal distillation is that it can be used to treat water with high salt concentrations, making it useful for treating seawater. However, it requires a lot of energy to heat the water, making it expensive and environmentally unsustainable. Additionally, thermal distillation can produce a large amount of brine waste, which can harm the environment if not disposed of properly. Membrane processes, on the other hand, are generally more energy-efficient and produce less waste than thermal distillation. They can also be used to treat a wider range of water sources, including brackish water. However, they are less effective at treating water with high salt concentrations, and the membranes can become fouled or damaged over time, requiring regular maintenance and replacement.

Each type of desalination process has its own advantages and disadvantages, and the choice of the process depends on several factors, such as the quality of the water source and level of salinity, energy availability, and cost considerations.

Renewable energy sources are sources of energy that are replenished naturally and are therefore considered sustainable and environmentally friendly. These sources of energy include solar, wind, hydro, geothermal, and biomass. Each renewable energy source has its unique advantages and disadvantages, and the choice of which technology to use depends on several factors, including the availability of resources, environmental impact, and cost considerations.

A Reverse Osmosis (RO) desalination system powered by renewable energy is a technology that combines two sustainable solutions to address the global water scarcity problem in remote areas. By combining these two technologies, a RO desalination system powered by renewable energy can provide a reliable and sustainable source of fresh water in areas with limited access to clean water and electricity. This technology has several benefits over traditional desalination systems that rely on fossil fuels. It is a clean and renewable source of energy, which reduces greenhouse gas emissions and environmental impact. It also provides a reliable source of fresh water in remote areas where access to electricity and clean water is limited. Additionally, the system can be easily scaled up or down depending on the demand for water.

To address this challenge, researchers and engineers have developed desalination systems that are powered by renewable energy sources, such as solar power. These systems use photovoltaic (PV) cells to convert sunlight into electricity, which can then be used to power the desalination process. However, the efficiency of a PV system depends heavily on the efficiency of its maximum power point tracker (MPPT), which is a device that optimizes the power output of the system by adjusting the voltage and current levels to match the maximum power point of solar panels. There are different types of MPPTs described in the literature, and the choice of MPPT will depend on the specific requirements of the PV system.

This research study addresses the region of Biskra, located in the southeast of Algeria, which is considered one of the best places for experimental projects related to solar desalination plants. Biskra is situated in the vast Algerian desert, characterized by a hot and dry climate throughout the long summer months, which becomes even hotter and drier as you move south. The clear sky in the desert results in a wide temperature range between night and day. These geographical and climatic conditions make Biskra an ideal location for the use of renewable energies, particularly photovoltaic solar energy.

Problematic

Improving the performance of a photovoltaic-powered water desalination system requires optimizing its design and operation to enhance its efficiency and reduce its cost. This can be achieved through various means, such as improving the efficiency of solar panels, designing more efficient desalination processes, and optimizing the integration of the solar power system with the desalination plant. In this context, the present study aimed to analyze the performance of a photovoltaic-reverse osmosis (PV-RO) desalination system under both uniform and non-uniform irradiation conditions. This manuscript is organized around five chapters that are arranged as follows:

- **Chapter One** provides an overview of the various technologies used for the desalination of water and the potential for integrating renewable energy sources into these processes. The chapter begins by discussing the growing demand for water in the world, specifically in Algeria. It then presents different types of desalination technologies, including thermal and membrane-based methods, and their respective advantages and disadvantages. The chapter also highlights the integration of renewable energies in desalination systems, such as solar, wind, and geothermal energy. The benefits and challenges associated with their use in desalination are discussed. The chapter concludes with solar energy being chosen as the feed source for an RO desalination system, which will be the subject of our study in this thesis.
- **Chapter Two** provides a comprehensive understanding of the modeling of PV desalination system components, which is crucial to this study. It also discusses the mathematical models used to describe the behavior of each component, such as the current-voltage characteristic of PV panels, the head/flow characteristic of the pump, and the performance of various water quality parameters.
- **Chapter Three** provides an in-depth analysis of the impact of partial shading on the performance of a photovoltaic (PV) generator and the effectiveness of different maximum power point tracking (MPPT) techniques in mitigating this effect. The chapter begins with a background on MPPT and an analysis of different global MPPT techniques for shading conditions. The chapter then presents various MPPT techniques and their working principles, including Perturb and Observe (P&O), classical Extremum Seeking Control (ESC) based on sinusoidal perturbation, Sliding mode control (SMC), and combination and hybrid methods. It analyzes the performance of each method under partial shading conditions and provides an experimental comparative study of their effectiveness.
- **Chapter Four** focuses on the control methods used to optimize the performance of a desalination system powered by photovoltaic energy. The chapter begins with an overview of TIADS (Technical Institute for Agricultural Development in the South) and the use of photovoltaic systems to replace electrical networks for powering them. It then discusses the different types of control methods used to regulate the operation of the system, including ESC applied to the PV generator, DTC (12 vectors) applied to the induction machine, and Lyapunov to maintain a constant DC bus. The chapter analyzes the characteristics of the RO (Reverse Osmosis) desalination system under uniform conditions (sudden irradiance change) and non-

uniform conditions (shading conditions with two scenarios). The chapter concludes by using real data from TIADS with three scenarios for the entire desalination system.

- **Chapter Five** validates the proposed control strategies used to optimize the performance of a desalination system powered by photovoltaic energy. The test bench was implemented in the Electrical Engineering Laboratory of Biskra (LGEB), associating a photovoltaic generator with a maximum power of 700 W peak, a boost chopper, a three-phase inverter, an induction machine of 270 W, a buck converter powered by a DC machine used as a pump emulator, and an RO membrane model. A dSPACE board (DS1104) controls the complete chain.

The manuscript ends with a general conclusion that summarizes and highlights the main results of this work and the perspectives envisaged for our future work.

Chapitre 01

STAT OF THE ART

Chapter 01: **STATE OF THE ART**

1.1. Introduction

Water is the backbone of our economy. Safe and adequate supplies of water are vital for agriculture, industry, recreation, and human consumption. While our water supply is largely safe and adequate today, we as a nation face increasing challenges related to water supply. These challenges include extended droughts, growing water demand due to population increases, more stringent health-based regulations, and competing demands from various users [1].

Water is one of the most abundant resources on the planet. However, the vast majority of it (about 97%) is salt water found in the oceans, and the remaining 3% is freshwater [2]. The freshwater shortage is becoming an increasingly significant problem in many parts of the world. Desalination has been shown to be a promising and viable technology for providing safe drinking water [3]. However, the main obstacle hindering the wider use of desalination technologies is the high cost, especially due to intensive energy consumption [4].

The use of renewable energies for controlling small-scale seawater and brackish water desalination plants has become possible, especially in isolated areas where conventional power generation is expensive. These areas are often characterized by a significant potential for renewable energy sources, coupled with a lack of drinking water resources.

In this chapter, we will present the search for new solutions to address the problems of freshwater scarcity, the availability of electrical energy, and the desire to limit environmental pollution, which contribute to combat global warming.

This chapter is arranged as follows: starting with the presentation of the current world situation of desalination and water, and after that, the Algerian situation of Water-Energy and Desalination. Then, the different desalination processes currently used for the production of fresh water from salt water will be presented, and we will specify their different characteristics. Special attention is given to the reverse osmosis process. At the end of the chapter, the coupling of desalination systems to renewable energies will be discussed, with an analysis of the different possible configurations with or without storage batteries.

1.2. Desalination and water in the world

In several regions across the world with local water basin depletions, communities have turned to alternative water sources, water recycling, water imports, and desalination [5]. Desalination is the process of removing excess salts and other dissolved chemicals from seawater [6], which has been around for centuries but has gained prominence in the last few decades. In 1565, French explorer Jean de Leary succeeded in desalinating water during a trip to Brazil, and in 1627, Sir Francis Bacon proposed the use of sand filters to desalinate water [7]. During the mid-1700s, advances in steam processes allowed for the wide use of evaporation and condensation methods for desalination, which continued to be the most common methods throughout the early 1900s [7]. In the mid-1900s, the development of membrane technology to aid in desalination began; however, it was not until 1960s when inventors in Canada patented an asymmetrical membrane that allowed for more cost-effective desalination, resulting in rapid expansion of the industry [8].

Desalination of brackish water and seawater has since grown rapidly around the globe. In 2013, there were over 17,000 active desalination plants, providing about 80 × 106 m3 /day water to 300 million people in 150 countries [9]. By 2015, the production capacity increased to nearly 97.5 × 106 m3 /day [10]. The supply of desalinated water is expected to increase to 192 × 106 m3 /day by 2050 [11]. Saudi Arabia is currently the largest producer of desalinated water worldwide and meets 60% of total water demand through desalination [12, 13]. In some countries like Kuwait and Qatar, 100% of the water used is obtained via desalination [14]. Despite the widespread use, desalination is still controversial as it is an expensive way to produce water [5]. Further, desalination has several environmental effects, including high greenhouse gas emissions and waste products that can affect the marine habitats [5, 6]. The world's population is increasing while resources remain consistent, even in some cases; these resources are diminishing because of pollution problems. Water assets and necessities differ from region to region.

1.3. Desalination, water, and energy in Algeria

It is important to take into account the great diversity of the climate and its irregularity in space and time. Because of its particular geographical situation (arid and semi-arid region), Algeria is subject to unfavorable physical and hydro-climatic conditions, accentuated by periods of chronic drought. Observed climate changes and the drought that has prevailed for several decades in North Africa, particularly in Algeria, have had a negative impact on the country's water resources.

Socio-economic development, the limited range of dams and groundwater, and the concentration of the population in the north of the country (about 80%) are the main causes of water scarcity in Algeria.

Algeria currently ranks 14th in the world among countries suffering from water scarcity, and if there are no effective measures, it will jump to 6th place by the year 2025 [15].

Algeria receives 65 billion cubic meters of rain per year of which:

- 15 billion of which goes into the rivers.
- 3 billion of which feed the groundwater.
- 47 billion evaporate into the atmosphere [15, 16].

In 2005, Algeria began producing freshwater through desalination or demineralization processes. The overall production capacity has already reached around 2.31 million cubic meters (m^3) per day. Seawater desalination may be the most appropriate solution to the situation faced by many regions in Algeria in order to bridge the gap between water demand and supply. The national agency estimates that the seawater desalination will contribute approximately 1.000 million cubic meters by 2030 [17].

In Algeria, around a quarter of groundwater is either completely or partially brackish. This water is mainly found in the country's desert and semi-desert regions. The exploitation of brackish water resources began in 2000, and the volume of brackish water mobilized is estimated to be 510 160 hm3/year with 160 hm3/year used to satisfy the drinking water supply. Twelve (12) stations are operating in the provinces of Tlemcen, Oran, Tizi-Ouzou, Bejaia, Illizi, Biskra, Ouargla, Medea and Ain Defla, with a total production of drinking water of 24.2 hm3/ year. Additionally, 241 hm3/year of brackish water will be demineralized from a mobilized volume of 464 hm3 through 35 stations, which are currently under study and work (included in different programs). The overall capacity of these stations is 91.5 hm3/year, and the overall throughput mobilized in the upstream exceeds 428.9 hm^3/year [18].

The current situation is as follows: six stations (Tamanrasset 4, El Oued 2) are still under study, while studies for four stations (Tamanrasset 2 and El Oued 2) have been completed. One station (Bechar) is currently under study and realization, while twelve stations (10 Ouargla, El Oued and Tamanrasset (ADE)) are in progress. Two stations of ADE (Tindouf and Illizi) are in the process of launching work. In addition, 15 stations (El Oued) are installing mono-blocks, with one station (Réguiba C.) completed and commissioned. Overall, water demand for all use sectors is expected to be approximately 20 billion m3 in 2030.

1.4. Desalination technologies

The main desalination processes can be classified into two categories based on the principle used: membrane processes and thermal processes, as shown in Figure (1.1) [19]. The first one operates on the basis of a phase change (liquid-vapor), while the second process essentially relies on filtration membranes. Thermal-based technologies work by supplying thermal energy to seawater to evaporate water, and then condensing this vapor to obtain potable water [20]. These technologies tend to be used in regions where water salinity levels are high and energy costs are low, such as in the Caribbean and the Middle East. Their main advantage is the absence of fouling problems occurring in membrane technology. Some examples of the most common thermal-based processes are multi-stage flash (MSF), multi-effect distillation (MED), and vapor compression distillation [19].

Although thermal technology has been widely used. Membrane-based technology has become more and more popular, especially in the Middle East due to its lower specific energy consumption, lower environmental footprint, and more flexible production capacity [21]. Some membrane technologies include ultrafiltration, electro-dialysis, and reverse osmosis [19, 22]. Reverse osmosis (RO) is now the most commonly used desalination process worldwide, comprising 61% of the global share, followed by MSF at 26% and MED at 8% [7]. RO is capable of treating a vast range of solute concentrations in water at a reasonable cost compared to other techniques. It can also provide higher water recovery rates than multi-effect and multi-stage flash distillation. In addition, RO has lower emissions than thermal-based desalination methods.

Reverse osmosis is based on the application of excessive pressure to reverse the spontaneous osmosis process, where water in solution moves across a semi-permeable membrane from lower to higher solute concentration. In reverse osmosis plants, this overpressure is applied by high-pressure pumps to push seawater and brackish water through semi-permeable membranes to obtain desalinated water [23].

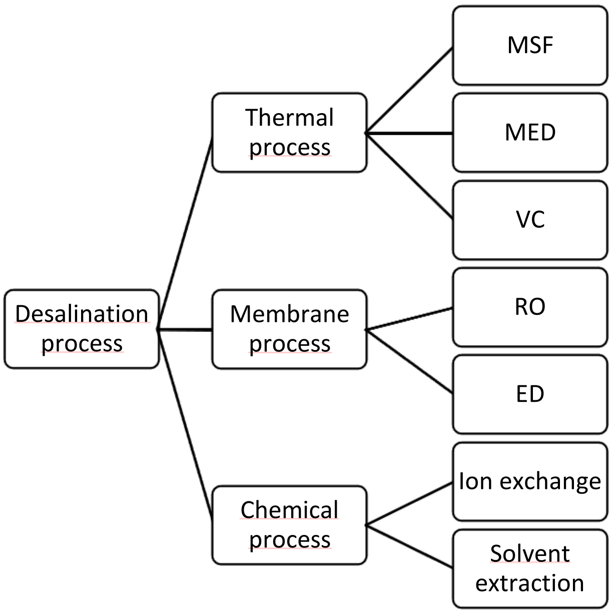

Figure 1.1 Different water desalination processes.

1.4.1. Thermal distillation technologies

The thermal desalination process involves boiling, evaporating, and condensing. It was the earliest method used to desalinate saline water on a commercial basis. The basic principle is to apply heat to create water vapor, which then condenses into pure water, separated from most salts and impurities. The commonly used thermal processes are MSF (Multi Stage Flash distillation), MED (Multi Effects distillation), and vapor compression (VC).

- **Multi Stage Flash distillation (MSF)**

This process shown in figure (1.2) is based on the principle of flash evaporation, where seawater is evaporated by reducing the pressure in successive process effects. The energy economy is achieved through successive regenerative heating, where seawater flashing in each flash chamber (effect or stage) rejects heat to the feed water, thereby heating incoming seawater [24]. Before entering the first stage, seawater is heated by external heat sources such as low-pressure steam from power plants or extraction steam from a steam turbine plant.

This heated seawater then enters the flash evaporation chambers with decreasing operating pressures in successive cycles. The typical number of stages for flashing and energy recovery varies between 15 and 30 in modern large-scale MSF plants [25]. The operating temperatures also vary between 90 and 120 C (known as top brine temperatures, TBT), depending on the quality of heat source available in the first stage [26]. Operating the plant at higher temperatures typically allows for higher efficiencies due to a higher number of stages.

The product water contains about 2–10 ppm and requires post-treatment (known as re-mineralization) before being supplied through pipelines for human consumption [24].

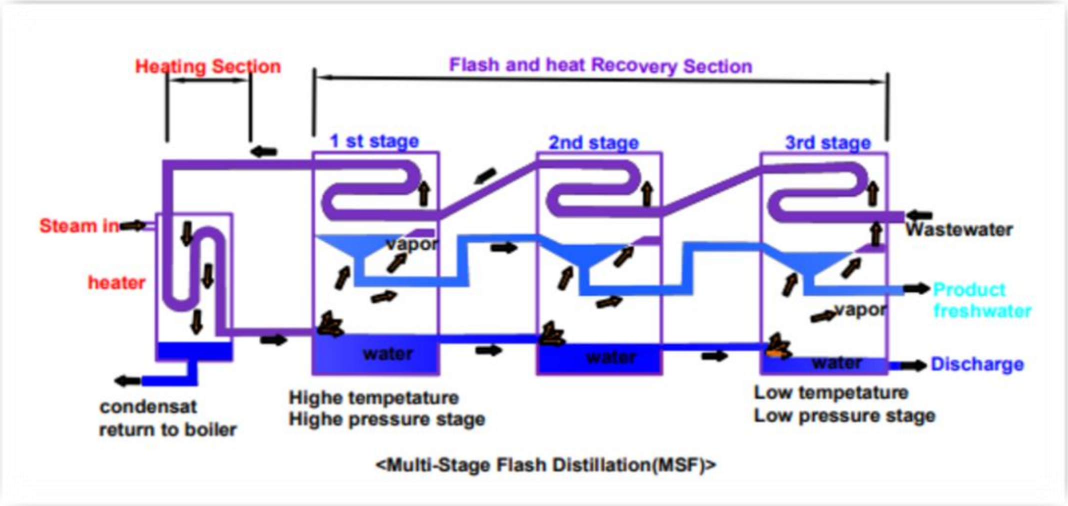

Figure 1.2 Multi-Stage Flash distillation.

➢ Multi Effects distillation (MED)

The MED process shown in figure (1.3) is the most thermodynamically efficient thermal desalination technology available today [27]. Similar to the MSF process, the MED process operates in a number of effects to increase energy efficiency. However, unlike the MSF process, the pre-heated seawater is sprayed onto the tubes in the first evaporation chamber, which are heated by an external heat source derived from a power plant steam [28]. This process is operated in a dual-purpose power plant scheme. The freshwater vapor evaporated in the first evaporation chamber passes through a condenser that serves as evaporating surface in the next effect. The remaining brine from the first evaporation chamber is passed through the next effect, where it is sprayed on the evaporating tubes at lower temperatures and pressures. This process continues in successive effects until a suitable temperature gradient is available for freshwater evaporation. The energy or steam economy is proportional to the number of effects. The total number of effects is limited by the total temperature range available and the minimum allowable temperature difference between successive effects [29]. The typical number of effects in the MED process varies between 4 and 21, depending on the heat source temperature and the top brine temperature in the first effect. The top brine temperatures are usually around 90 C for MED processes, but a lower top brine temperature of 70 C is also possible, which are called low temperature MED (LTMED) [30]. Although this process is considered thermodynamically efficient, a drawback is the requirement for large heat transfer areas. The heat transfer areas for LTMED are considerably higher than MED process, often varying between 25% and 40%.

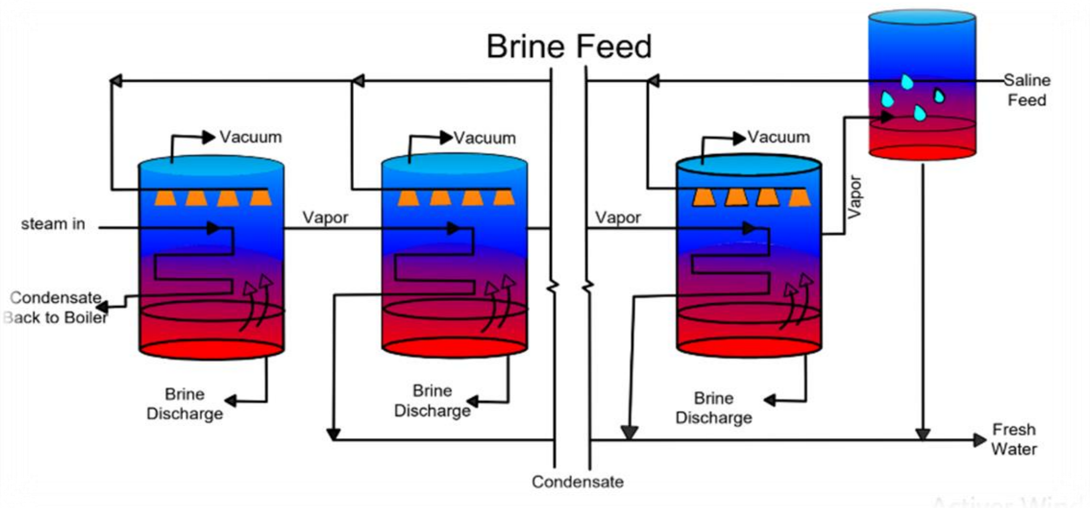

Figure 1.3 Multi Effect Distillation.

➢ Vapor Compression (VC)

Distillation plants that use vapor compression rely on the heat generated by the compression of water vapor to evaporate salt water. There are two methods of vapor compression: mechanical vapor compression (MVC) and thermo vapor compression (TVC).

The MVC system consists of five major elements: a mechanical vapor compressor, an evaporator/ condenser heat exchanger, pre-heaters for the intake seawater, brine and product pumps, and a venting system [31]. In the MVC process, mechanical energy is used to compress the water vapor, raising its temperature and pressure. The high-pressure vapor is then condensed, releasing heat that is used to evaporate salt water. The condensed water is collected as fresh water, while the salt is left behind in the brine. Pre-heaters for the intake seawater help to reduce the energy required for the distillation process.

In the TVC process, thermal energy is used to compress the water vapor. The compressed vapor is then used to evaporate salt water, and the condensed vapor releases heat that is used to preheat the seawater. This process reduces the energy required for the distillation process. The TVC system also includes pre-heaters for the intake seawater, brine and product pumps, and a venting system.

Overall, both the MVC and TVC processes are effective in producing fresh water from salt water, with each method having its own unique advantages and disadvantages.

Vapor compression shown in figure (1.4) is suitable for small to medium scale desalination plants. The principle behind this technology is that energy recovery from the vapor generated in the last effect by compressing it either thermally in a steam ejector or mechanically in a compressor to act as a heat source for the first effect. The compression of the vapor raises the steam pressure and temperature to a level higher than the vapor generated in the first effect [32]. The compressor creates a vacuum in the evaporator and then compresses the vapor taken from the evaporator, which is then condensed inside a tube bundle. Seawater is sprayed on the outside of the heated tube bundle where it boils and partially evaporates, producing more vapor. With the steam-jet type of VCD unit, called a thermo-compressor, the steam jet creates and extracts water vapor from the evaporator, creating a lower ambient pressure. The steam jet compresses the extracted water vapor. This mixture is condensed on the tube walls to provide the thermal energy, the heat of condensation, to evaporate the seawater being applied on the other side of the tube walls in the evaporator. The difference between the two vapor compression techniques is that mechanical vapor compression requires the installation of an expensive compressor, whereas thermal vapor compression requires a simple ejector [33]. MVC compressor is known to have lower efficiency and higher maintenance disadvantages, which are not the case with the TVC method [33, 34].

Figure 1.4 Vapor Compression.

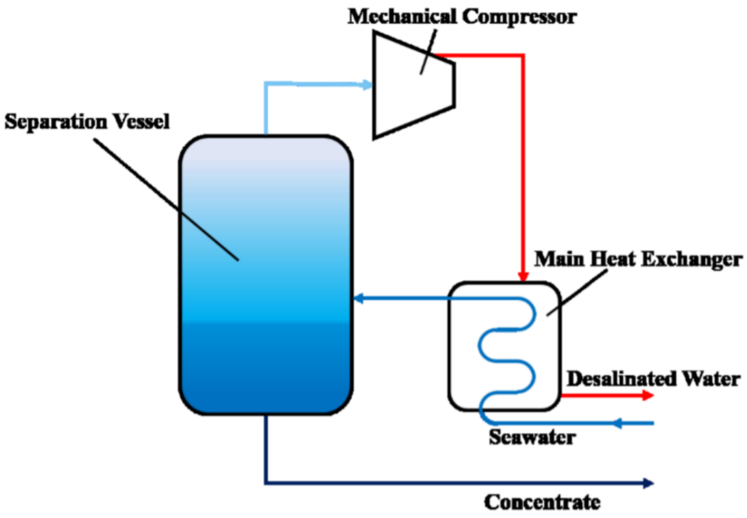

1.4.2. Membrane desalination technologies

In membrane processes, a membrane that separates two phases allows for the easier transportation of one or more components compared to other components. The driving force of the transport can be a pressure or temperature gradient, a concentration gradient, or an electrical potential gradient. There are two mainly types of membrane processes commonly used for desalination: reverse osmosis (RO) and electro-dialysis (ED).

1.4.2.1. Reverse Osmosis (RO)

Reverse Osmosis (RO) is currently the most reliable state-of-the-art technique for seawater and brackish water desalination. It has been used as an alternative source for producing clean water to minimize desalination associated costs [35-37]. The utilization of RO for desalination has significantly increased since the 1950s [38]. RO processes can be grouped into brackish water RO plants (BWRO) and seawater RO plants (SWRO), based on the quality of the processed input. BWRO plants process feed water with salinity in the range of 500 mg/L to 10,000 mg/L and can be further sub-grouped into low salinity BRWO plants, which process feed water with salinity between 500 and 2500 mg/L and high salinity BRWO plants that process water with salinity between 2500 and 10,000 mg/L. Currently, around 50% of the desalinated water available globally is produced by using RO [36]. The efficiency of RO depends on several factors, including the operational parameters, the employed membrane, and the feed water characteristics.

➢ Principle of reverse osmosis

The physical phenomenon of osmosis has been known to mankind since many years [39]. Osmosis, in simplest terms, can be defined as a natural process in which water molecules spontaneously move from a solution of low solute concentration (low osmotic pressure) to a solution of high solute concentration (high osmotic pressure) across a semi permeable membrane (Figure 1.5.a). The membrane, being semi permeable, rejects the solutes and only allows water molecules to pass through. The process of osmosis continues until a state of osmotic equilibrium is reached where the chemical potentials across the membrane become equal (Figure 1.5.b). The flow of water molecules can be stopped or reversed by application of an external pressure on the solution of higher concentration (feed solution) [40]. In case the applied pressure difference is greater in magnitude than the osmotic pressure difference across the membrane, water molecules are forced to flow in a direction opposite to that of the natural osmosis phenomenon. In such a case, the process occurring is known as RO and is depicted in Figure (1.5.c).

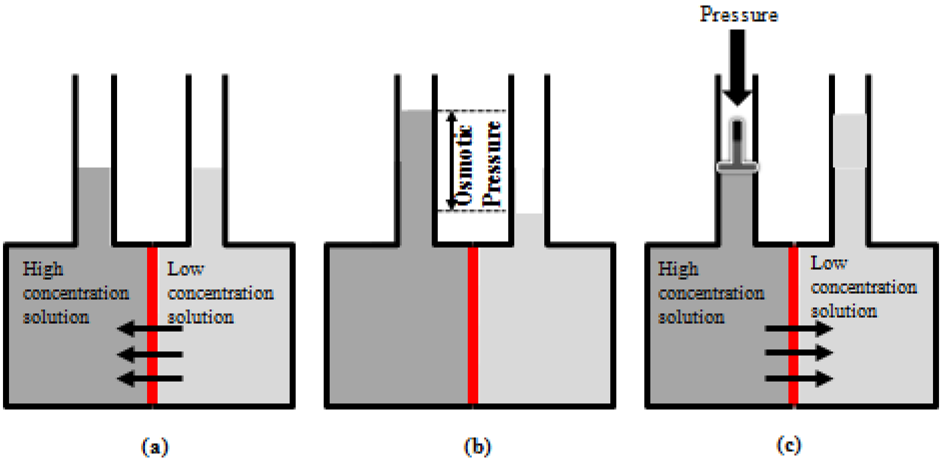

Figure 1.5. Schematic of (a) osmosis (b) osmotic equilibrium (c) RO.

➢ Type of reverse osmosis modules

Reverse osmosis (RO) modules are classified into different types based on their configuration and design. Here are some of the common types of reverse osmosis modules:

1. The **Plate and Frame** design, illustrated in Figure (1.6), is the simplest RO module design. It comprises a frame with a flat plate on each side of the RO membrane. The module operates in a cross-flow configuration, where the feed water flows through the module.

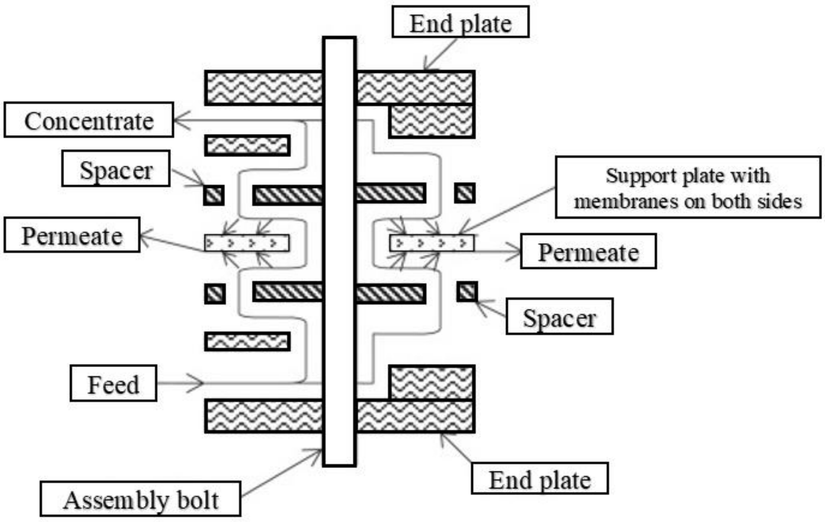

Figure 1.6. Schematic of a plate-and-frame module [41].

2. Figure (1.7) shows the **Spiral Wound** design, which is the most widely used RO module design. This design includes a permeate carrier and feed spacer that are wound around a central permeate tube. The feed water flows in a spiral pattern between the membrane and the permeate tube, while the permeate flows through the membrane to the central tube.

The primary suppliers of spiral membrane modules are FILMTEC, TORAY, HYDRANAUTICS and KOCH.

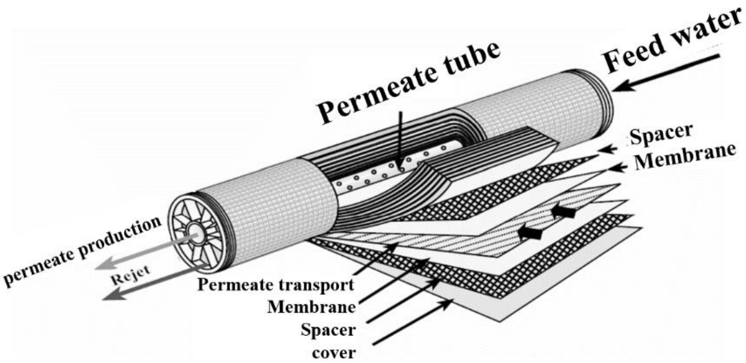

Figure 1.7. RO spiral module.

3. Figure (1.8) depicts the **Hollow Fiber** design, in which the RO membrane consists of hollow fibers, bundled together. The feed water flows through the center of the fibers, and the permeate passes through the fiber walls.

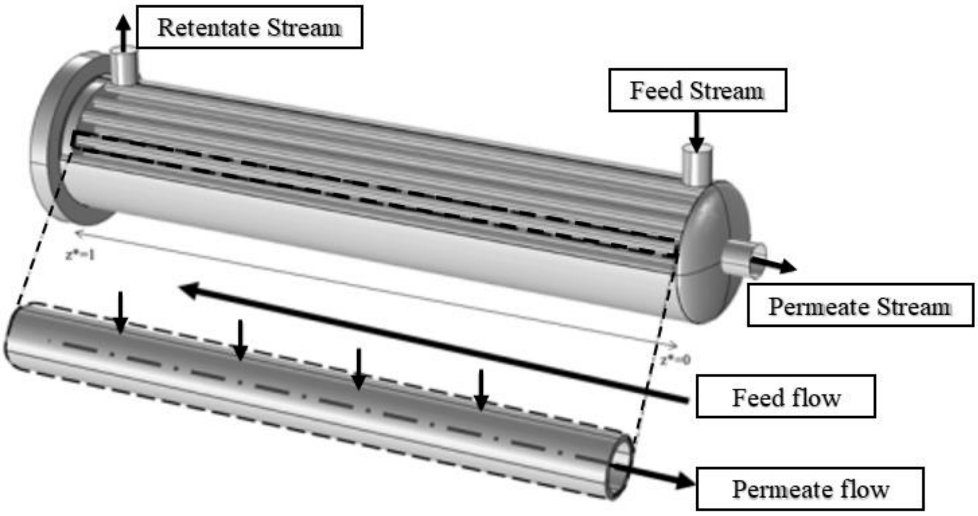

Figure 1.8. Schematic of hollow fiber RO membrane [42].

4. **Tubular**: This design consists of a bundle of RO membrane tubes mounted inside a pressure vessel. The feed water flows inside the tubes, and the permeate passes through the membrane walls.

5. **Capillary**: This is a relatively new RO module design consisting of very small-diameter hollow fibers bundled together. The feed water flows through the center of the fibers, and the permeate flows through the fiber walls.

Each of these reverse osmosis module designs has its own advantages and disadvantages, and the selection of the appropriate module for a particular application depends on the specific requirements and characteristics of the feed water and the desired permeate quality.

1.4.2.2.Electro-dialysis

The operating principle of this method is based on the migration of ionic salts toward their respective counter-charge electrodes. Selective membranes that allow passage of either anions or cations in an alternating fashion result in concentrate and product streams. The anions can pass through the anion-selective membrane but are not able to pass by the cation-selective membrane, which blocks their path and traps the anions in the brine stream [43]. Similarly, cations move in the opposite direction through the cation-selective membrane under a negative charge and are trapped by the anion-selective membrane. A typical ED system includes a membrane stack with a number of cell pairs, each consisting of a cation transfer membrane, a demineralized flow spacer, an anion transfer membrane, and a concentrate flow spacer. Compartments for the electrodes are at opposite ends of the stack. The electrodes need regular flushing to reduce fouling or scaling [44]. Figure (1.9) represents the schematic of the electrodialysis process, which summarizes its working principle.

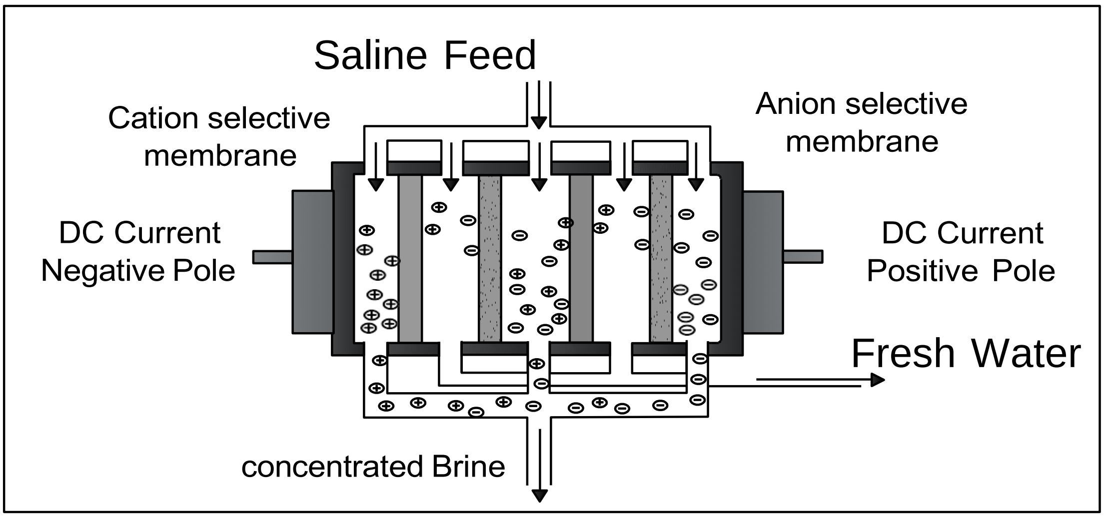

Figure 1.9. Schematic of the electro-dialysis process.

1.4.3. Chemical process

This process is carried out either by ion exchange or solvent extraction. Despite their advantages and disadvantages, each of these processes also has varying energy consumption per m^3 of drinking water. Table 1.1 presents a summary of the advantages and disadvantages of each desalination process [45].

Table 1.1. Advantages and disadvantages of the different processes

PROCÉSS	advantages	Disadvantages
REVERSE OSMOSIS	- Treatment of all types of water (brackish water, sea water, ...) - Removal of 98% to 99% of dissolved solid particles and 100% of microorganisms. - Low energy consumption especially for brackish water. - Adaptation to any size of installation and to any available energy source (conventional or not) - Wide range of available capacities - Flexibility of operation - High efficiency: can reach up to 80% of the production capacity	- Sensitivity of membranes to clogging - Mandatory and relatively complex pre-treatment - Sensitivity of production costs to water salinity - Limited life time of its membranes - Salinity of the water produced sometimes incompatible with certain industrial uses
DISTILLATION	+ Obtaining ultra-pure water (from 5 to 30 mg/l) suitable for industrial and pharmaceutical applications + Effective for very high salinity water (> 40g/l)	- High energy consumption (Electrical and thermal) - High cost of installation
ELECTRODIALYSIS	- Mainly used for domestic uses with low salinity water to be desalinated	- Effective only for desalination of water with a salinity not exceeding 2.5 g/l. - Major membrane scaling problems.
ION EXCHANGE	+ Efficient for the treatment of water whose salinity does not exceed 10 g/l.	- High risk of clogging - Mandatory pre-treatment to avoid bacterial development.

MSF and RO are the most widely used seawater desalination methods today. In [46], we note that the majority of the new units built use the RO desalination technique because of its advantages over other techniques. Figure (1.10) shows the desalination units installed worldwide according to the different techniques, in 2011 [46].

In areas where energy costs are lower, MSF desalination is suitable for large-scale units. On the other hand, RO desalination is suitable for medium and small-scale units, especially in regions where the energy cost is higher.

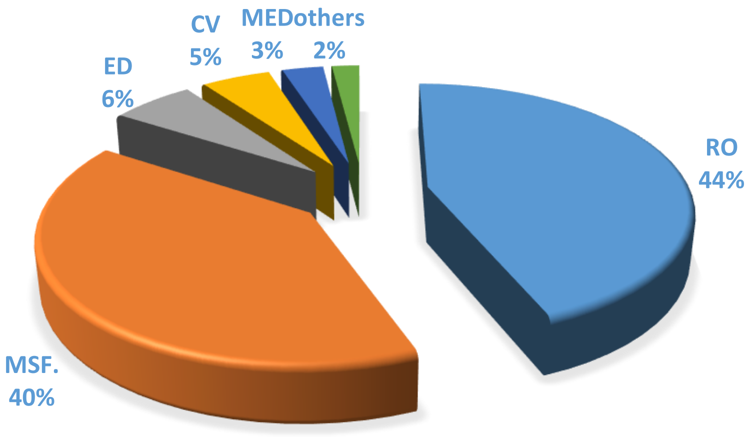

Figure 1.10. Desalination units installed worldwide according to the different techniques.

1.5. Desalination powered by renewable energy

Enormous research has been conducted on integrating renewable power sources with various desalination technologies [46, 47]. It is well established that solar energy is the most promising application with a significant contribution for sustainability [48]. Similarly, wind turbines are another sustainable approach to energy production. The transient nature of wind kinetics is different from that of solar energy. Wind turbines, if well designed, may provide adequate energy during night times and in winter when solar energy is insufficient. A good combination of these two energy sources may better match the dynamic energy demand of RO desalination plant, which is mainly governed by freshwater withdrawal and consumers' lifestyle. Freshwater demand not only fluctuates on an hourly basis but also responds to climate variation and seasonal deviation. Dry and wet seasons also impact the freshwater withdrawal rates [49].

In the vast Algerian desert, the climate is hot and dry during the long summer months, and it is becomes progressively hotter and drier as one proceeds towards the south. The sky in the desert is usually clear, favoring a wide temperature range between night and day.

In the northern part of the desert, the average maximum temperature in July and August is around 40 °C in Biskra, which is known as the "Gateway of the Sahara". These geographical and climatic criteria highlight the importance of using renewable energies, especially photovoltaic solar energy. Studies and researches are converging towards renewable energies sources to address the challenges of remote regions without access to the electricity grid. Today, several renewable energy sources are used, including geothermal, hydro, solar, wind, and biomass, as shown in Figure (1.11).

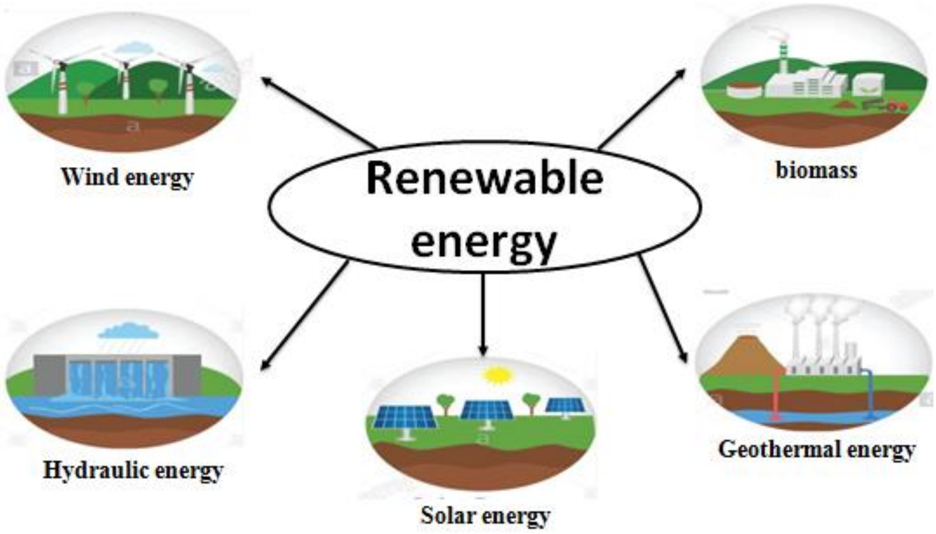

Figure 1.11. Different types of renewable energy.

The majority of desalination systems that use renewable energy sources are currently under research. The distribution of installed desalination capacity by the main renewable energy sources is shown in Figure (1.12). Solar energy is the most widely used renewable source for desalination, with a percentage of 42%. It can be used for the desalination of brackish or seawater by generating the thermal energy required to drive the phase change processes or by generating the electricity required to drive the membrane processes [50].

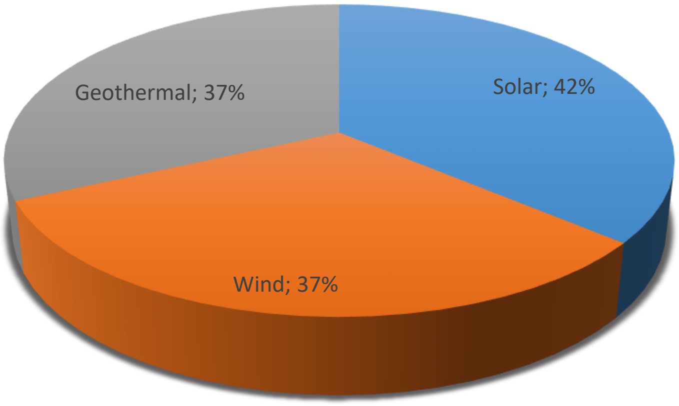

Figure 1.12. Global distribution of desalination by main renewable energy sources (2019).

1.5.1. Wind energy and RO

Wind power is mostly the use of wind turbines to generate electricity. At the beginning of wind energy development, the size of a wind power plant was small ranging from under 1 MW to 10 MW. In the past 40 years, its size has increased significantly [51]. A wind farm equipped with wind-driven pressurizing devices can be used for desalinating saltwater using reverse osmosis with constant pressure and variable flow [52].

1.5.2. Geothermal energy

Geothermal energy has been found to be an effective method for water desalination. Lakic [53] discovered a method of desalinating water from a large body of salty water by lowering a geothermal generator deep into a predrilled well bore below the Earth's surface. Marshall [53] revealed a system for producing thermal energy that can be used to generate electricity or desalinate water. Another technique for water desalination involves extracting fluids from near the sea surface through deep sea vents formed at the scattering ridge zones of the Earth's oceans due to the internal energy of surficial hot magma [54]. Al-Garni and Abdelrahman [55] examined a novel water desalination system that uses geothermal energy and includes a series of stepped evaporation trays.

1.5.3. Solar energy

Solar energy is the mother of all other renewable energies. It does not pollute, is freely, available everywhere, and several patents have been invented for systems and methods that collect and convert solar energy into electrical energy. This electrical energy can be used for water desalination [53]. However, the main disadvantages of solar energy is that it is a fluctuating source. On the other hand, water usage is continuous. Therefore, Mueller et al. [53] investigated the possibility of switching between day and night operations to maintain continuous operation mode. In order to achieve this, studies and research are converging towards either electrical storage using batteries or hydraulic storage.

1.6.Desalination system configurations

Many small-scale renewable energy-based desalination plants have been installed and successfully operated with minimal maintenance. However, their output is negligible when compared to the global capacities [56, 57] due to the plant size and salinity of the feed water. Figure (1.13) shows possible options for water desalination based on renewable energy sources.

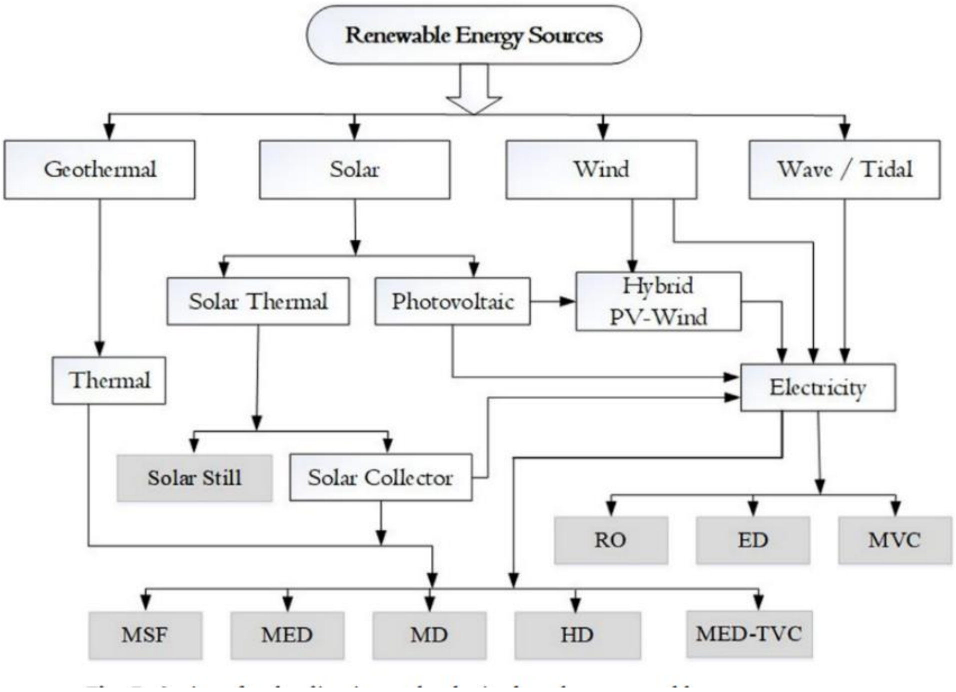

Figure 1.13. Options for desalination technologies based on renewable energy resources[58].

Renewable energy sources can provide two forms of energy: thermal and electrical. Thermal energy can power desalination processes such as those based on MSF, MED, MD, solar still, and humidification-dehumidification (HD) techniques, while electrical energy can power desalination processes such as those based on RO and ED techniques.

Standalone PV-powered desalination systems are commercially available [59]. Research and commercialization of PV-RO desalination technologies have been underway for more than three decades. The main difficulty for such systems is the high initial cost and the intermittent nature of solar energy. However, with significant advances in the field of photovoltaics, these systems are becoming preferred to conventional generators for several reasons. They are environment friendly, produce no sound or air pollution, require minimal maintenance, and can generate power throughout their lifespan [56].

PV-powered desalination systems include PV arrays, inverters, and sometimes battery banks, as well as thermal or membrane processes for desalination. In PV-RO desalination systems, direct current (DC) electricity generated by the PV arrays can run the high-pressure pumps to feed water to exude the permeate from the RO membranes [58]. Mahmoud and Ibrik [60] describe how either RO or ED water desalination technology can be connected to a PV generator, providing a feasible option for desalination in remote areas. Figure (1.14) shows a schematic representation of a PV-RO system with two scenarios, with or without batteries.

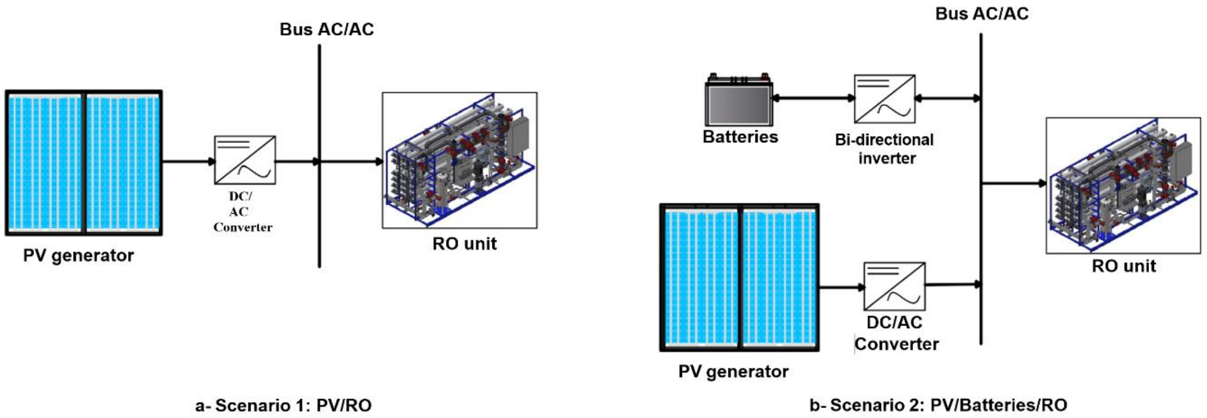

a- Scenario 1: PV/RO

b- Scenario 2: PV/Batteries/RO

Figure 1.14. Schematics representation of a PV-RO system.

The most widely used renewable energy source after solar energy is wind energy, which can power small-capacity desalination plants [61]. Electrical power generated by wind turbines is used for powering desalination plants. Wind turbine technology is commercially mature and emerging as a promising solution for seawater desalination, especially in coastal regions where higher wind resources are available [62].

Desalination processes using RO driven by wind energy can operate in both islanding and grid-connected modes. Although a wind energy system (WES) cannot guarantee the continuous operation of an RO plant, energy can be stored in the form of desalinated water to meet the demand when the plant is not operating [63]. Small desalination plants integrated with independent wind energy systems have enormous potential for transforming brackish water and seawater into potable water at a reduced cost [61]. However, a standalone wind-RO plant, without battery storage, may not be cost-effective due to the fluctuating nature of wind, which can decrease production and even halt the process in the absence of wind [62].

Using a battery and generator backup solves this problem, and a wind-diesel-RO plant can produce freshwater and electricity even in the absence of wind [64]. Figure (1.15) shows the basic configuration of a wind-RO desalination system.

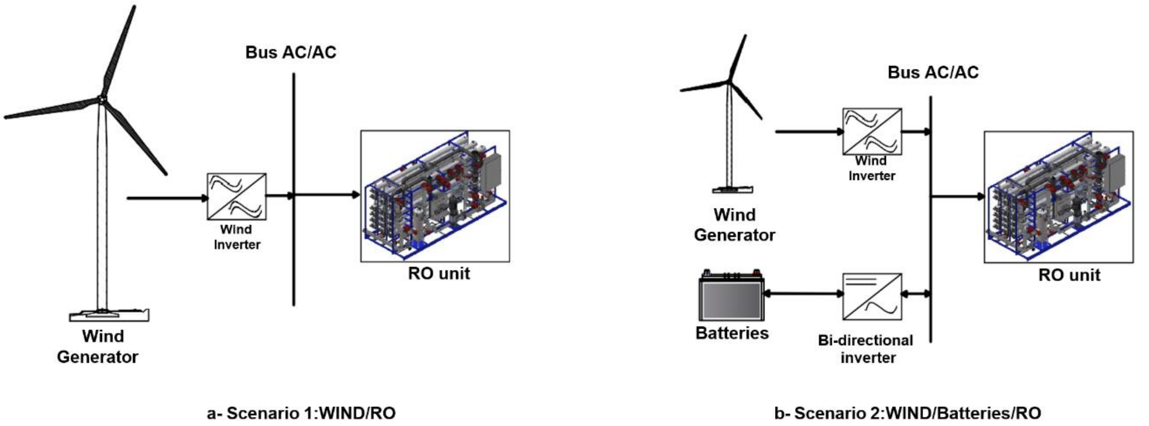

a- Scenario 1:WIND/RO

b- Scenario 2:WIND/Batteries/RO

Figure 1.15. Schematics representation of wind-RO system.

Several researchers have done the combination of the two sources (PV and wind) with RO systems. The key advantage of a hybrid PV-wind system is that the desalination unit can be operated in the absence of one of the energy sources. Manolakos et al. [65] have developed software to perform simulations of a hybrid PV-wind-RO system. They studied various combinations of renewable energy sources, such as solar and wind, with and without battery storage. Figure (1.16) shows the basic configuration of a PV-wind-RO desalination system.

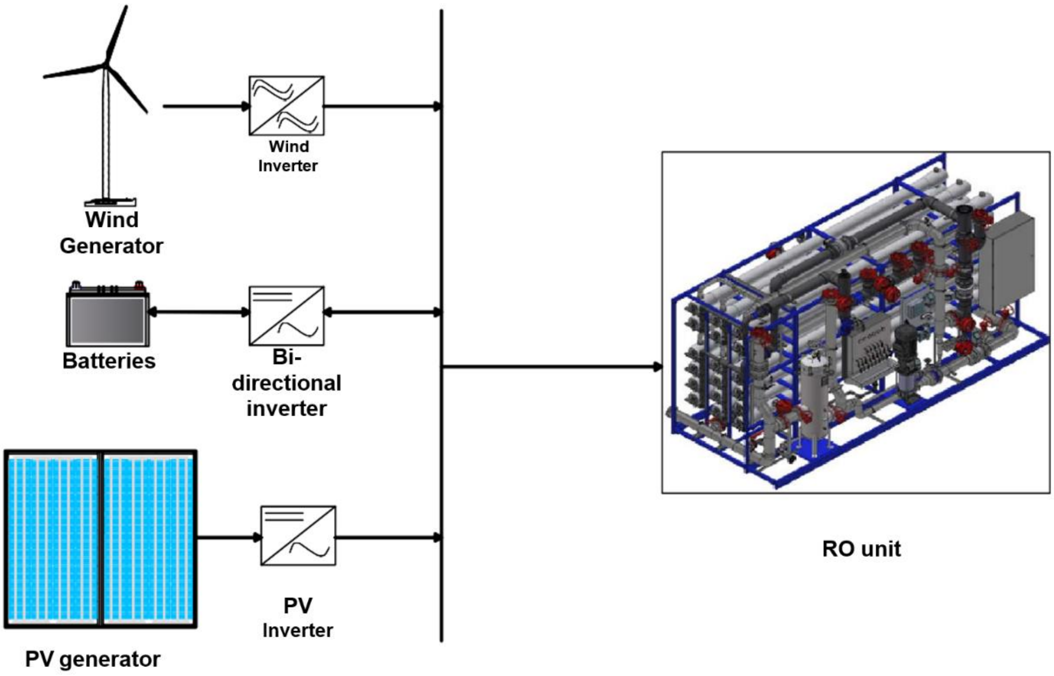

Figure 1.16. Schematics representation of PV-wind-RO system.

Many studies on both experimental and theoretical analysis of coupling the RO desalination technique with a renewable energy system have been conducted. Table (1.2) provides a summary of the theoretical studies and experimental units for renewable energy powered RO systems [66].

Table 1.2
Coupling *RE*/*RO* systems e State of the art.

	REFERENCE	STAND-ALONE SYSTEMS								NON STAND-ALONE SYSTEMS				
		Simple without Batteries			Simple with Batteries		Hybrid							
		COUPLING												
		PV/RO	*WIND /RO*	*Diesel /RO*	*PV /Batteries/RO*	*Wind/ Batteries/RO*	*PV /Diesel/RO*	*PV/WIND //Diesel/RO*	*PV/WIND /Batteries/RO*	*PV/Gird/RO*	*WIND /Gird/RO*	*PV/WIND //Gird IRO*	*PV/WIND //DieselIRO*	*PV/WIND //Diesel/Gird/RO*
EXPERIMENTAL	Joyce et al. [1]	■												
	Thomson [2]	■												
	Pestana et al. [3]		■											
	Carta et al. [4]		■											
	Kolkas and Papathanassiou [5]		■											
	Liu et al. [6]		■											
	Miranda [7]		■											
	Masson et al. [8]				■									
	Abdallah et al. [9]				■									
	Sardi and Beer [10]				■									
	Maurel [11]				■									
	Kehal [12]													
						■								
	Weiner et al. [6]							■						
	Kershman et al. [23]											■		
MODELING & DESIGN	Helal et al. [24]	■		■			■							
	Thomson [11]	■												
	Tzen et al. [25]				■									
	Voivontas et al. [4]				■	■		■	■	■				
	Setiawan et al. [3]							■	■					
	Tzen et al. [26]									■				
	Mohamed and Papadakis [27]									■				
	Hochnut [28]												■	
	Rheinlander et al. [29]													■

1.7. Conclusion

In this chapter, we have presented the current situation of water and energy in the world in general and in Algeria in particular. We have also presented a state of the art of desalination processes associated with renewable energies. In addition, a comparison between desalination processes was made, which will enable us to adopt a configuration of a renewable desalination system that will be presented in the next chapter.

Chapter 02

Modeling of the Photovoltaic desalination System Components

Chapter 2: Modeling of the Photovoltaic desalination System Components

2.1.Introduction

Following the discussion in the previous chapter, figure (2.1) illustrates a typical configuration of a battery-less photovoltaic (PV) water desalination system. The system comprises a PV generation system with a group of series-parallel connected modules (PV arrays); a passive input filter, and a capacitor used to reduce the current and voltage ripple (and hence power) at the PV side. The input filter is followed by two conversion stages in a cascade that allows for adequate transfer of the energy extracted from the PV generator to the load. The first stage, called the "DC-DC boost converter" performs maximum power point tracking (MPPT) of the PV array and elevates its voltage. The second stage, called the "DC-AC" converter", is connected through the DC-link (capacitor) to the three-phase two-level inverter. The inverter converts DC power to AC power and feeds the energy to the induction motor (IM) with high power quality. The IM is directly coupled with a high-pressure centrifugal pump to convert mechanical energy into hydraulic energy. This hydraulic energy is used to transport brackish water to the reverse osmosis (RO) unit by converting the kinetic energy to the hydrodynamic power of the water flow. The feed water passes through the RO membrane under high pressure to overcome the osmotic one. At the outlet of the RO membrane, two outputs are distinguished: brine with highly concentrated salt and fresh water.

To control the PV desalination system, an essential step is to model the installation components. Hence, this chapter presents the explicit mathematical models for the PV array, both the boost and invert power converters, IM, centrifugal pump, and RO membrane.

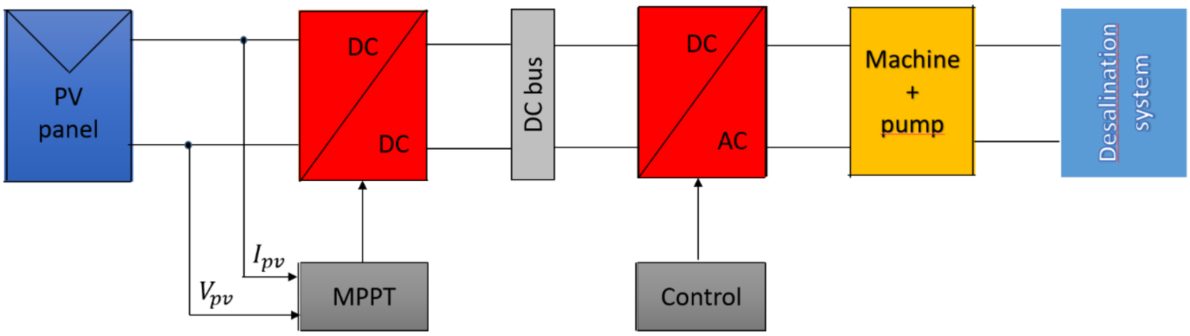

Figure 2.1. Schematic diagram of the proposed PV-RO desalination system.

2.2.PV array modeling

A photovoltaic generator consists of several photovoltaic panels connected together in series and/or in parallel to provide the necessary current and voltage. The generator's performance depends on the variability of the modules comprising the generator and the cells within those modules. The integrated set of photovoltaic panels and the supporting structure are defined as a photovoltaic array. The set of photovoltaic arrays forms a photovoltaic field. Figure (2.2) represents a PV field which is a large-scale installation consisting of multiple PV arrays.

Figure 2.2. Photovoltaic (PV) field

2.2.1. PV cell

Typically, solar cells are named after the semiconducting component that makes them up. These materials must have certain characteristics in order to absorb sunlight. Solar cells can be constructed using just one layer of light-absorbing material (single-junction) or using numerous physical configurations (multi-junctions) to take advantage of diverse absorption and charge separation techniques.

Three main types of photovoltaic cells can be distinguished [67]: mono-crystalline cells (also called first-generation cells), poly (or multi)crystalline cells, and amorphous cells. Table (2.1) provides a systematic summary of these PV cells.

Table 2.1: Features of PV cells types

Cell type	Photoelectric conversion efficiency	Advantages	Disadvantages
Mono-crystalline [68-70]	25.6%	- high conversion efficiency - Low maintenance cost. - Long life-span (25-year warranty) - Good performance under low irradiation conditions.	- High costs. - Circuit breakdown when the solar panel is covered with dirt, shade or snow. - Complicated manufacturing
Poly-crystalline [71-73]	22.3%	- Relatively high conversion efficiency - Low costs - The manufacturing process is simpler - Higher performance while increasing the operating temperature.	- Limited supply - Complicated manufacturing - Lower efficiency due to low silicon purity. - Require a higher installation area than a mono-crystalline solar panel.
Amorphous [74]	13.4%	- Higher efficiency than the other two. - can withstand higher temperatures without output being affected - Lower production cost - Flexible and lightweight.	- Not suitable for roof installations - Need nearly double the panel area for the same power output

Among the different modeling structures found in the literature [75], that explain photovoltaic conversion, the famous single diode model, with four parameters (I_{ph}, I_o, V_{th}, R_s), displayed in figure (2.3), reproduces the PV cell's equivalent circuit. It consists of a photovoltaic current source $\mathrm{I_{ph}}$ which represents the irradiance, a diode representing the diffusion effect, and a shunt resistor $\mathrm{R_p}$(which has been eliminated), emulating losses around the junction due to impurities. A second resistor $\mathrm{R}_s$connected in series, emulates the joules losses.

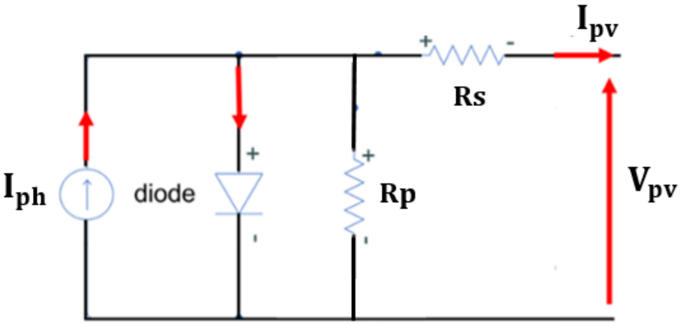

Figure 2.3. The PV cell equivalent circuit.

The relationship between the PV voltage and current of the module is obtained via the famous non-linear implicit equation [76]:

$$\mathbf{I_{pv} = I_{ph} - I_0 \left[\exp\left(\frac{V_{pv}+I_{pv}R_s}{V_{th}}\right) - 1\right]} \qquad (2\text{-}1)$$

Where the saturation current of the diode $\mathrm{I_0}$ is given by equation (2-2), which depends on temperature T (in Kelvin).

$$\mathrm{I_0 = I_{0r}\left(\frac{T}{T_r}\right)^3 \exp\left(\left[\frac{qE_g}{K_bA}\right] \times \left[\left(\frac{1}{T_r}\right) - \left(\frac{1}{T}\right)\right]\right)} \qquad (2\text{-}2)$$

The photo-generated current I_{ph} depends on solar irradiance E $(\mathrm{W/m^2})$ and the short-circuit current of the PV cell under standard conditions $\mathrm{I_{sc}}$, often given by:

$$\mathrm{I_{ph} = \frac{E}{E_r}[I_{sc} + K_i(T - T_r)]} \qquad (2\text{-}3)$$

2.2.2. PV module

When several PV cells are combined in series or parallel, they form a PV module. If the cells are connected in series, their voltages add up, increasing the total voltage of the module. Conversely, if the cells are connected in parallel, the current increases. The PV module is generally rated by its DC output power under standard test conditions (STC), which are specified at an irradiance of 1000 W/m^2 and a temperature of 25^0C for the PV cell. The nonlinear current-voltage characteristic of the PV module is modeled by the following equation, assuming that all cells are identical:

$$\mathbf{I_{pv} = N_pI_{ph} - N_pI_0\left[\exp\left(\frac{N_sV_{pv}+(N_s/N_p)I_{pv}R_s}{N_sV_{th}}\right) - 1\right]} \qquad (2\text{-}4)$$

The PV module type considered in this thesis is Monocristallin (Sharp) NTR5E3E/ NT175E1, with a power output of 175 Wp. Table (2.2) lists the electrical rated characteristics of this module under STC. Figure 2.4 shows the power versus voltage (P-V) and current versus voltage (I-V) characteristics of the module under STC conditions. A PV module can produce power at any point on the I-V curve, known as the operating point. There are three important operating points on the I-V curve that define the performance of a PV module: the maximum power point (V_{MPP}, I_{MPP}), the short-circuit current point (I_{sc}, 0), and the open-circuit voltage point (0, V_{oc}).

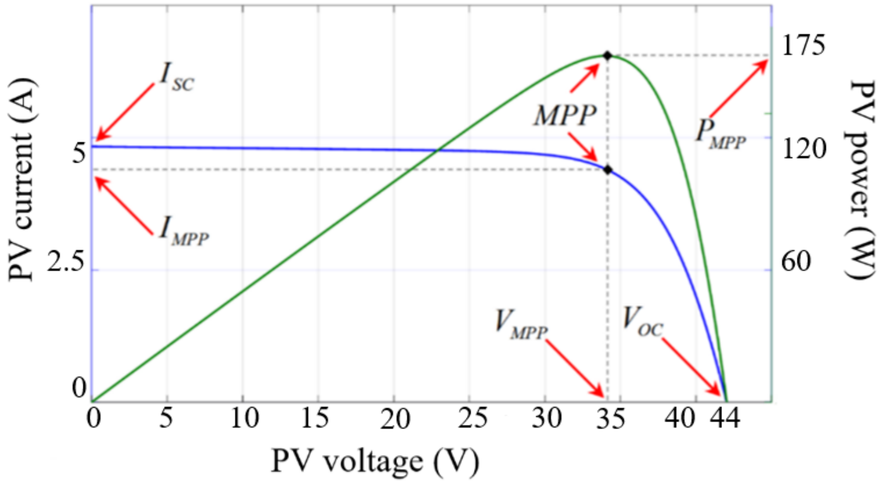

Figure 2.4. I-V and P-V characteristics of NTR5E3E/ NT175E1 under STC.

Table 2.2: PV module parameter

Type	Monocristallin (Sharp) NTR5E3E/ NT175E1
Maximum power	$P_{max} = 175{,}0\ W$
Optimum current	$I_{op} = 4{,}95\ A$
Optimum voltage	$V_{op} = 35{,}4\ V$
Open circuit voltage	$V_{oc} = 44\ V$
Open circuit current	$I_{cc} = 5\ A$
Number of cells per module	$N_s = 72$

2.2.3. PV array

A PV array, also known as a PV generator (PVG), consists of a series-parallel arrangement of PV modules to obtain the desired voltage, current, and power. The size of the PV array can range from a single module to any number of modules. The PV array output current and voltage can be computed using equations (2-5) and (2-6) respectively:

$$I_{pvG} = n_p I_{pv} \tag{2-5}$$

$$V_{pvG} = n_s V_{pv} \tag{2-6}$$

Figure 2.5 and Figure 2.6 show respectively P-V and I-V characteristics under different irradiation levels between 700 and 1000 W/m^2, while the temperature is kept constant ($T_c =$ 25°C).

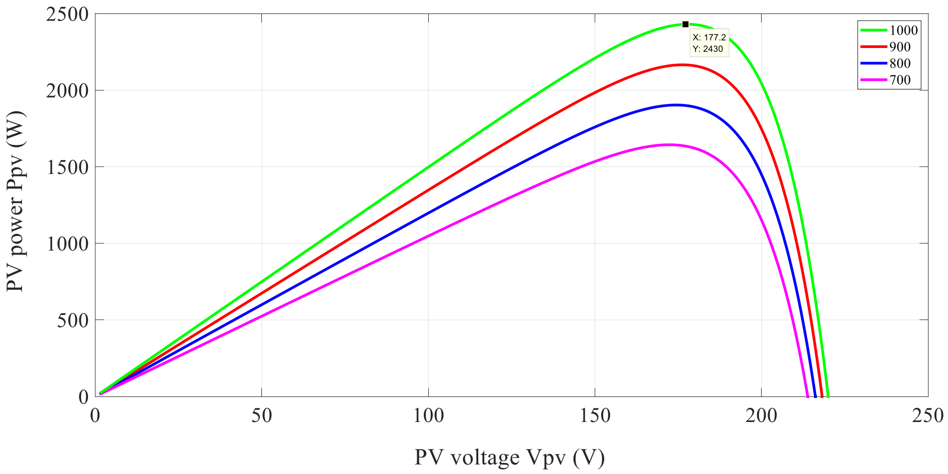

Figure 2.5. P-V characteristics of PV array under different levels of solar irradiation at 25°C

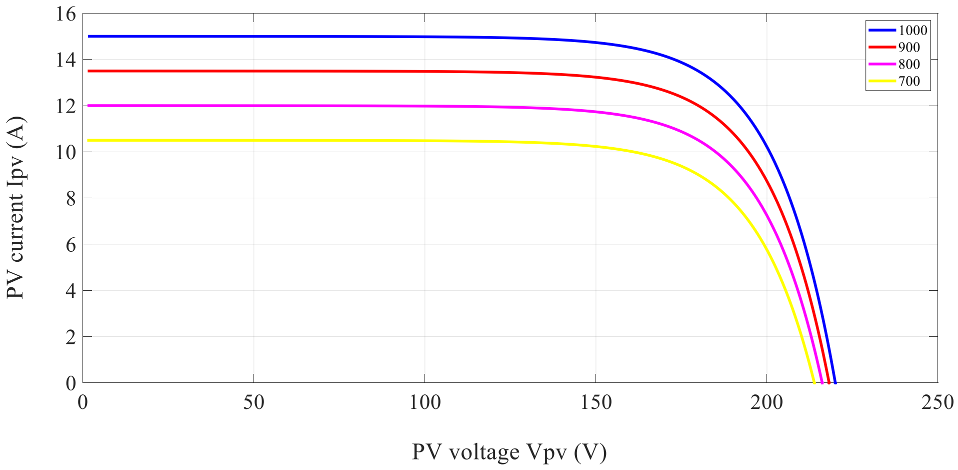

Figure 2.6. I-V characteristics of PV array under different levels of solar irradiation at 25°C.

2.3.Power converters modeling

Power electronic converters play a crucial role in optimizing the energy output of photovoltaic (PV) systems. In a PV-RO desalination system, power converters are critical for efficient and effective operation. The adaptation stage usually involves a DC-DC power converter that boosts the low DC voltage output of the PV panels to a higher DC voltage level required by the DC/AC three-phase inverter. The inverter then converts this DC voltage into three-phase AC power, which is required by the RO desalination system. Additionally, the inverter regulates the output voltage and frequency to ensure that it is stable and matches the requirements of the RO system. This helps to ensure that the RO system operates at optimal power and efficiency levels, thereby maximizing the energy output of the PV system.

Overall, the role of power converters in a PV-RO desalination system is essential in providing a reliable source of fresh water using renewable energy sources. The two converters used in our system are chopper boost and voltage inverter types, as shown Figure (2.7).

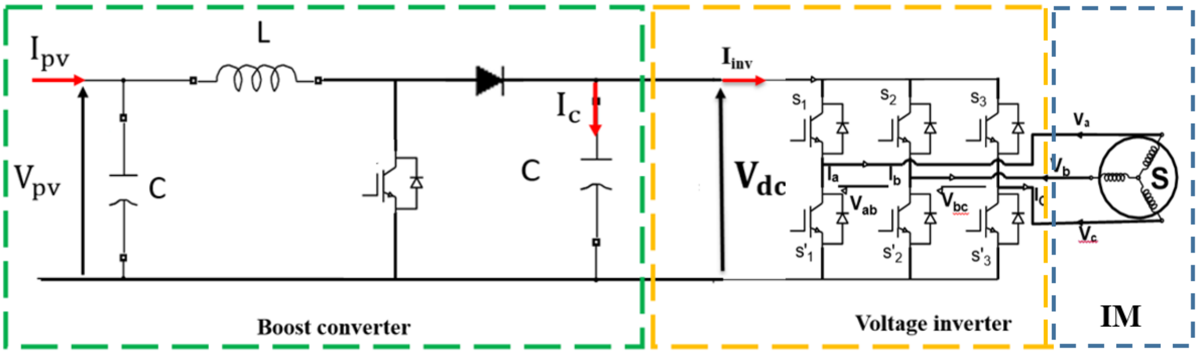

Figure 2.7. Power converters in the PV-RO desalination system.

2.3.1. Boost converter

The boost converter plays the role of an impedance adapter for maintaining the PV generator at the maximum power point. It is more suitable for loads located to the right of the optimum PV point, where adjusting the duty ratio allows the input impedance to match the optimum value. A boost converter typically consists of an inductor, a power electronic switch (IGBT), a diode, and a capacitor [77].

➢ **Operating sequences and state equations :**

❖ First conduction sequence:

In this sequence, the switch S is closed, while the diode D is blocked alternately. This causes the current in the inductor to increase and a quantity of energy to be stored in magnetic form, while the load is disconnected (figure 2.8).

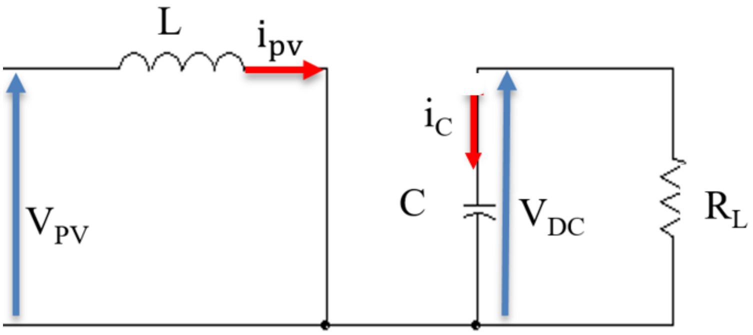

Figure 2.8. The equivalent electrical circuit of the first conduction sequence.

The dynamic behavior of the circuit is given by:

$$\frac{di_{pv}}{dt} = \frac{1}{L} V_{pv} \qquad (2\text{-}7)$$

$$\frac{dV_{dc}}{dt} = -\frac{1}{CR_L} V_{dc} \qquad (2\text{-}8)$$

Considering the current i_{pv} and the output voltage V_{dc} as state variables, equation (2-9) models the first sequence.

$$\begin{bmatrix} \dot{x}_1 \\ \dot{x}_2 \end{bmatrix} = \begin{bmatrix} 0 & 0 \\ 0 & -\frac{1}{CR_L} \end{bmatrix} \begin{bmatrix} x_1 \\ x_2 \end{bmatrix} + \begin{bmatrix} \frac{1}{L} \\ 0 \end{bmatrix} V_{pv} \qquad (2\text{-}9)$$

Where: $x_1 = i_{pv}$ and $x_2 = V_{dc}$

- Second conduction sequence:

In this phase, the switch S is opened, which results in a transfer of the energy accumulated in the coil to the capacitor C (figure 2.9). Equations (2-10), (2-11) and (2-12) similarly define the dynamic behavior of the converter for this sequence:

$$\frac{di_{pv}}{dt} = \frac{1}{L} V_{pv} - \frac{1}{L} V_{dc} \qquad (2\text{-}10)$$

$$\frac{dV_{dc}}{dt} = \frac{1}{C} i_{pv} - \frac{1}{R_L C} V_{dc} \qquad (2\text{-}11)$$

The state representation of this sequence is:

$$\begin{bmatrix} \dot{x}_1 \\ \dot{x}_2 \end{bmatrix} = \begin{bmatrix} 0 & -\frac{1}{L} \\ \frac{1}{C} & -\frac{1}{CR_L} \end{bmatrix} \begin{bmatrix} x_1 \\ x_2 \end{bmatrix} + \begin{bmatrix} \frac{1}{L} \\ 0 \end{bmatrix} V_{pv} \qquad (2\text{-}12)$$

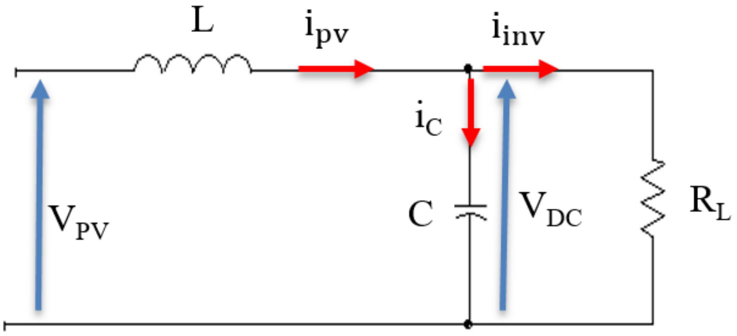

Figure 2.9. Equivalent electrical circuit of the second conduction sequence.

- **Average model :**

The continuous-time expressions of the boost converter can be found as follows [78]:

$$\begin{cases} \frac{di_{pv}}{dt} = -\frac{(1-\alpha)}{L} V_{dc} + \frac{1}{L} V_{pv} \\ \frac{dV_{dc}}{dt} = \frac{1-\alpha}{C} i_{pv} - \frac{1}{CR_L} V_{dc} \end{cases} \quad (2\text{-}13)$$

Which is put into final form, under:

$$\begin{bmatrix} \dot{x}_1 \\ \dot{x}_2 \end{bmatrix} = \begin{bmatrix} 0 & -\frac{(1-\alpha)}{L} \\ \frac{1-\alpha}{C} & -\frac{1}{CR_L} \end{bmatrix} \begin{bmatrix} x_1 \\ x_2 \end{bmatrix} + \begin{bmatrix} \frac{1}{L} \\ 0 \end{bmatrix} V_{pv} \quad (2\text{-}14)$$

The relationship between the mean values PV and load voltage is presented in the following equation:

$$\frac{V_{dc}}{V_{pv}} = \frac{1}{1-\alpha} \quad (2\text{-}15)$$

2.3.2. Voltage inverter

The power circuit of the voltage source inverter is shown in Figure (2.7). The three-phase inverter consists of three switching arms, each one is composed of two cells with a diode and a IGBT transistor in antiparallel with the DC-link voltage and three AC voltage as output [79].The inverter is modeled by associating a logic function F with each arm, which determines its conduction states:

$$F_1 = \begin{cases} 1 & \text{if } S_1 \text{ passing and } S'_1 \text{ open.} \\ 0 & \text{if } S'_1 \text{ passing and } S_1 \text{ open.} \end{cases}$$

$$F_2 = \begin{cases} 1 & \text{if } S_2 \text{ passing and } S'_2 \text{ open.} \\ 0 & \text{if } S'_2 \text{ passing and } S_2 \text{ open.} \end{cases}$$

$$F_3 = \begin{cases} 1 & \text{if } S_3 \text{ passing and } S'_3 \text{ open.} \\ 0 & \text{if } S'_3 \text{ passing and } S_3 \text{ open.} \end{cases}$$

The compound voltages at the output of the inverter are related to the connection functions F via the following equations:

$$V_{ab} = V_{dc}(F_1 - F_2) \quad (2\text{-}16)$$

$$V_{bc} = V_{dc}(F_2 - F_3) \quad (2\text{-}17)$$

$$V_{ca} = V_{dc}(F_3 - F_1) \quad (2\text{-}18)$$

Consequently, the simple voltages V_a, V_b, V_c are then synthesized as follows [80]:

$$V_a = \frac{V_{dc}}{3}(2F_1 - F_2 - F_3) \quad (2\text{-}19)$$

$$V_b = \frac{V_{dc}}{3}(2F_2 - F_1 - F_3) \quad (2\text{-}20)$$

$$V_c = \frac{V_{dc}}{3}(2F_3 - F_1 - F_2) \quad (2\text{-}21)$$

The following matrix equation is used to model the two-level voltage inverter[45]:

$$\begin{bmatrix} V_a \\ V_b \\ V_c \end{bmatrix} = \frac{V_{dc}}{3} \begin{bmatrix} 2 & -1 & -1 \\ -1 & 2 & -1 \\ -1 & -1 & 2 \end{bmatrix} \begin{bmatrix} F_1 \\ F_2 \\ F_3 \end{bmatrix} \tag{2-22}$$

Equation (2-23) represents the relationship between the inverter input current and the three-phase output currents:

$$I_{inv} = F_1 I_a + F_2 I_b + F_3 I_c \tag{2-23}$$

Table (2.3) indicates that the switches can be in either ON or OFF position, represented by 1 or 0. Switches 1, 3, and 5 are the upper switch configuration.

Table 2.3 Switching state for each leg

V_i	state	Leg a	Leg b	Leg c
		S_1	S_3	S_5
V_1	active	1	0	0
V_2	active	1	1	0
V_3	active	0	1	0
V_4	active	0	1	1
V_5	active	0	0	1
V_6	active	1	0	1
V_0	zero	0	0	0
V_7	zero	1	1	1

2.4.DC bus model

The time evolution of the DC bus voltage is obtained from the integration of the capacitive current:

$$\frac{dV_{dc}}{dt} = \frac{1}{C} i_c \tag{2-24}$$

The capacitor current comes from a node where the PVG current at the chopper output (Idc) and the current is modulated by the voltage inverter flow (figure 2.10). The capacitor current is determined by (2-25):

$$I_c = I_{dc} - I_{inv} \tag{2-25}$$

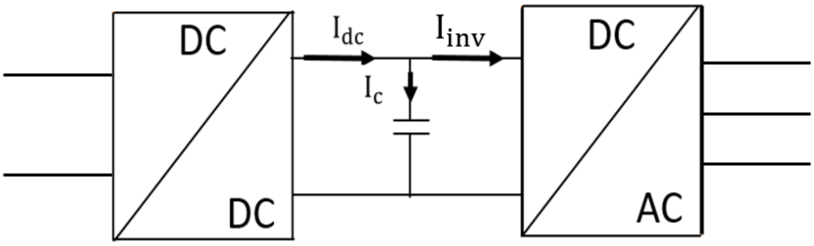

Figure 2.10. Representation of the DC bus.

2.5.Induction motor modeling

Among all types of AC machines, the induction machine, especially the squirrel cage type, is the most widely used in the industry. These machines are economical, robust, and reliable, and are available in a range of low power to high power.

The three-phase asynchronous machine has a fixed stator and a rotor that is movable about the axis of symmetry of the machine. Figure 2.11 shows the six windings of the three-phase asynchronous machine in electrical space. Three identical windings with p pairs of poles are housed in regularly distributed slots inside the stator; their axes are separated from each other by an electrical angle equal to $\frac{2\pi}{3}$ [81]. The voltage inverter supplies the phases of the stator with an adjustable frequency and amplitude.

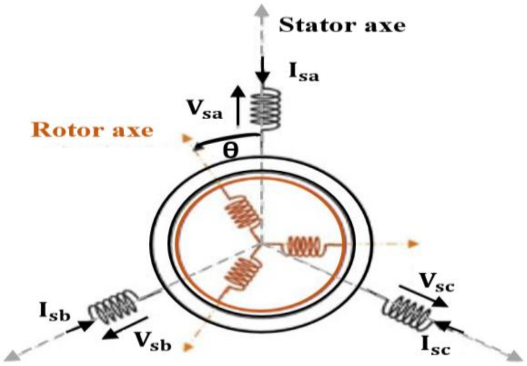

Figure 2.11. Representation of the three-phase asynchronous machine in the electrical space.

Before setting up the equations of the asynchronous machine in the (α-β) axis, let us consider the following assumptions:

2.5.1. Hypothesis

Before modelling the asynchronous machine, it is necessary to make several assumptions [82]:

- Saturation is neglected, so the self and mutual inductances are independent of the currents flowing in the windings.
- The magneto motrice force (m.m.f) is distributed sinusoidally in the machine's air gap, and there is symmetry with regard to the magnetic axis of the windings.
- Notches are assumed to be non-existent.
- Hysteresis and eddy currents in the magnetic parts are not taken into account.

The machine considered in this work is a three-phase induction motor. In an induction motor, alternating currents feed three-phase terminals and flow in the stator windings, producing a rotating stator flux in the machine. The rotational speed of this magnetic field is defined as the synchronous speed, which is related to the number of poles of the machine and the power source [83].

2.5.2. Setting in equations of the Induction Motor

The dynamic behavior of the asynchronous machine is characterized by three types of quantities: electrical, magnetic and mechanical [84].

- **Electrical equations**

In figure (2.11), the electrical equations of the model of the three-phase asynchronous machine are respectively written for the stator with the index “s” and the rotor with the index “r” as follows:

$$\begin{bmatrix} V_{sa} \\ V_{sb} \\ V_{sc} \end{bmatrix} = \frac{d}{dt}\begin{bmatrix} \varphi_{sa} \\ \varphi_{sb} \\ \varphi_{sc} \end{bmatrix} + \begin{bmatrix} R_s & 0 & 0 \\ 0 & R_s & 0 \\ 0 & 0 & R_s \end{bmatrix}\begin{bmatrix} I_{sa} \\ I_{sb} \\ I_{sc} \end{bmatrix} \tag{2-26}$$

$$\begin{bmatrix} V_{ra} \\ V_{rb} \\ V_{rc} \end{bmatrix} = \frac{d}{dt}\begin{bmatrix} \varphi_{ra} \\ \varphi_{rb} \\ \varphi_{rc} \end{bmatrix} + \begin{bmatrix} R_r & 0 & 0 \\ 0 & R_r & 0 \\ 0 & 0 & R_r \end{bmatrix}\begin{bmatrix} I_{ra} \\ I_{rb} \\ I_{rc} \end{bmatrix} \tag{2-27}$$

- **Magnetic equations**

The stator and rotor flux equations can be expressed as follows:

$$\begin{bmatrix} \varphi_{sa} \\ \varphi_{sb} \\ \varphi_{sc} \end{bmatrix} = \begin{bmatrix} L_s & M & M \\ M & L_s & M \\ M & M & L_s \end{bmatrix}\begin{bmatrix} I_{sa} \\ I_{sb} \\ I_{sc} \end{bmatrix} + [M_{sr}]\begin{bmatrix} I_{ra} \\ I_{rb} \\ I_{rc} \end{bmatrix} \tag{2-28}$$

$$\begin{bmatrix} \varphi_{ra} \\ \varphi_{rb} \\ \varphi_{rc} \end{bmatrix} = \begin{bmatrix} L_r & M & M \\ M & L_r & M \\ M & M & L_r \end{bmatrix}\begin{bmatrix} I_{ra} \\ I_{rb} \\ I_{rc} \end{bmatrix} + [M_{rs}]\begin{bmatrix} I_{sa} \\ I_{sb} \\ I_{sc} \end{bmatrix} \tag{2-29}$$

Where $$[M_{sr}] = [M_{rs}]^t = M_{max}\begin{bmatrix} \cos\theta & \cos(\theta - \frac{4\pi}{3}) & \cos(\theta - \frac{2\pi}{3}) \\ \cos(\theta - \frac{2\pi}{3}) & \cos\theta & \cos(\theta - \frac{4\pi}{3}) \\ \cos(\theta - \frac{4\pi}{3}) & \cos(\theta - \frac{2\pi}{3}) & \cos\theta \end{bmatrix} \quad (2\text{-}30)$$

- **Mechanical equations**

The mechanical equation can be expressed by the following expression:

$$T_e - T_r = J\frac{d\Omega}{dt} + f\Omega \quad (2\text{-}31)$$

2.5.3. Transformation of the machine model from three-phase to two-phase

The equation of the induction machine leads to a system of six differential equations with variable coefficients. The resolution of this system is very difficult; hence, there is a need to transform the three-phase system into an equivalent two-phase system. This transformation must preserve the instantaneous power and the reciprocity of mutual inductances. Preserving the mutual inductances allows us to establish an expression for the electromagnetic torque that is valid for the real machine [85]. With the development of digital tools, this transformation can now be easily performed.

There are mainly two transformations:

- Three-phase-Diphase transformation "in a fixed benchmark" **Concordia**.
- Transformation fixed reference frame - rotating reference frame "**Park**".

2.5.3.1. Transformation of Concordia

The Concordia transformation simplifies the equations of an AC machine by converting the three-phase representation (x_a , x_b, x_c) to a two-phase representation (x_α, x_β), and vice versa using the Concordia matrix T_{32} and its inverse matrix T_{32}^{-1}, respectively.

The Concordia transformation is given by:

$$\begin{bmatrix} x_\alpha \\ x_\beta \\ x_0 \end{bmatrix} = T_{32} \begin{bmatrix} x_a \\ x_b \\ x_c \end{bmatrix} \quad (2\text{-}32)$$

The inverse transformation is given by:

$$\begin{bmatrix} x_a \\ x_b \\ x_c \end{bmatrix} = T_{32}^{-1} \begin{bmatrix} x_\alpha \\ x_\beta \\ x_0 \end{bmatrix} \quad (2\text{-}33)$$

Where $T_{32} = \begin{bmatrix} 1 & -\frac{1}{2} & -\frac{1}{2} \\ 0 & \frac{\sqrt{2}}{3} & -\frac{\sqrt{2}}{3} \\ \frac{1}{\sqrt{2}} & \frac{1}{\sqrt{2}} & \frac{1}{\sqrt{2}} \end{bmatrix}$ and $T_{32}^{-1} = \begin{bmatrix} 1 & 0 & \frac{1}{\sqrt{2}} \\ -\frac{1}{2} & \frac{\sqrt{2}}{3} & \frac{1}{\sqrt{2}} \\ -\frac{1}{2} & -\frac{\sqrt{2}}{3} & \frac{1}{\sqrt{2}} \end{bmatrix}$

2.5.3.2.Transformation of Park

The Park transformation, also known as the dq0 transformation, is a mathematical technique used to transform the three-phase quantities of an AC electrical system into a two-coordinate rotating frame of reference. The transformation is named after its inventor, John Park.

The Park transformation is given by the following equations:

$$\begin{bmatrix} x_d \\ x_q \\ x_0 \end{bmatrix} = [P(\theta)] \begin{bmatrix} x_a \\ x_b \\ x_c \end{bmatrix} \tag{2-34}$$

The inverse Park transformation is given by the following equations:

$$\begin{bmatrix} x_a \\ x_b \\ x_c \end{bmatrix} = [P(\theta)]^{T} \begin{bmatrix} x_d \\ x_q \\ x_0 \end{bmatrix} \tag{2-35}$$

In the case of an equilibrated system, the Park transformation is obtained from a unique matrix (2x3) given by:

$$P(\theta) = k \begin{bmatrix} \cos\theta & \cos(\theta - \frac{2\pi}{3}) & \cos(\theta - \frac{4\pi}{3}) \\ -\sin\theta & -\sin(\theta - \frac{2\pi}{3}) & -\sin(\theta - \frac{4\pi}{3}) \end{bmatrix} \tag{2-36}$$

Where k is a constant that can take the value $\frac{2}{3}$ for the transformation with no power conservation or the value $\sqrt{\frac{2}{3}}$ for the transformation with power conservation.

2.5.3.3.Induction motor on (α,β) frame

In the alpha-beta frame, the three-phase currents and voltages can be represented as two components in each frame, one component on the alpha-axis and one on the beta-axis. This transformation simplifies the analysis of the machine behavior and allows for the development of control algorithms.

$$\begin{cases} V_{s\alpha} = R_s I_{s\alpha} + \frac{d\varphi_{s\alpha}}{dt} \\ V_{s\beta} = R_s I_{s\beta} + \frac{d\varphi_{s\beta}}{dt} \\ V_{r\alpha} = 0 = R_r I_{r\alpha} + \frac{d\varphi_{r\alpha}}{dt} + \varphi_{r\beta}\omega_r \\ V_{r\beta} = 0 = R_r I_{r\beta} + \frac{d\varphi_{r\beta}}{dt} - \varphi_{r\alpha}\omega_r \end{cases} \quad (2\text{-}37)$$

Where

$$\begin{cases} \varphi_{s\alpha} = L_s I_{s\alpha} + M\, I_{r\alpha} \\ \varphi_{s\beta} = L_s I_{s\beta} + M\, I_{r\beta} \\ \varphi_{r\alpha} = L_r I_{r\alpha} + M\, I_{s\alpha} \\ \varphi_{r\beta} = L_r I_{r\beta} + M\, I_{s\beta} \end{cases} \quad (2\text{-}38)$$

By replacing (2-38) in (2-37), the system becomes:

$$\begin{cases} V_{s\alpha} = R_s I_{s\alpha} + L_s \frac{dI_{s\alpha}}{dt} + M\, \frac{dI_{r\alpha}}{dt} \\ V_{s\beta} = R_s I_{s\beta} + L_s \frac{dI_{s\beta}}{dt} + M\, \frac{dI_{r\beta}}{dt} \\ 0 = R_r I_{r\alpha} + L_r \frac{dI_{r\alpha}}{dt} + M \frac{dI_{s\alpha}}{dt} + \omega_r\left(L_r I_{r\beta} + M\, I_{s\beta}\right) \\ 0 = R_r I_{r\beta} + L_r \frac{dI_{r\beta}}{dt} + M \frac{dI_{s\beta}}{dt} - \omega_r\left(L_r I_{r\alpha} + M\, I_{s\alpha}\right) \end{cases} \quad (2\text{-}39)$$

The electromagnetic torque is defined by:

$$T_e = \frac{3}{2} p\left(\varphi_{s\alpha} I_{s\beta} - \varphi_{s\beta}\, I_{s\alpha}\right) \quad (2\text{-}40)$$

2.6.Centrifugal pump modeling

RO desalination typically utilizes a pressure system provided by a pump. The most common types of pumps used in RO units are centrifugal pumps, dedicated to high pressure, and positive displacement pumps, which are suitable for low flow rates. Choosing the right pump requires a thorough understanding of existing market equipment, operating characteristics, design, efficiency, as well as dimensional and pressure-flow ranges. Centrifugal pumps are most commonly used in RO desalination plants due to their numerous advantages, including reduced volume, relatively silent operation, and ease of implementation. These pumps convert the energy of a kinetic source (motor: torque-speed) into hydraulic energy (pressure-flow). Figure (2.12) illustrates a centrifugal pump.

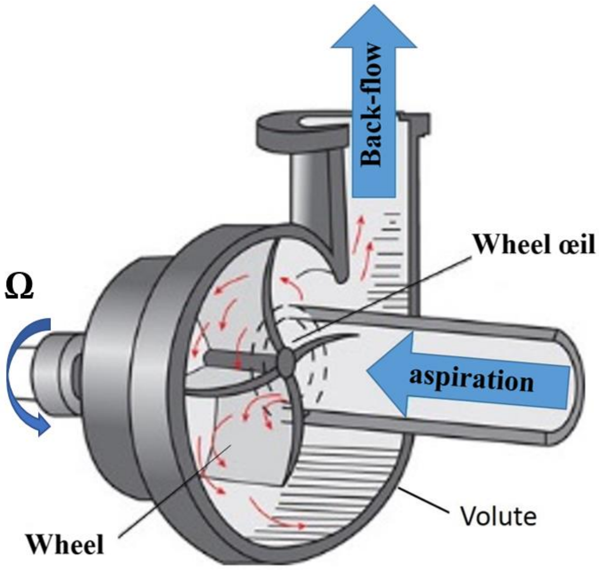

Figure 2.12. Block diagram of a centrifugal pump

The water arrives in the axis of the device through its suction circuit (vacuum or aspiration circuit), which is coupled to the impeller (rotor). The centrifugal force then projects it towards the outside of the turbine via the discharging circuit (back-flow). As the section of the collector increases, the water acquires a great kinetic energy, which is transformed into pressure energy (pressure lift). The use of a diffuser (fixed impeller) at the periphery of the impeller allows for a reduction of the energy loss.

This pump is essentially characterized by: (Figure 2.13)

- Rotation speed (Ω) ;
- Characteristic curve: Total Manometric Head (TMH) as a function of flow rate: H=f(Q);
- Efficiency curve: which characterizes the maximum efficiency in the vicinity of which the pump must be used;
- Power curve: This curve shows the power absorbed at the pump shaft;
- Net Positive Suction Head NPSH, which is the minimum NPSH that the pump must have to avoid cavitation. It is usually given by the manufacturer in the form of a curve as a function of the flow rate, on the same graph as the TMH curve.

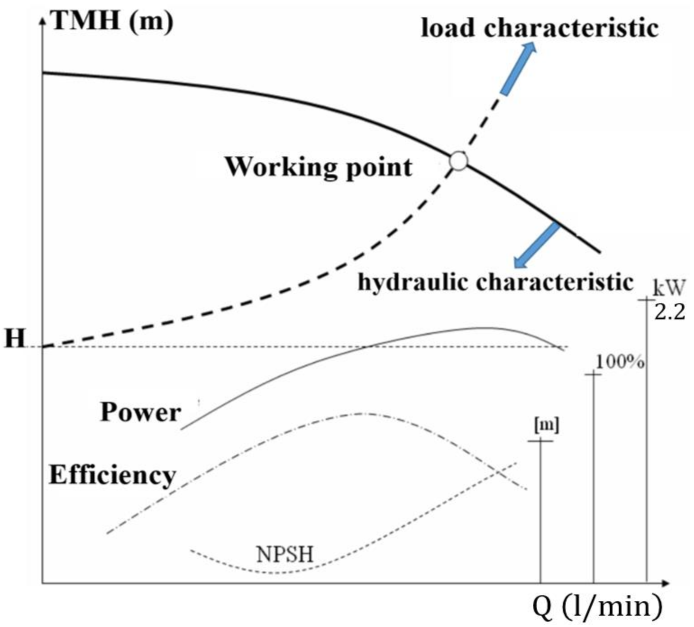

Figure 2.13. The characteristic curve of a centrifugal pump.

The relationship between head (H) and pressure (P) is written as follows:

$$P=ƒgH \tag{2-41}$$

With:

P [Pa]: Pressure ($1\ \text{Pa} = 10^{-5}\text{bar}$)

H[m]: Height of fluid

g [m/s]: Gravity acceleration (9.81 m/s)

ƒ [Kg/m^3] : fluid density (ƒ = 1000 Kg /m^3 for water)

The flow pressure is determined by equation (2-42) [86]:

$$P = a\Omega^2 + b\Omega\, Q + c\, Q^2 \tag{2-42}$$

Where a and b are the pump parameters, c is the parameter corresponding to the pump losses, Ω is the rotation speed of the pump shaft (in rad/s), and Q is the flow rate in l/min. These parameters are given in Annex A.

The torque of the centrifugal pump, which represents the IM (Induction machine) load torque [86], is given by:

$$T_r = a\, Q^2 + b\, Q\, \Omega \tag{2-43}$$

The hydraulic characteristics of a motor pump refer to its ability to generate flow and pressure under various operating conditions, including different frequencies. As the frequency changes, the hydraulic performance of the pump changes as well, impacting its ability to deliver the desired flow rate and pressure. To ensure optimal performance and efficiency in different applications, it is essential to understand the hydraulic characteristics of a motor pump at variable frequencies. Hydraulic testing and analysis can be used to determine the pump's performance curves, which show the relationship between flow rate and pressure. Figure (2.14) shows the characteristics curves of a 2.2 KW high-pressure centrifugal pump tested at three different frequencies (30, 40, and 50 Hz). The parameters of the pump used in this work are presented in Annex 01.

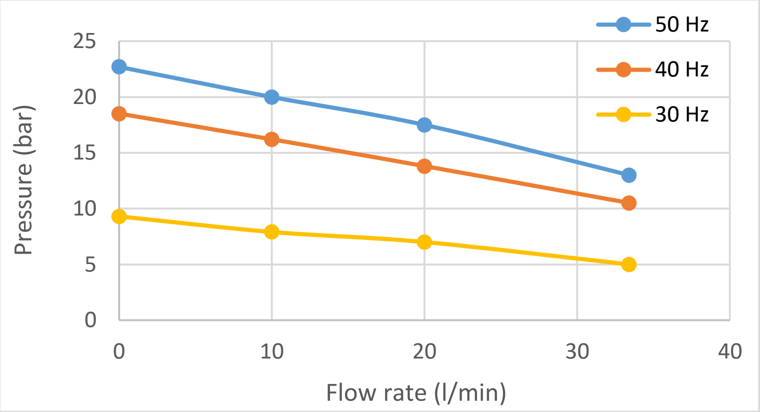

Figure 2.14. Characteristics of a variable speed centrifugal pump.

2.7.RO membrane modeling

In the literature, many models describe the behavior of the membrane during its operation. It is a semi-permeable device, which separates the liquid under the pressure gradient.

The water permeability coefficient, A, can be determined by its relation to water flux J_w. The water flux across the membrane is described by the solution-diffusion model [87, 88].

$$J_w = A\,(\Delta P - \Delta\pi) \qquad (2\text{-}44)$$

The A coefficient can be easily calculated by measuring J_w using deionized water, which removes the effects of osmotic pressure. This value of A is known as the "pure water permeability coefficient". However, certain solution chemistries can cause physicochemical alterations in the membrane, such as selective layer deswelling induced by salt [89]. These alterations in the swelling of the selective layer cannot be detected in filtration experiments using only pure water. Changes in the swelling of the selective layer can significantly impact the overall thickness of the membrane and, as a result, affect the resulting A coefficient [89].

ΔP is the imposed hydraulic pressure and Δπ is the osmotic pressure difference between the feed and permeate sides of the membrane active layer.

$$\Delta\pi = \pi_f - \pi_p \qquad (2\text{-}45)$$

$$\Delta P = P_f - P_p \qquad (2\text{-}46)$$

To prevent the passage of pure solvent through a semi-permeable barrier into a solution by osmosis, osmotic pressure must be applied. Equation (2.47) is used to calculate the difference in osmotic pressure across the active layer of a membrane between the feed and permeate sides.

$$\Delta\pi = K_{nacl}(T_{nacl} + 273)\frac{C_{nacl}}{1000 - \frac{C_{nacl}}{1000}} \qquad (2\text{-}47)$$

The membrane recovery rate is an important factor in the reverse osmosis (RO) process, as it can significantly affect the efficiency and cost of the process. The membrane recovery rate is defined as the ratio of the volume of permeate (i.e., the purified water) produced by the RO membrane to the volume of feed water that enters the membrane system. In other words, it represents the percentage of feed water that is converted into permeate, defined by:

$$R = \frac{Q_p}{Q_f} \times 100 \qquad (2\text{-}48)$$

Exceeding the maximum recovery rate can result in scaling and fouling of the RO membrane, which can reduce the efficiency of the system and lead to higher operating costs. Therefore, the maximum recovery rate should be carefully determined based on the specific conditions of the RO system and should monitored and controlled to ensure optimal performance and membrane lifespan. In addition, a high recovery rate can reduce the overall permeate flux and hence increase the energy consumption of the process.

A second factor that is no less important than the recovery rate is the selectivity of a membrane. This is defined by the rejection rate Y (or retention rate) of the species that the membrane is supposed to retain.

$$Y = 1 - \frac{C_p}{C_f} \qquad (2\text{-}49)$$

With C_p and C_f are respectively the concentration of the produced water and that of the feed water.

The rate of permeate flow, denoted by Q_p, is determined by several factors including the active surface area of the membrane(S_m), the water permeability coefficient (A), and the feed flow pressure(P_f). This relationship is expressed mathematically as follows:

$$Q_p = A.[P_f - \Delta\pi].S_m \qquad (2\text{-}50)$$

The feed flow rate is one of the important operating parameters in a desalination plant, as it affects the overall efficiency and productivity of the system.

The feed flow can vary depending on the size and capacity of the desalination plant, as well as the specific technology used for the desalination process. In general, a higher feed flow rate can result in a higher production rate of fresh water, but can also require more energy and resources to maintain the desired level of performance. Optimal feed flow rates are determined based on the specific conditions and requirements of the desalination system.

2.8.Conclusion

The purpose of this chapter is to present the mathematical models of a proposed PV-RO desalination system. These models will be used in subsequent chapters for system control, simulation, and implementation.

The chapter begins with a description of photovoltaic cells, modules, and arrays, along with their characteristic curves. It also presents the power converters used in the proposed desalination system, illustrating their power circuit and electrical behavior.

The induction motor is modeled in a synchronous reference frame, which facilitates understanding of motor control operations. Additionally, the chapter describes the centrifugal pump model and its head-flow characteristics. Finally, the RO membrane is presented.

Chapter 03

Partial shading effects on PV generator

Chapter 3: Partial shading effects on PV generator

3.1.Introduction

Reverse Osmosis (RO) desalination systems powered by conventional electrical sources have been a major research topic. These systems generally operate stably throughout their operational period to meet production requirements. However, desalination systems powered by non-conventional electrical sources, such as wind and solar, pose greater challenges due to fluctuating and intermittent electrical power levels. The variable efficiency and output values (pressure and flow) of the moto pumps may exceed or fall below the limits of the desalination membranes, causing damage in the short or medium term.

The efficiency of solar photovoltaic (PV) energy conversion to electrical energy is relatively low, and the PV characteristics are nonlinear and dependent on environmental conditions. To ensure that the PV desalination system operates at its maximum power point (MPP), an algorithm known as a Maximum Power Point (MPP) tracker is essential. However, during partial shading, the curve exhibits multiple power peaks with unpredictable trajectories and shapes, making it challenging for designers of MPPT algorithms to track the global maximum power point (GMPP).

In this chapter, five literature methods have been explained, and DSpace 1104 has been used for implementation and validation. A comparative study was conducted to choose the best method for the entire system.

3.2.MPPT techniques background

Generally, the photovoltaic source is associated with controlled converters whose purpose is to track the maximum power point (MPP) of the P-V curve to ensure a better energy yield of the system. For a PV array under uniform irradiance conditions (UIC), conventional MPP tracking (MPPT) algorithms can effectively achieve their goal [90] due to their simplicity of implementation. The concept of these conventional methods is, in fact, similar. It is based on perturbing the system voltage/duty cycle and checking the evolution of the extracted power, leading to an improvement in the overall system efficiency. However, under partially shaded conditions (PSC), these methods present certain insufficiencies.

In PSCs, PV modules do not receive equal solar irradiance, and the array PV characteristic may contain a maximum peak named GMPP (Global Maximum Power Point) and one or multiple peaks with different power values seen as LMPP (Local Maximum Power Point) [91]. In most cases, PSCs are inevitable, especially in PV systems installed in urban areas or places with significant cloud cover. Therefore, PSC analysis and mitigation effect studies have been conducted, offering appropriate technical solutions. Accordingly, numerous MPP tracking methods for PV systems under PSC have been tested [92].

Various MPPT control techniques, more or less efficient depending on their operating principle and complexity, appear regularly in the literature [93, 94]. Figure (3.1) presents a general classification of the different MPPT controls published in the literature.

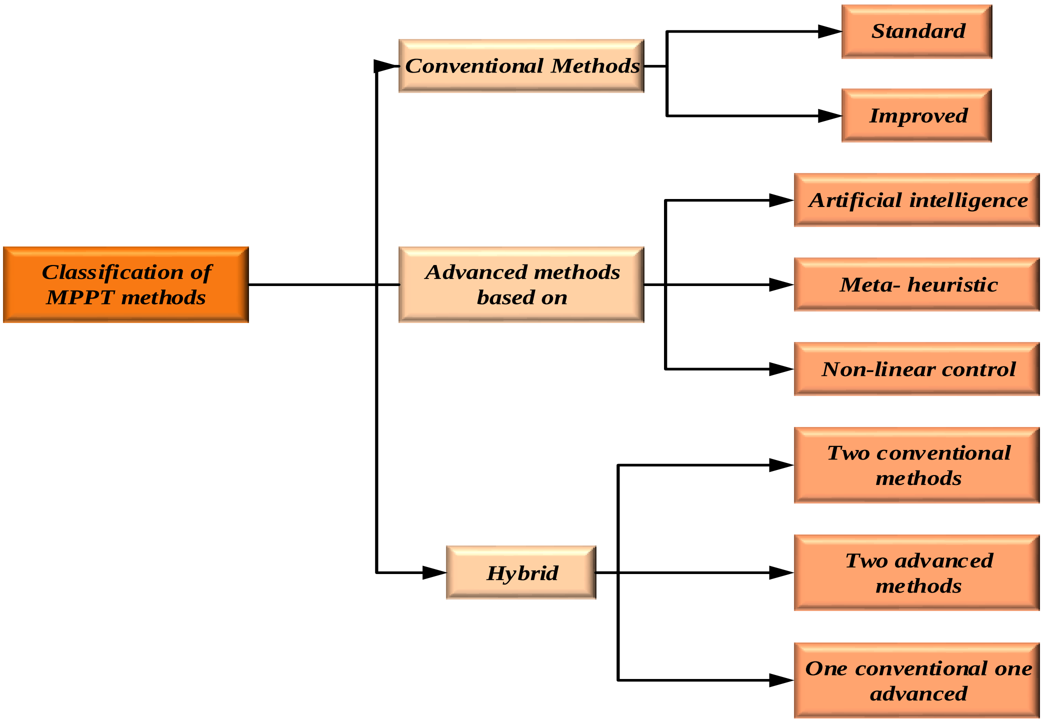

Figure 3.1. Basic classification of MPPT techniques.

A variety of MPPT methods for maximum power point tracking under partial shading conditions have been developed and can be found in literature reviews such as[95-98]. Among these strategies are those involving the application of intelligent and meta-heuristic search algorithms [99]. Other GMPPT methods have been used for the same objective. These methods include enhanced adaptive P&O (EA-P&O) [100], an artificial vision algorithm [101], a bypass diode-scanning approach [102], and the method based on the maximum power that the series and parallel configuration of PV cells are able to deliver [103]...etc.

As mentioned above, there are several MPPT techniques dealing with partial shading conditions cases in the literature, which are summarized in Tables (3.1) and (3.2). However, for a designer, it is difficult to make the right choice for a specific application. Each application has its own criteria like efficiency, tracking speed, cost, accuracy, implementation complexity, etc.

Table 3.1: Tabular analysis of different global MPPT techniques for shading conditions

Type of method	Name of techniques	Year of publication	Reference	Converters used	Efficiency	Algorithm complexity	Tracking & convergence speed
advanced Methods	ESC	2016	[104]	Boost	99.87 %	High	2.1 s
	PSO	2018 2017	[105] [106]	Boost Buck-Boost	99.82 % -	High Medium	Two times faster ≈ 1.5 s
	ANN	2013	[107]	Boost	High (no oscillation around MPP)	High	Quick convergence
	GWO	2016	[108]	Boost	99.92%	High	Fast
	GA	2013	[109]	Boost	Improves	High	Fast convergence
	Fuzzy	2019	[110]	-	Low	Medium	Medium
	NN	2020	[111]	-	>98%	High	Fast

Table 3.2: Tabular analysis of different global MPPT techniques for shading conditions

Type of method	Name of techniques	Year of publication	Reference	Converters used	Efficiency	Algorithm complexity	Tracking & convergence speed
Hybrid methods	ANN-PO	2017	[112]	Boost	98.26 %	Medium	Fast
	GWO-PO	2016	[113]	Boost	Above99.91%	Medium (only tuning two parameters)	Fast 0.015s
	PSO-PO	2017 2015 2014	[114] [115] [116]	Boost Boost Boost	- Above 99.50% -	Medium Medium Medium	0.9 s Faster than PSO Faster than PSO

Abbreviations: ESC, Extremum Seeking Control; ANN, Artificial Neural Networks; GA, Genetic Algorithm; GWO, Gray Wolf Optimisation; PSO, Particle Swarm Optimization.

3.3.MPPT techniques used in this thesis

Maximum power point tracking (MPPT) is a crucial component in photovoltaic (PV) systems, as it ensures that the system operates at its maximum power output point under varying operating conditions. There are several MPPT techniques available, each with its own advantages and limitations. Choosing the right MPPT technique depends on various factors, including the type of PV system, environmental conditions, and cost considerations. By selecting the appropriate MPPT technique, the performance and efficiency of the PV system can be optimized, resulting in improved energy production and cost savings over the system's lifetime.

In this chapter, various MPPT techniques were tested and implemented, such as PO, SMC, classical ESC, and other hybrid and modified ESC methods. These techniques were implemented and compared with the nonlinear sliding mode MPPT to determine which one is best suited for the whole system.

3.3.1. Perturb and Observe (PO)

The Perturb and Observe (PO) algorithm is most commonly used in PV systems applications to find the Maximum Power Point (MPP) due to its ease of implementation and simplicity [117, 118]. It is based on the measurement of V_{pv} and I_{pv}, making it an easy method with an excellent efficiency. However, its major disadvantage is the oscillations around the maximum power point (MPP), and it fails to track the Global MPP (GMPP) under shading conductions. The system will be only able to respond very slowly to rapid changes in temperature or insolation. Figure (3.2) shows the flowchart of the Perturb and Observe algorithm, where α is the duty cycle.

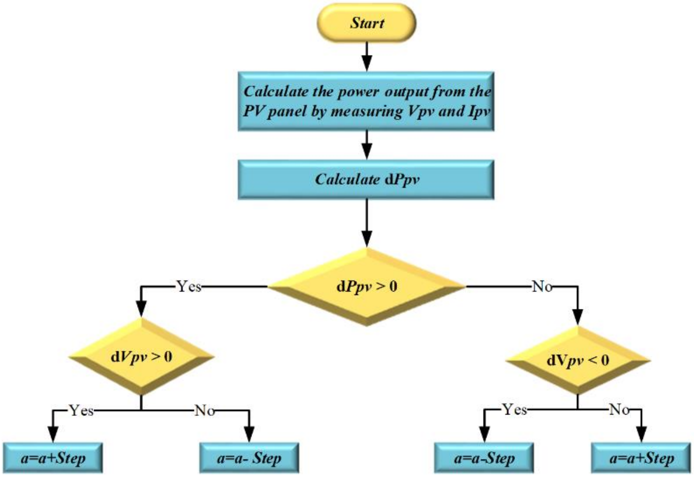

Figure 3.2. Flowchart of PO algorithm.

3.3.2. Sliding mode control

This work details sliding-mode controller (SMC), a nonlinear tracking technique that quickly and accurately determines the maximum power point (MPP) in PV systems. The basic idea of the methodology is to control the DC–DC converter by sensing the inductance’s current. First, the best sliding surface has to be chosen according to the application. This nonlinear technique controls the system's nonlinear parameters, and its main advantage is its independence regardless of the PV array or configuration size.

As part of the robust control system, this control strategy has generally been used as a reliable tool for regulating electromechanical systems and parametric variations. In recent years, the first-order and higher-order sliding mode (super-twisting) have been successfully implemented as an MPPT algorithm [119]. In this work, only the first order-sliding mode is used. The concept of the approach can be introduced by selecting the sliding surface S. Slotine [120] proposes in a common equation of the surface used in electromechanically based systems, as shown in (3.1). This equation relates the sliding surface, the tracking error 'e', and the relative degree 'r'.

$$\mathrm{S} = \left(\frac{\mathrm{d}}{\mathrm{dt}} + \gamma\right)^{\mathrm{r}-1} \mathrm{e(t)} \tag{3.1}$$

The sliding surface S is defined by:

$$\mathrm{S} = \frac{\mathrm{dP_{pv}}}{\mathrm{dV_{pv}}} = \mathrm{V_{pv}}.\frac{\mathrm{dI_{pv}}}{\mathrm{dV_{pv}}} + \mathrm{I_{pv}} \tag{3.2}$$

Based on the observation of the operation region shown in Figure (3.3), the method involves increasing or decreasing the duty cycle α with a pre-set Δα increment following the sign of the surface in order to approach the optimal MPP point.

$$\alpha(k) = \begin{cases} \alpha(k-1) + \Delta\alpha & for \quad S > 0 \\ \alpha(k-1) - \Delta\alpha & for \quad S < 0 \end{cases} \tag{3.3}$$

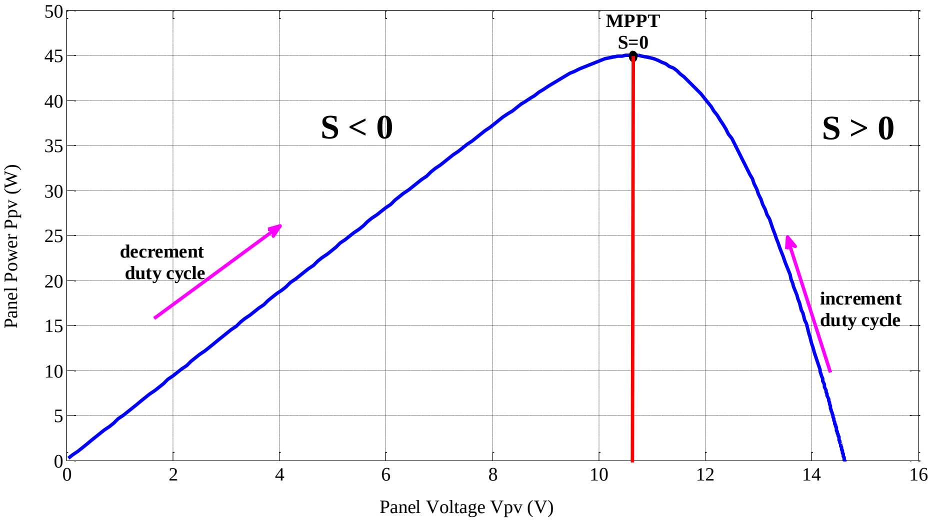

Figure 3.3. Principle of MPPT control by sliding mode.

The PV system achieves the MPP when the sliding surface equals zero (S=0). To ensure this over the entire operating range, it is necessary for time derivative of the quadratic Lyapunov function ($V = \frac{1}{2}S^2$) to be negative, as shown in equation (3.4):

$$\dot{V} = S \times \dot{S} < 0 \tag{3.4}$$

The SMC is composed of two parts: α_{eq} and α_n. The first one deals with the equivalent control quantity and the second one provides the stabilization part, as shown in equations (3.5) and (3.6), respectively:

$$\alpha_{eq} = 1 - \frac{V_{pv}}{V_L} \tag{3.5}$$

$$\alpha_n = -k_{smc} S \tag{3.6}$$

The sliding surface for the tracking error is defined as the incremental conductance condition to extract the maximum power, as shown in Figure (3.4).

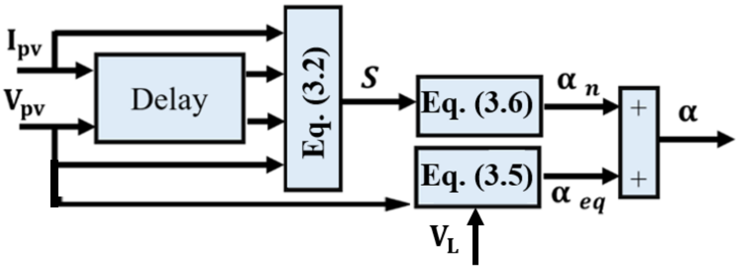

Figure 3.4. Sliding mode control (SMC) diagram.

The duty cycle variation within the allowable range can be guaranteed if the control gain k_{smc} is not selected too large ($k_{smc} > 0$). In fact, it is chosen as the inverse of continuous variation of the duty cycle in the specified range and can be ensured without violation if the scaling constant $k_{smc}$is not selected too large. The control gain is chosen as the inverse of the maximum equivalent load on the DC side: $k_{smc} \leq |R(max)|$, [45]:

$$R(max) = \frac{V_{dc\_min}^2}{P_{min}} \tag{3.7}$$

Where V_{dc-min}denotes the minimum value of the PV voltage obtained with regular irradiance changes, while P_{min} expresses the minimum extracted power after sunshine. The sliding mode ensures the stability and robustness of the system. However, the main disadvantages of this type of control include reticence phenomena, variable switching frequency, and the significant steady state error. To mitigate these associated SM control issues, other studies have included an integral action term [121, 122]. However, undesirable disturbances and significant overshoot have been observed.

3.3.3. Extremum Seeking Control (ESC)

The foundations of extremum-seeking control can be traced back to the early 1920s in the work of Leblanc on the search of the resonance peak of an electromechanical system [123]. The nonlinear and adaptive nature of such control is clearly shown in [124]. Although there are different extremum-seeking algorithms, it is important to make a significant analytic effort to establish the stability regions of a large number of reported applications [125]. The block diagram of an extremum-seeking problem is depicted in Figure (3.5), where an integrator governs the equations describing the system behavior:

$$\frac{dx}{dt} = K.\varepsilon \tag{3.8}$$

Where $\varepsilon = \mp 1$ and K is $constant$

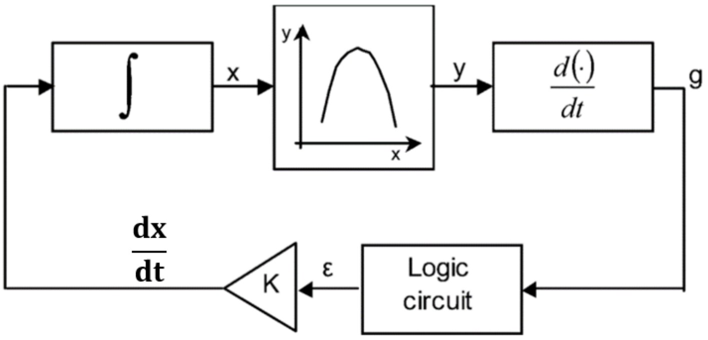

Figure 3.5. Block diagram of gradient method.

A differentiator

$$g = \frac{dy}{dt} \tag{3.9}$$

If g < 0, ε changes sign, whereas if g > 0, ε keeps its sign. Figure (3.6) illustrates abstract cases of the extremum-seeking mechanism.

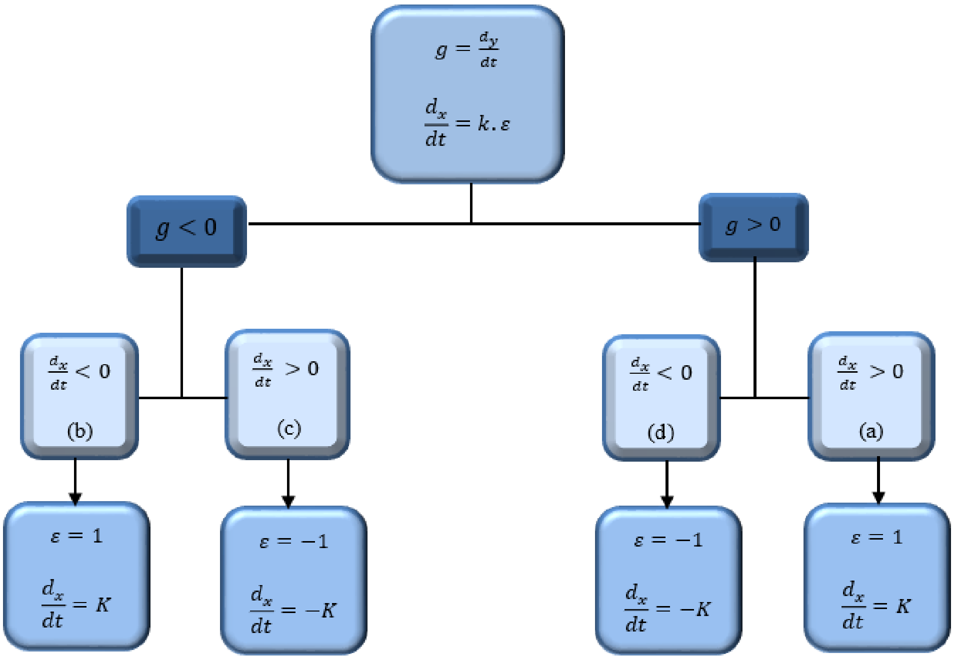

Figure 3.6. Illustrative cases of extremum-seeking mechanism.

In the case of a solar array, the extremum-seeking algorithm will force the PV system to approach to the maximum power point by increasing or decreasing the voltage at the array terminals with a constant time-derivative value. The variables x and y of the MPPT function depicted in Figure (3.6) correspond, in our work, to the panel voltage V_{pv}, and the panel power P_{pv}, respectively. The variation of V_{pv} with a constant time-derivative is achieved by imposing such behavior on the converter duty cycle α.

The expression of $\overline{V_{pv}}$ is given by:

$$\overline{V_{pv}} = \overline{V_L}(1 - \alpha) \tag{3.10}$$

Where $\overline{V_{pv}}$ is the PV mean voltage and $\overline{V_L}$is the mean load voltage

The derivative of the power P delivered by the solar array with respect to the duty cycle can be calculated using the following equation:

$$\frac{dP_{pv}}{d\alpha} = \frac{dP_{pv}}{dV_{pv}}\frac{dV_{pv}}{d\alpha} \tag{3.11}$$

By replacing V_{pv} with its expression (3.10), the derivative of the power P delivered by the solar array with respect to the duty cycle can be calculated:

$$\frac{dP_{pv}}{d\alpha} = -V_L\frac{dP_{pv}}{dV_{pv}} \tag{3.12}$$

Hence,

$$\frac{d^2P_{pv}}{d\alpha^2} = {V_L}^2 \frac{d^2P_{pv}}{d{V_{pv}}^2} \qquad (3.13)$$

At the maximum power point

$$\frac{dP_{pv}}{d\alpha} = 0 \qquad (3.14)$$

Which implies

$$\frac{d^2P_{pv}}{d\alpha^2} < 0 \qquad (3.15)$$

We can conclude from (3.14) and (3.15) that the solar array power is a concave function of the duty cycle. As a result, the Extremum Seeking algorithm can be applied directly to the converter duty cycle, which controls the power panel. The search for the maximum power point would result in a trajectory through the P-V characteristics of the PV array, characterized by a voltage triangular waveform in the time domain.

3.3.4. Conventional Sinusoidal Extremum Seeking Control(ESC sin)

The following figure represents the sinusoidal ESC principle applied to the PV source. Given a nonlinear input-output map, if a sinusoidal signal of small amplitude is added to the input signal V_{pv}, the output signal P_{pv}, oscillates around its mean value. It can be observed that when the signal P_{pv}, is multiplied by a sinusoidal of the same frequency and phase, the multiplier output $\frac{d\,P_{pv}}{dt}$ is positive before the MPP and negative at the right side of the MPP.

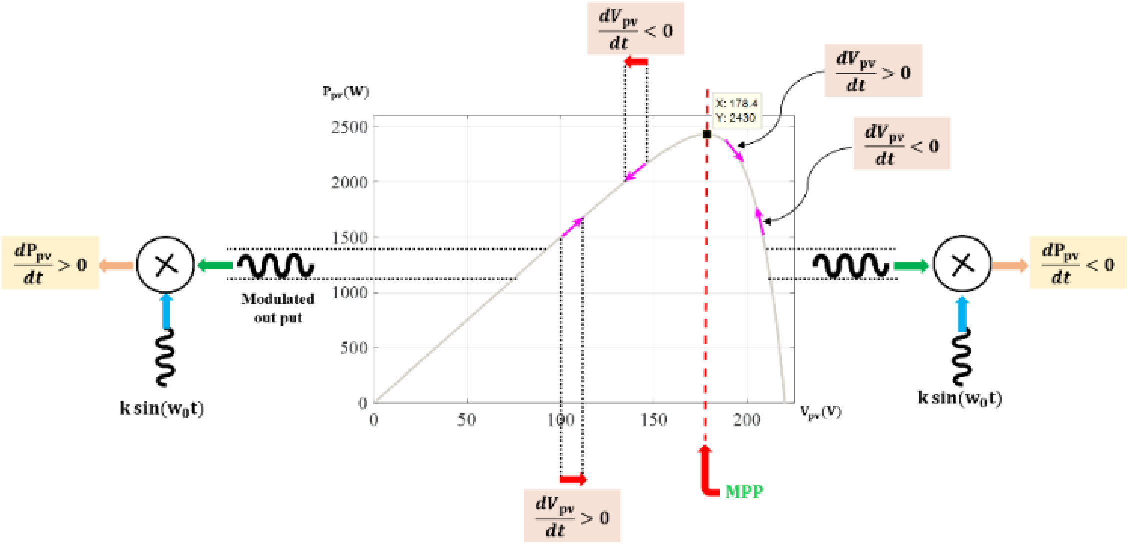

Figure 3.7. Sinusoidal ESC principal applied to PV generator.

The approach can be applied to the PV system by the schema shown in Figure (3.8). The schema consists of several components: an integrator, two filters (High Pass Filter HPF and Low Pass Filter LPF), and a small sinusoidal signal. This signal is added to the PV power at the same frequency as the dither signal, which is extracted through a High Pass Filter (equation (3.16)).The gradient function is obtained by modulating the signal through the addition of a sinusoidal perturbation signal ($\sin(\omega t)$) with a relatively high frequency. Then, the low-pass filter (equation (3.17)) eliminates unnecessary components, and the resulting signal represents the estimated gradient [126]. The output of the LPF is applied to an integrator and added to $\mathrm{k} * (\sin(\omega_0 t))$ to obtain the reference PV voltage $\mathrm{V}_{\mathrm{pv}}^{*}$.

$$\mathrm{HPF} = \frac{\mathrm{s}}{\mathrm{s}+\omega_{\mathrm{h}}} \tag{3.16}$$

$$\mathrm{LPF} = \frac{\omega_{\mathrm{l}}}{\mathrm{s}+\omega_{\mathrm{l}}} \tag{3.17}$$

To ensure the convergence of the ESC controller, the cut-off frequency ω_h must be lower than the frequencyω_l, and both of these frequencies are much smaller than ω_0[127].

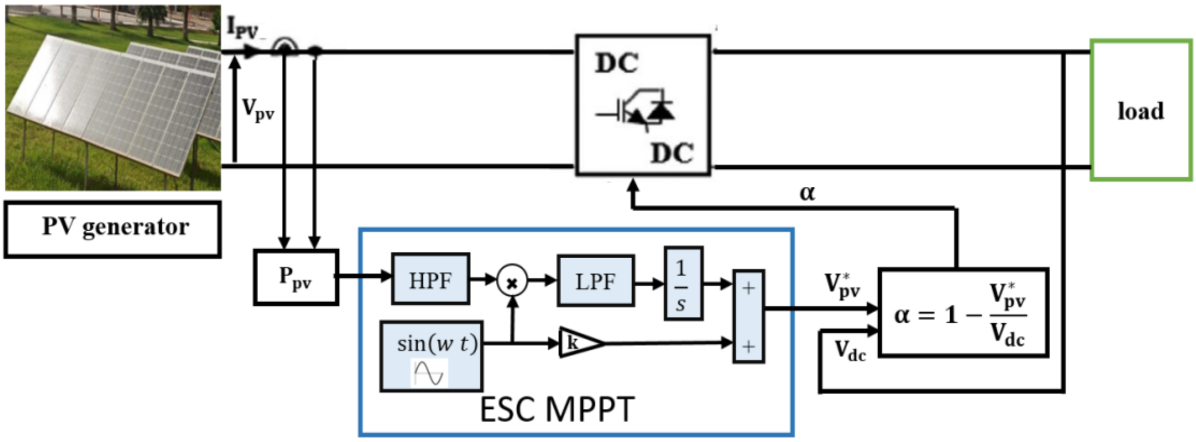

Figure 3.8. Scheme of the ESC-based MPPT

The main steps of the ESC-based algorithm can be summarized as follows:

Step1: Inject a small perturbation signal called the dither signal ($\mathrm{k}\sin\omega_0 t$)) with a relatively high frequency to an estimate of the optimal input (Vpv∗).

Step2: The PV power will have a sinusoidal component with the same frequency as the dither signal, which is extracted through a High Pass Filter (HPF). Due to the nature of the PV characteristics, this sinusoidal component is either in phase with the dither signal if the voltage is less than the MPP or out of phase if the voltage is larger than the MPP.

Step3: multiply the resulting sinusoid with the dither signal, yielding a shifted sinusoid with a positive or negative DC component if the multiplied signals are in phase or out of phase, respectively.

Step4: The DC component, which is extracted through a Low Pass Filter (LPF), represents a signal proportional to the gradient of the PV power.

Step5: Integrate it and multiply it by a gradient update gain so that the voltage estimate asymptotically approaches the MPP.

3.3.5. Extremum Seeking Control modified (ESC modified)

One of the newest and most efficient methods to track the maximum power point in solar systems and increase the energy yield in photovoltaic systems during abrupt changes in atmospheric conditions is the modified Extremum Seeking Method (ESM modified) proposed by [128]. This method uses a slow periodic perturbation $(\sin(w_p t))$ added to the estimated value like the classical ESC to continuously drive the system to the optimal point [129]. To increase system performance, the modified ESC adds a second low-pass filter and an integrator, as illustrated in Figure(3.9).

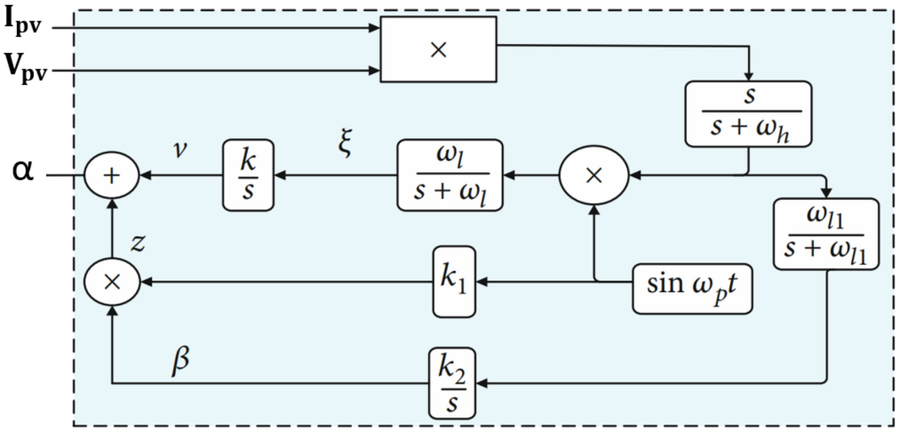

Figure 3.9. Block diagram of the modified ESC algorithm applied to the PV system.

3.3.6. Hybrid Mode SM-ESC

The SM-ESC is developed through the combination of SMC and ESC. Compared to ESC, the SM-ESC method not only enhances the robustness of MPPT but also ensures that it can enter the sliding mode with the shortest time, regardless of the initial state of the system, thanks to the concept of the sliding mode surface. Assuming that P_{MPP} represents the maximum point of the objective function $P_{pv} = f(V_{pv})$, the sliding mode motion aims to approach P_{MPP} by following a function that increases with time, regardless of changes in the gradient of the objective function. In Figure (3.10), the sign(s) proposed in ESC is replaced by the sliding layer control strategy, which utilizes the following function [130]:

$$sat(s,\beta) = \begin{cases} 1 & s > \beta \\ \frac{s}{\beta} & |s| \leq \beta \\ -1 & s < -\beta \end{cases} = \begin{cases} sign(s) & |s| > \beta \\ \frac{s}{\beta} & |s| \leq \beta \end{cases} \tag{3.18}$$

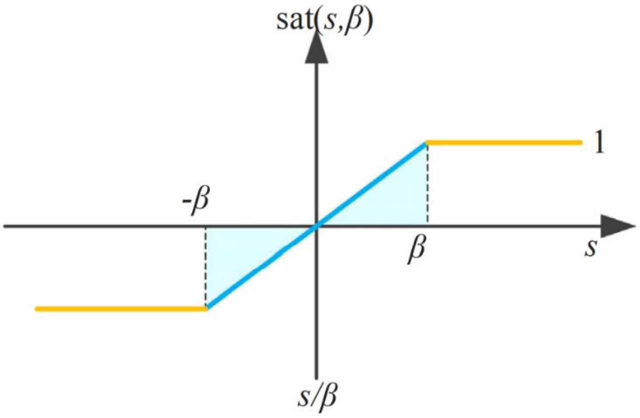

Figure 3.10. The model of the sliding layer.

Reference [131] proposes related work on the SM-ESC method for MPPT used with a wind turbine. We apply this principle on the PV system to achieve ideal switching without high-frequency noise and reduce power losses. The extremum search process implemented by the SM-ESC method is shown in figure (3.11), where the left and right neighborhood width of the maximum point are defined. The extreme point of $P_{pv} = f(V_{pv})$ is (Vpvmax, Ppvmax). As shown in Figure (3.11), the area is divided into two zones. Zone I is the neighborhood of the optimal point, and the other is the sliding surface. In zone I, the method parameters have an influence on the MPPT speed.

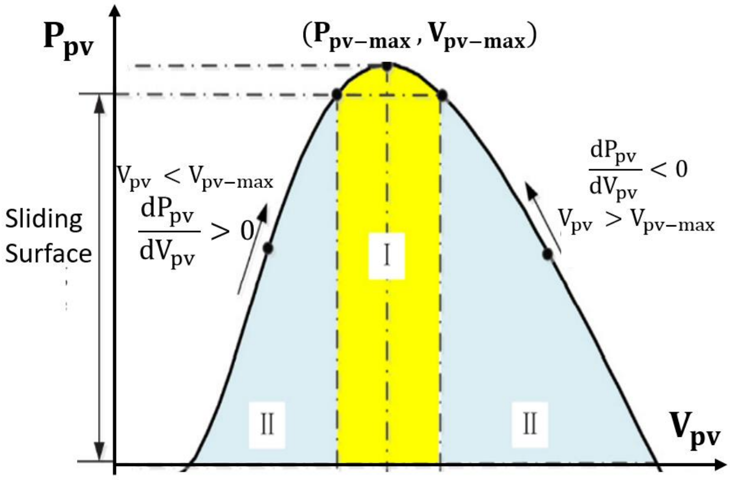

Figure 3.11. Extremum search process of SMESC method.

3.4. Experimental results

To implement and validate the chosen control strategies, an experimental test bench shown in figure (3.12), was built within the electrical engineering laboratory of Biskra (LGEB).

It mainly consists of two PV modules of 170 Wp, with the parameters given in table (3.3); a boost converter composed of one SKM50123, IGBT module, switched at 15 kHz, that supply a variable resistive load. A DSpace 1104 card from Texas instruments with a TMS32F240 DSP using the Matlab/Simulink environment is used to implement the control algorithms used in this thesis. An interface card is used to adapt the control signal levels between the DSpace board and the power converter. Voltage and current sensors are used to measure the different currents and voltages. To test the robustness of the proposed algorithms for maximum power point tracking (MPPT), three cases are distinguished.

Table 3.3. PV module parameter

Type	Monocristallin (Sharp)NTR5E3E/ NT175E1
Maximum power	$P_{max} = 85$ W
Optimum current	$I_{op} = 4.77$ A
Optimum voltage	$V_{op} = 17{,}9$ V
Open circuit voltage	$V_{oc} = 22$ V
Short circuit current	$I_{cc} = 5{,}2$ A

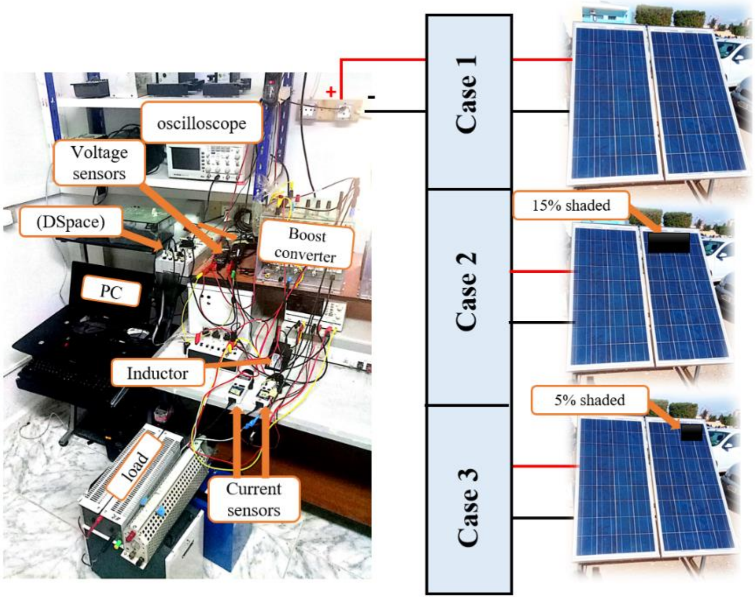

Figure 3.12. Test bench for experimental validation of the proposed algorithms.

On February 9th, 2022, the conventional PO MPPT was implemented in the healthy case, as shown in figure (3.13). The modified ES, ES (Extremum Seeking) and SM (Sliding Mode) control strategies were tested for three scenarios on the same day (10th February 2022). The hybrid SM-ESC and modified ES-SM were tested for the same scenarios but in another day (January18th, 2022). The first one is the healthy case (without shading), for which the PV generator was tested under different loads, and the characteristics were simulated. As shown in figure (3.13), in such situation, the so-called global MPPT point (GMPP) of 150 W at 950 W/m² was tracked. Afterwards, the generator underwent another scenario where the GPV was shaded by 15 %. In the last scenario, the GPV was shaded by a lesser ratio of about 5%.

As depicted in Figure (3.13), there are three cases shown. The bleu curve represents the healthy case with one pick of 150 W, which is called global MPP. The red curve presents the second case with two picks, the global MPP of 137.6 W and the local MPP of 64 W. The green curve corresponds to the third case with two picks, the global MPP of 111 W and local MPP of 58 W. One can notice the presence of local optimum points located on the left side of the I-V curve.

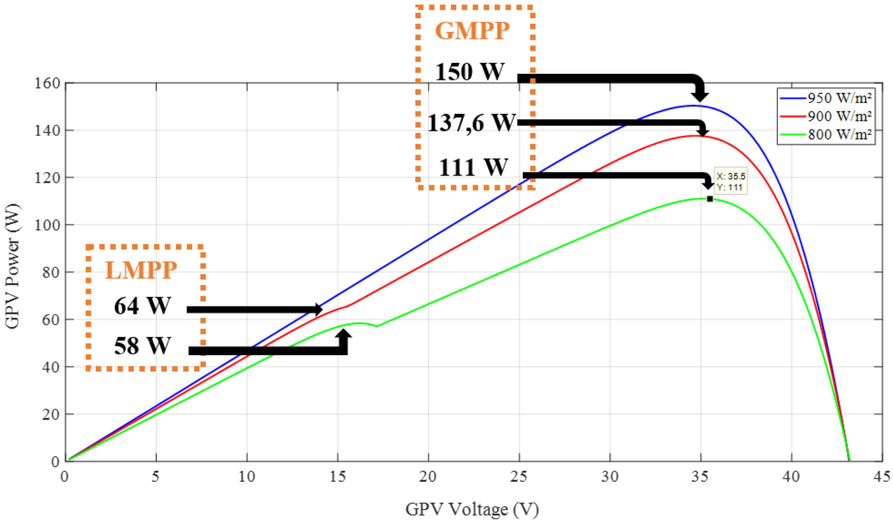

Figure 3.13. P-V curve of the simulation shading applied on the GPV.

In the PO test, the irradiance level remains stable at 950 W/m², as shown in Figure (3.14). The figure has two parts: the first one is from 0s to 15s before connecting the PO, which is the open circuit part. The second part, which occurs after 15s, involves the application of the PO. It is clear that PO takes only 0.2s to track the MPP with significant oscillation.

The significant oscillations demonstrated by the Perturb and Observe (PO) method have led us to eliminate it as an option for the next experimental test.

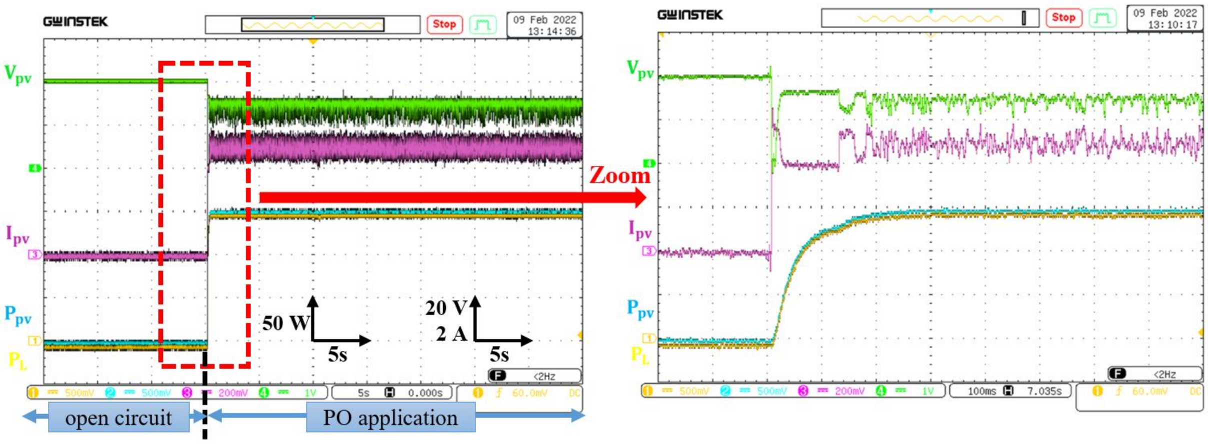

Figure 3.14. Power, Voltage and Current graphs of PO method for healthy case.

Case 1: The practical responses of the load side power and PV power, voltage, and current are shown in Figure (3.15). These results concern the application of the SMC and ESC algorithms under load variation. The curves are divided into three time windows. In the first time span, an initial open circuit phase is distinguished, followed by the implementation of both algorithms, and finally, a load variation is applied.

During the first phase of the experiment, which lasted from 0s to 40s, the SMC strategy was used, while the ESC strategy was used for only 15s during the second phase. Both methods were able to track the global MPP, resulting in a rapid increase of PV power to its maximum value of 150W. The $\left(I_{pv}, V_{pv}\right)$ dipole then converged towards their optimum values of 4,3A and 35V. However, the SMC results were characterized by chattering phenomena, caused by the application of the ‘sign’ component. In contrast, the curves of the ESC-based strategy were smooth.

The load change occurred at 70s using the SMC and 32s using the ESC. The dynamic performance of the two methods differed significantly. The SMC algorithm was able to follow the optimum power regardless of the load changes and extract it in just 2 seconds, thanks to the stabilization control. In contrast, the ESC strategy took longer to re-track the optimum point, which took 4 seconds.

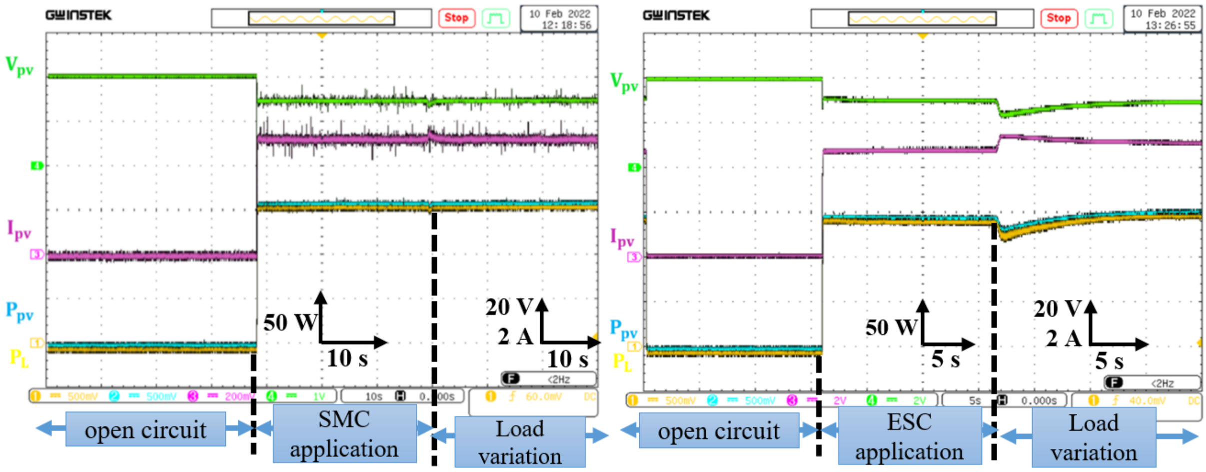

Figure 3.15. Power, Voltage and Current graphs of SMC, ESC methods for case 1.

In the same case, a practical test was performed on three other methods: modified ESC, SM-ESC (Sliding Mode Extremum Seeking Control), and hybrid sliding mode (SM) with modified ESC.

Figure (3.16) shows the practical responses of the load side power, PV power, PV voltage, and PV current using the modified ESC. During the transitional regime at start-up, the modified ESC is very fast to stabilize, while it takes 1.5s for the load changing (at 32s).

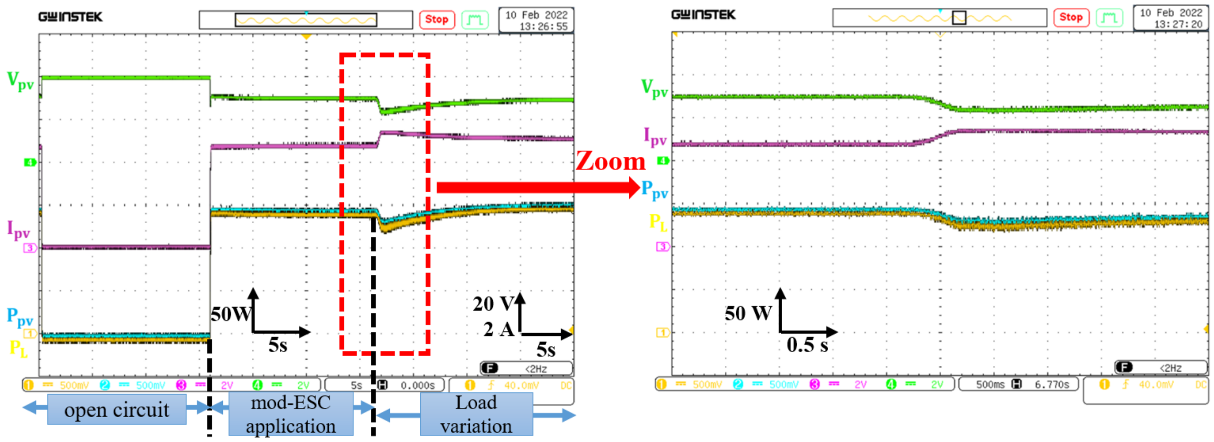

Figure 3.16. Power, Voltage and Current graphs of modified ESC method for case 1 and its zoom.

Figure (3.17) illustrates the curves of the PV and load power with a zoomed-in view of two important points: at start-up and during a load change. It takes 1s for the powers to reach the MPP.

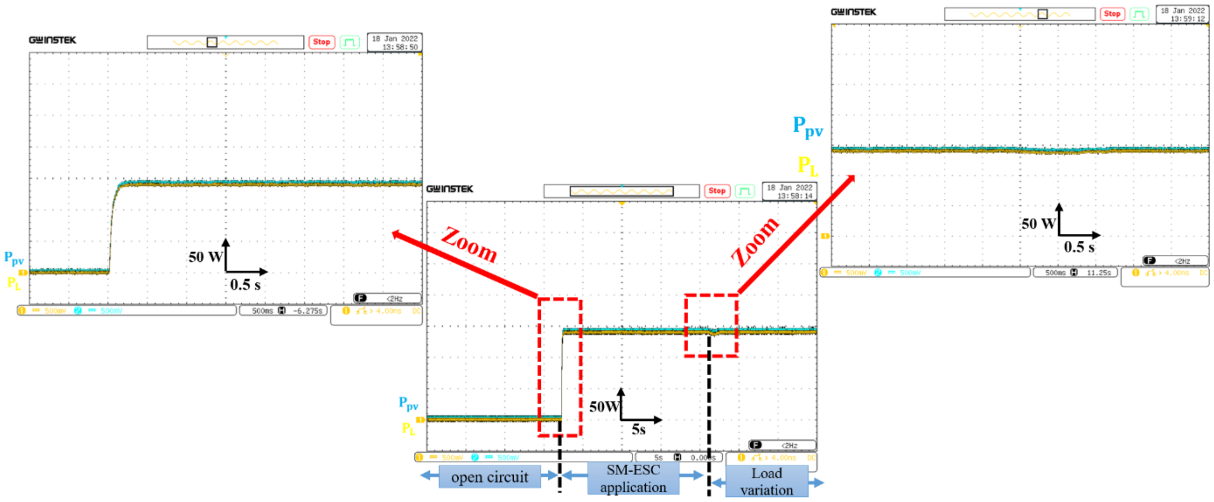

Figure 3.17. PV and load power graphs of SM-ESC method for case 1 and its zoom.

Figure (3.18) illustrates the curves of the PV voltage and current with a zoom-in view of two important points: at start-up and when the load changes. It takes 1s to reach the MPP.

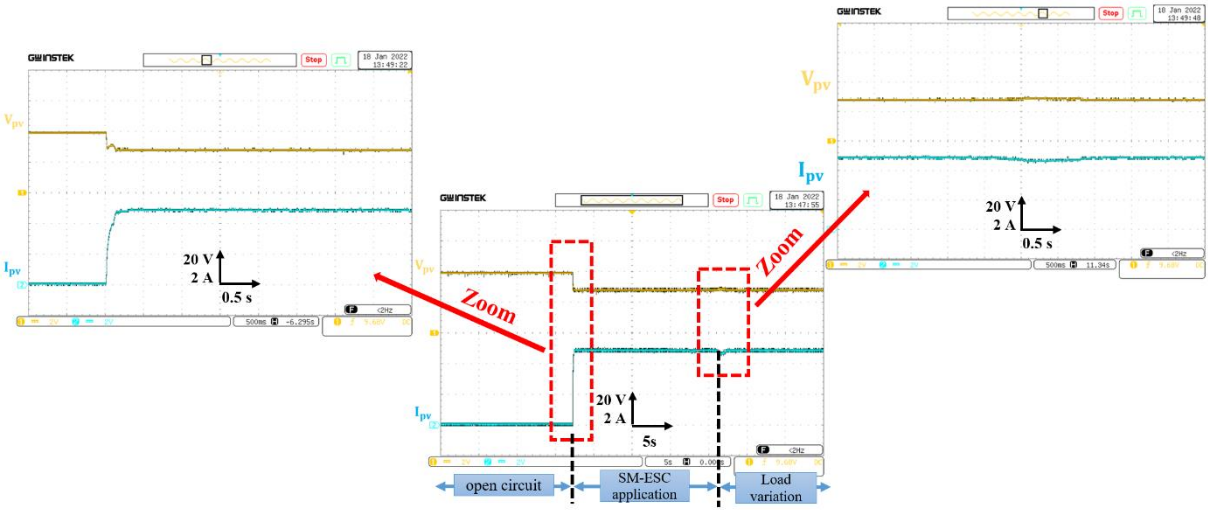

Figure 3.18. PV Voltage and Current graphs of SM-ESC method for case 1 and its zoom.

Figure (3.19) shows the practical responses of the PV and the load power, using the hybrid sliding mode control with the modified ESC. This method takes only 0.15s to reach the maximum power point, while it takes 0.5s when the load change (at 4s).

Figure (3.20) illustrates the curves of the PV voltage and current with a zoom-in view of two important points: at start-up and when the load changes.

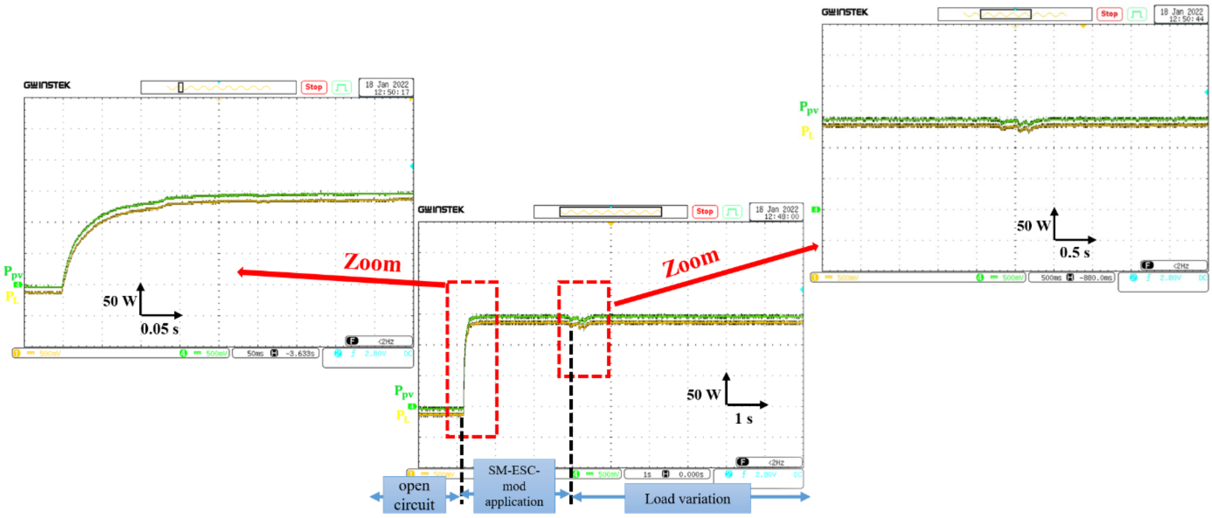

Figure 3.19. PV and load power graphs of SM-ESC-mod method for case 1 and its zoom.

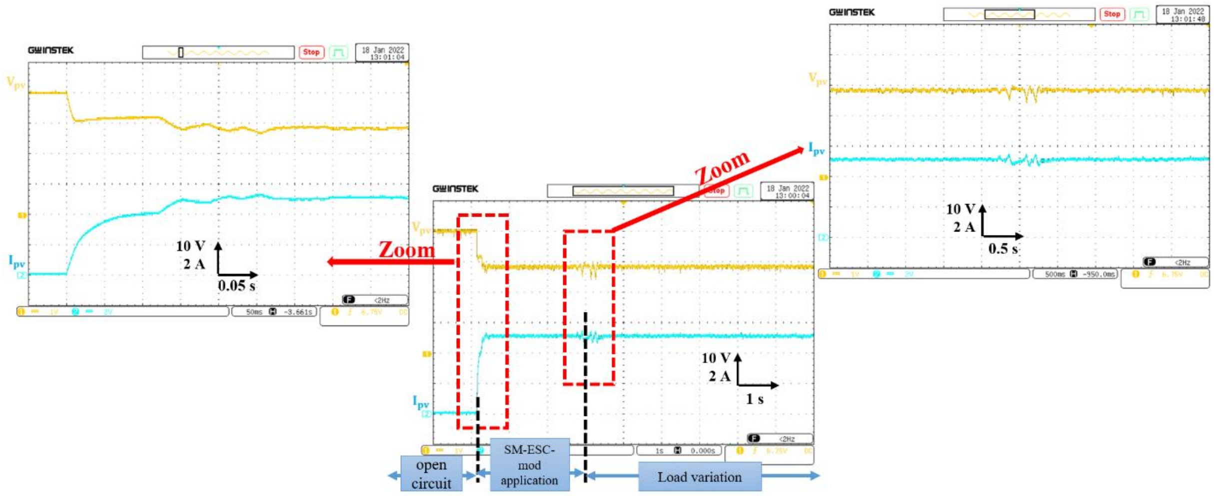

Figure 3.20. PV Voltage and Current graphs of SM-ESC-mod method for case 1 and its zoom.

The next two cases represent the application of the two shaded ratios. In each case, the curve is divided into three steps:

- The first step [0, 15] s: represents the open circuit phase.
- The second step [15, 30] s: represents the application of MPPT in a healthy state.
- The third step [30, 50] s: represents the application of shading percentage.

Case 2: The performance of the five applied strategies are shown respectively in Figures (3.21)-(3.27). From these figures, the following observations can be made:

- After the initialization phase, all methods successfully match the optimum point in the healthy state.
- After the application of 15% partial shading, the performance of the applied strategies differs. It can be seen that the ESC arrives to reject the localization of the operating point at a local knee of the I-V characteristic, and converges after 0.3s to the global Maximum Power Point, where 111 W is extracted (figure 3.13).
- For the SMC strategy, only 58 W is tracked after 0.14s. This power concerns the local optimum point given in the green curve of Figure (3.13) (LMPP). In this situation and since the algorithm does not encompass a random search, while the stabilization control part’s success to converge to the surface equals zero, the process stops. The algorithm fails accordingly to disturb the functioning point.
- All MPPT apply in the following figures track the maximum point at a different time.
- After the application of 15% partial shading, the ESC (figure 4.22) takes 0.3s to reach the MPP, while the hybrid SM-ESC (figure 4.24 and figure 4.25) takes 0.4s. Finally, the hybrid modified ESC with SM (figure 4.26 and figure 4.27) takes only 0.2s.

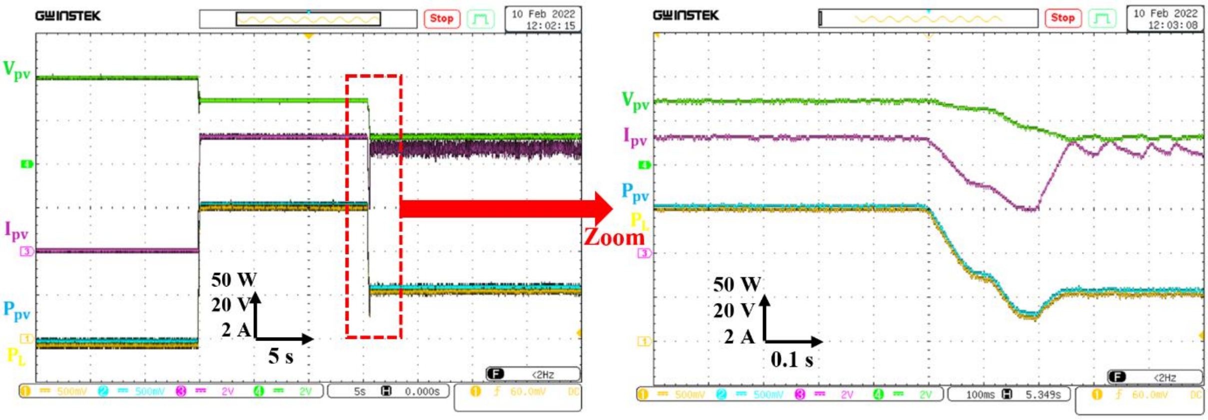

Figure 3.21. Power, Voltage and Current graphs of SMC method for case 2.

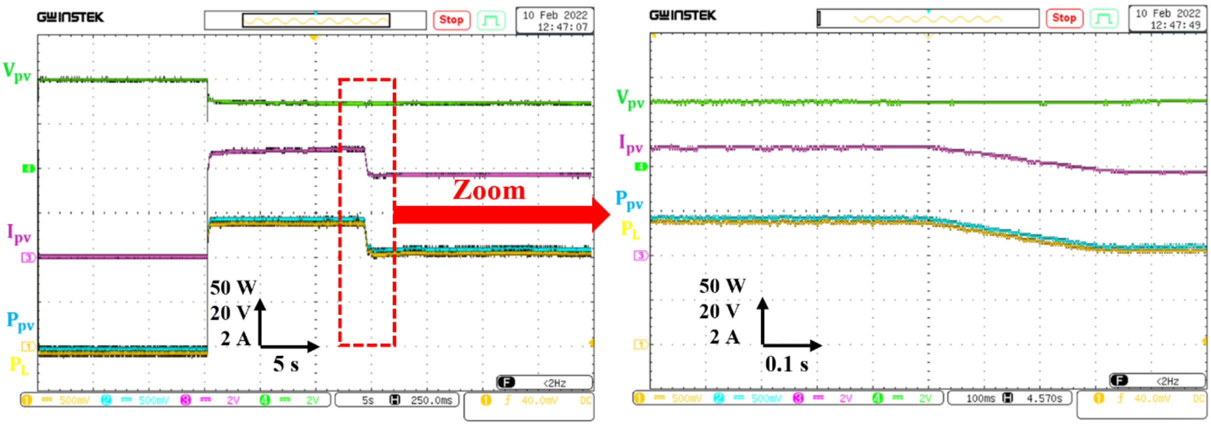

Figure 3.22. Power, Voltage and Current graphs of ESC method for case 2.

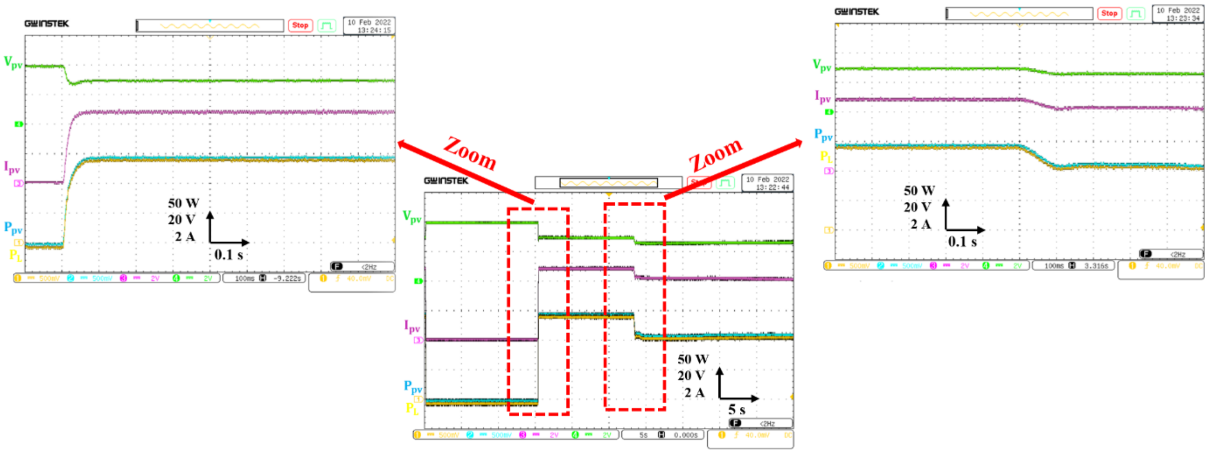

Figure 3.23. Power, Voltage and Current graphs of modified ESC method for case 2 and its zoom.

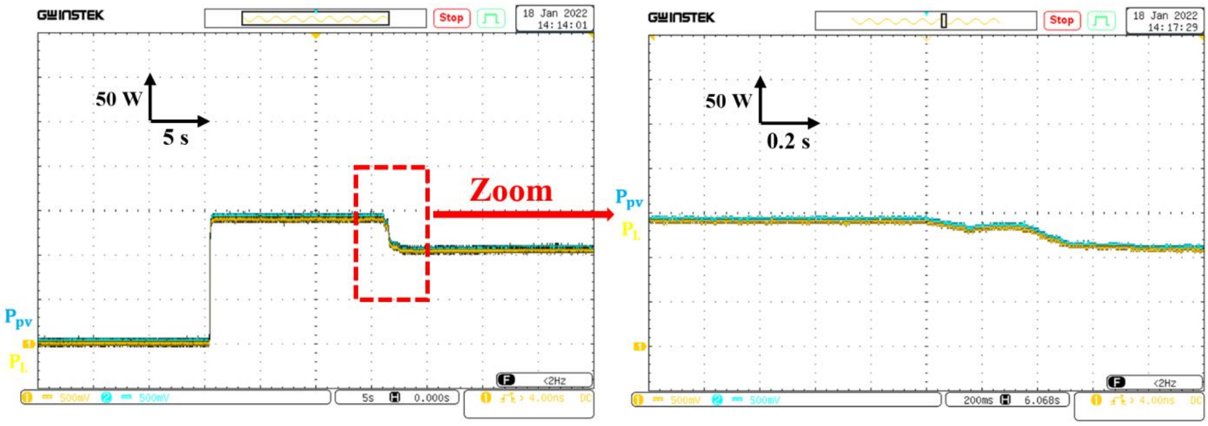

Figure 3.24. PV and load power graphs of SM-ESC method for case 2 and its zoom.

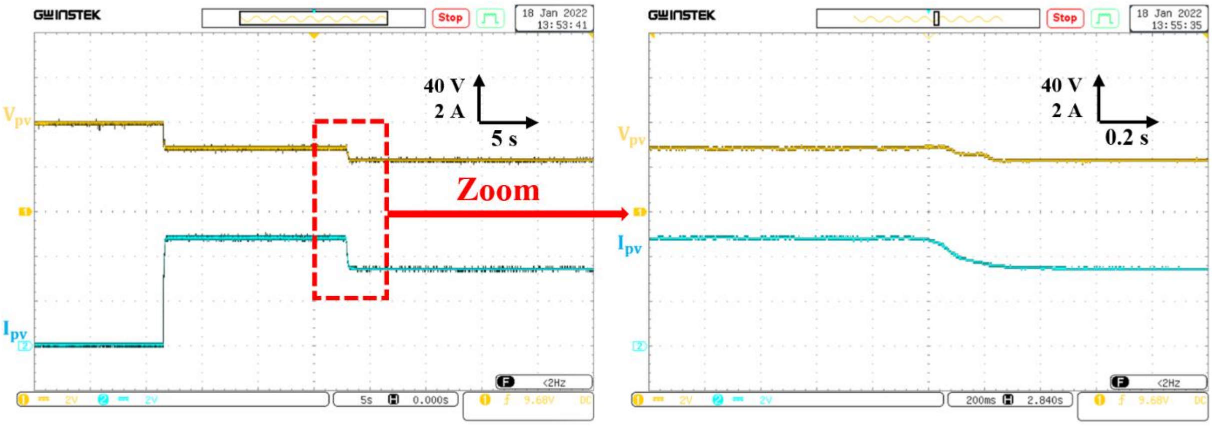

Figure 3.25. PV Voltage and Current graphs of SM-ESC method for case 2 and its zoom.

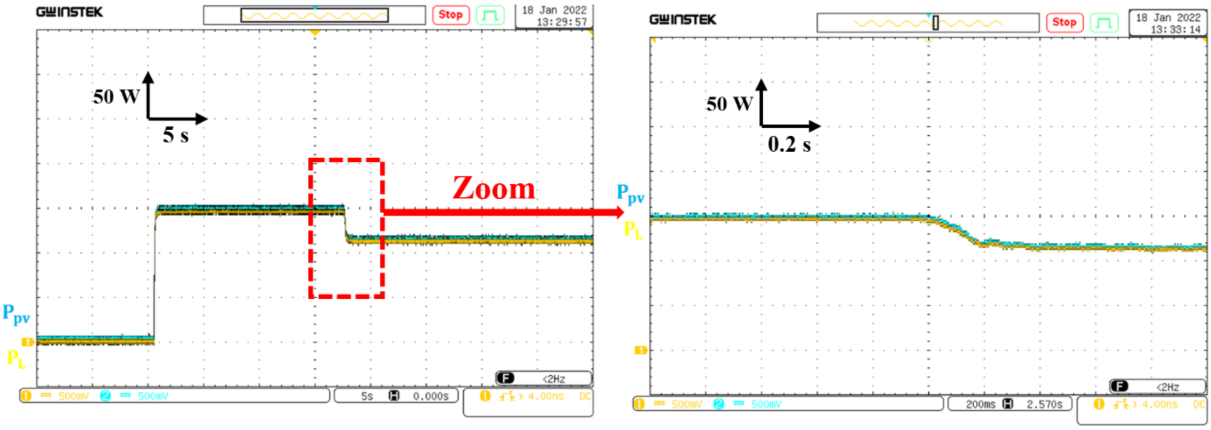

Figure 3.26. PV and load power graphs of SM-ESC-mod method for case 2 and its zoom.

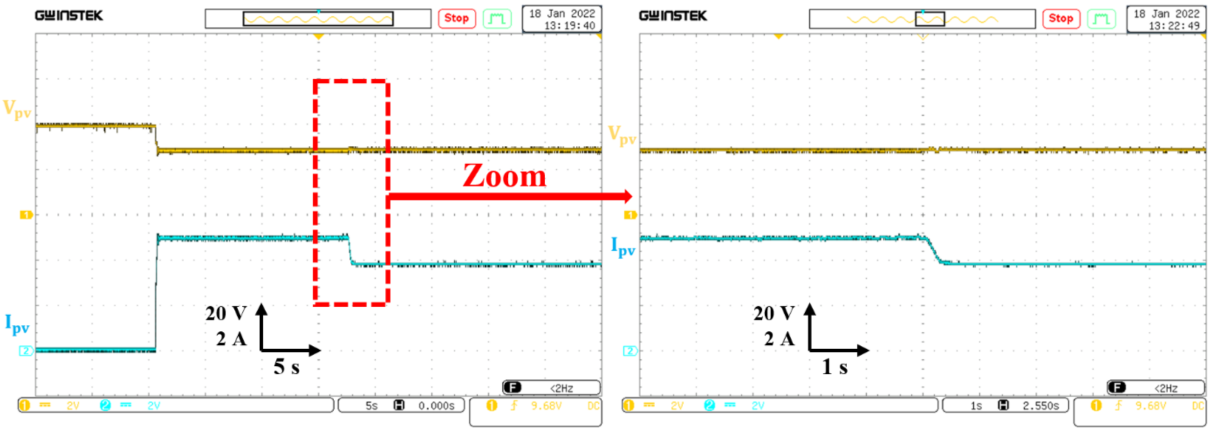

Figure 3.27. PV Voltage and Current graphs of SM-ESC-mod method for case 2 and its zoom.

Case 3: Figures (3.28) and (3.29) show the PV and load power, PV voltage and current of the SMC and ES method, respectively for the third case. It can be seen that the ESC provides better performances, tracking a global maximum power point of about 137 W after 2s, while the operating point stands at a local MPP (LMPP) where only 64 W was extracted after 0.36s. This point concerns in fact the red curve, plotted in Figure (3.13).

After applying 5% partial shading, the modified ESC (figure (3.30)) takes 0.3s to track the MPP, while the hybrid SM-ESC (figure (3.31) and figure (3.32)) takes 0.5s. Finally, the hybrid modified ESC with SM (figure (3.33) and figure (3.34)) takes only 0.25s.

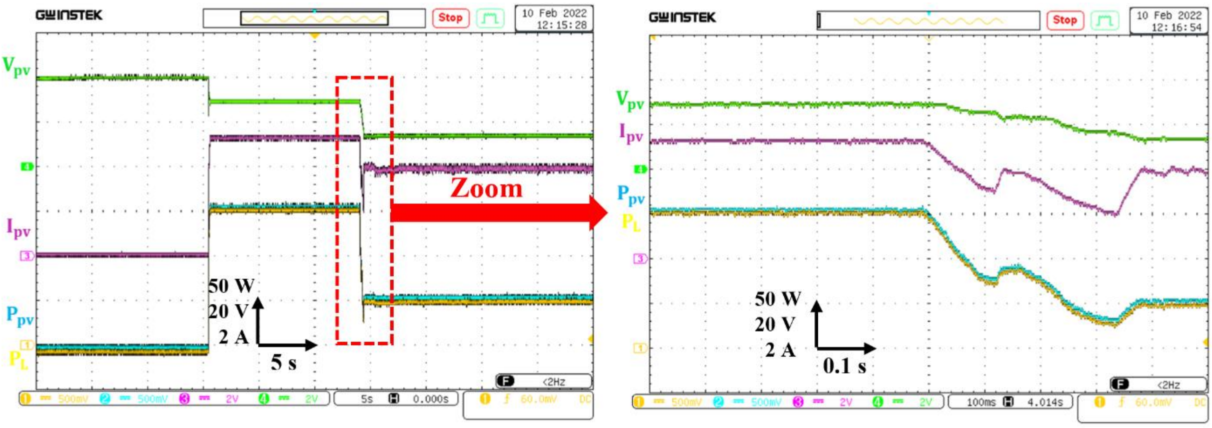

Figure 3.28. Power, Voltage and Current graphs of SMC method for case 3.

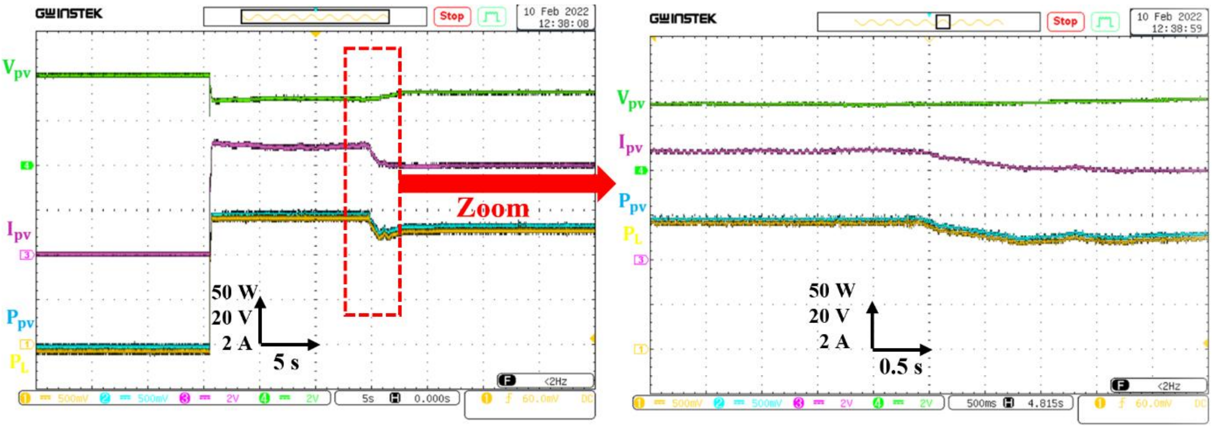

Figure 3.29. Power, Voltage and Current graphs of ESC method for case 3.

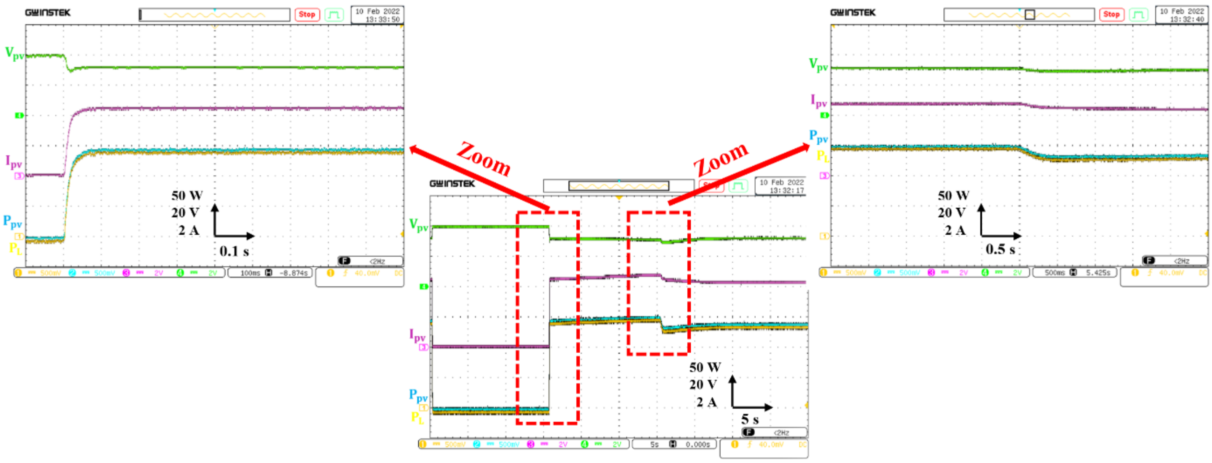

Figure 3.30. Power, Voltage, and Current graphs of the modified ESC method for case 3 and its zoom.

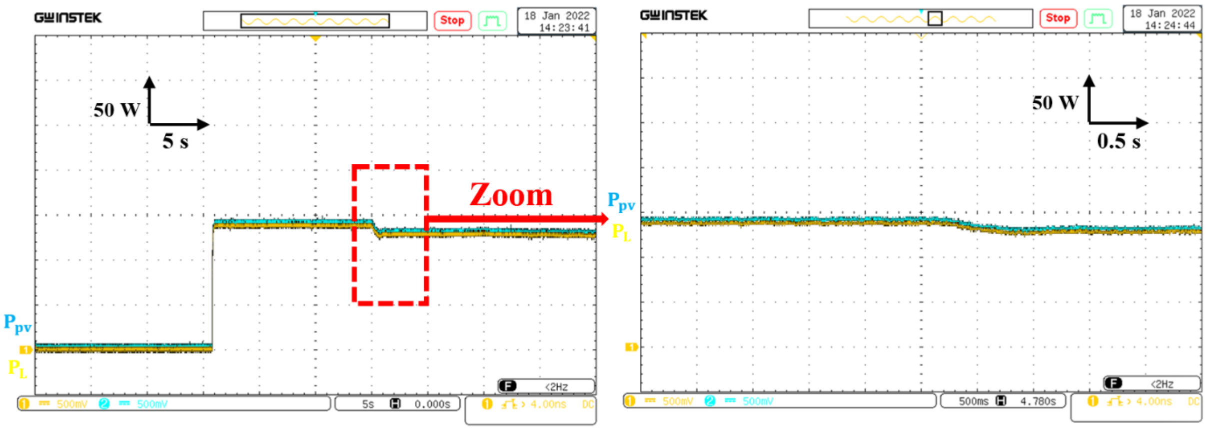

Figure 3.31. PV and load power graphs of SM-ESC method for case 3 and its zoom.

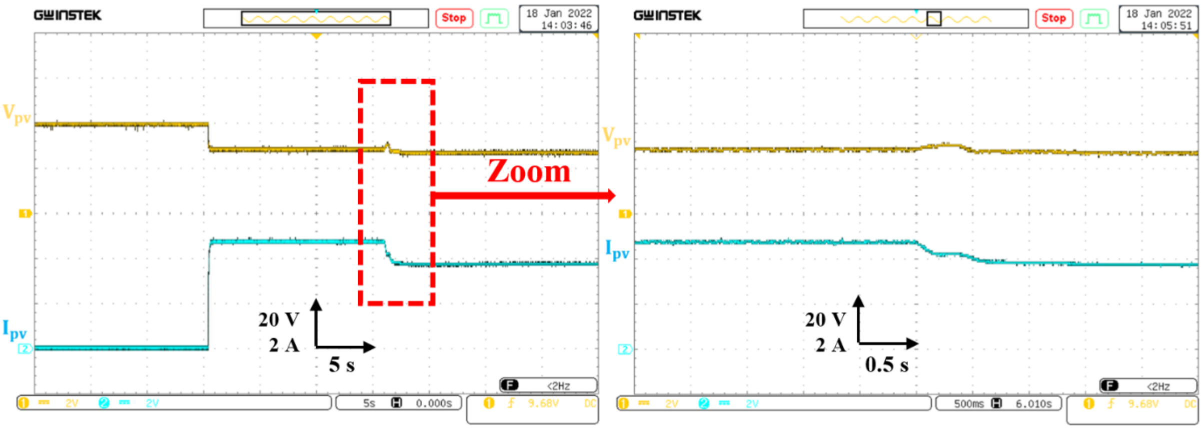

Figure 3.32. PV voltage and current graphs of SM-ESC method for case 3 and its zoom.

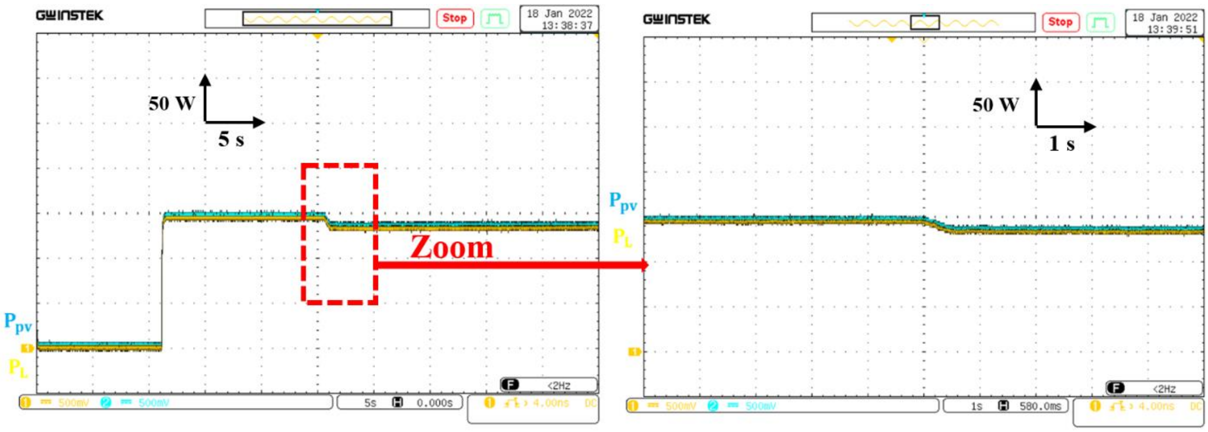

Figure 3.33. PV and load power graphs of SM-ESC-mod method for case 3 and its zoom.

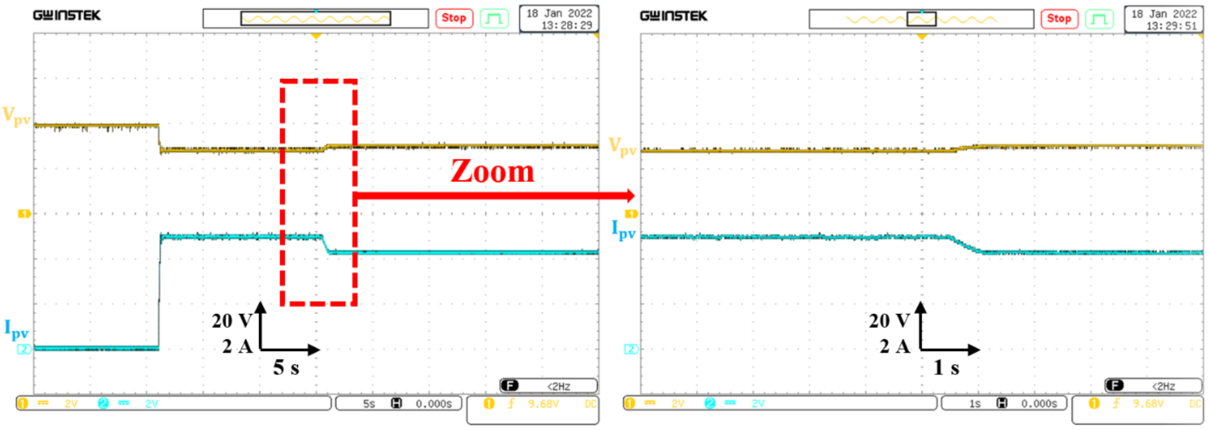

Figure 3.34. PV voltage and current graphs of SM-ESC-mod method for case 3 and its zoom.

An analysis of tracking skills is presented in Table (3.4) as a result of the performance delivered by the proposed algorithms. From this table, it is obvious that the SMC method presents better results than the ESC in terms of the time response to track the optimum point, while the ESC ensures convergence to a global optimum point in the case of partial shading. A modified ESC was implemented, but it takes a longer time compared to the ESC. The hybrid method was developed to create a faster system with the best possible performance.

Table 3.4. Performances comparison between MPPT methods

	method	Convergence time to reach MPP (s)		Operating point
		Closed circuit	Load changing	
Case 1 Healthy	PO	0.2s	-	A lot of chattering
	SMC	Very fast	2s	Around MPP
	ESC	Very fast	4s	MPP
	Modified ESC	Very fast	1.5s	MPP
	SM-ESC	1s	1s	MPP
	SM-ESC-mod	0.15s	0.5s	MPP
Case 2 15% shading	SMC	0.25s		LMPPT
	ESC	0.3s		GMPPT
	Modified ESC	0.15s		GMPPT
	SM-ESC	0.4s		GMPPT
	SM-ESC-mod	0.2s		GMPPT
Case 3 5% shading	SMC	0.36s		LMPPT
	ESC	2s		GMPPT
	Modified ESC	0.3s		GMPPT
	SM-ESC	0.5s		GMPPT
	SM-ESC-mod	0.4s		GMPPT

3.5.Conclusion

In conclusion, partial shading has significant effects on the performance of a photovoltaic (PV) generator. It can lead to a decrease in the output power, efficiency, and reliability of the PV system. Various techniques have been proposed to mitigate these effects such as maximum power point tracking (MPPT) algorithms.

In this chapter, PO, SMC, and classical and improved ESC are chosen for our work. The issues and challenges related to different algorithms, such as tracking accuracy, power oscillations, and efficiency are discussed. In addition, these techniques are implemented with load variation under uniform and non-uniform conditions. Comparative results are summarised in a table. Among these, the MPPT algorithms have shown promising results in improving the performance of partially shaded PV systems. However, the choice of the MPPT algorithm depends on the type and severity of shading, as well as the system's design and requirements.

Chapter 04

Control strategy for a photovoltaic-powered desalination system

4.1.Introduction

This chapter proposes an effective control scheme for a PV desalination system that can operate under uniform, non-uniform irradiance conditions, as well as abrupt irradiance changes. The two main objectives of this scheme are to apply Extremum Seeking Control (ESC) on the PV generator side and Direct Torque Control (DTC) on the machine side, using Lyapunov control to maintain the Vdc constant.

The ESC is applied to the PVG side to overcome power and water quantity losses and improve the system's overall performance. The technical design of the system is based on an existing RO desalination unit, and real climatic data from a local mast is used in the study. Different scenarios, including healthy and shaded conditions based on real climatic data, were tested to obtain results.

The results show that the ESC is effective in extracting global maximum power under shaded conditions in all scenarios, offering up to 685W of extra power compared to conventional controllers. Furthermore, shading conditions can significantly affect freshwater production, with losses estimated at around 82.91% for critical scenarios.

In addition to the ESC, this chapter also proposes a twelve-sector DTC based on an extended switching table as another objective. The findings of this study are significant for industrialists working in this field.

4.2.Study case

The Technical Institute for Agricultural Development in the South (TIADS) is located in Biskra, a city in northeastern Algeria. This institute is equipped with a reverse osmosis desalination system that operates on electrical network mode 1, as shown in Figure (4.1).

The electrical network supplies three pumps. The inlet water goes through a pump that injects it into two filters (a sand filter and an activated carbon filter). After that, the water passes through second stage of filtration to prepare it to go through the high-pressure pump, which injects it into a 4040x4 membrane. This membrane produces fresh water that is then stored in the storage tank. A third pump is used to clean the filters and the membrane with fresh water.

Two tests were conducted: the first involved irrigation with reverse osmosis-treated water, while the second using normal water. The use of RO-treated water had a beneficial effect on the growth and yield of both leguminous and condiment crops, as shown the results of Annex 2, when compared to normal irrigation water. The results demonstrate a significant increase in plant height, leaf count, and crop weight when RO-treated water was used. These findings suggest that utilizing RO-treated water for crop irrigation can be an effective strategy to enhance crop productivity and mitigate the negative effects of soil salinization.

However, most of the farmers suffer either from exposure to power outages or from being remote from the electrical networks. Hence, the idea of this study is to design a GPV system as an alternative to the electrical grid for operating the RO desalination system. This type of system is commonly employed in remote areas where access to fresh water is limited, and traditional grid-based electricity is either unavailable or too expensive to install. The use of such systems provides a sustainable and eco-friendly approach to producing fresh water in regions where traditional sources of fresh water are scarce.

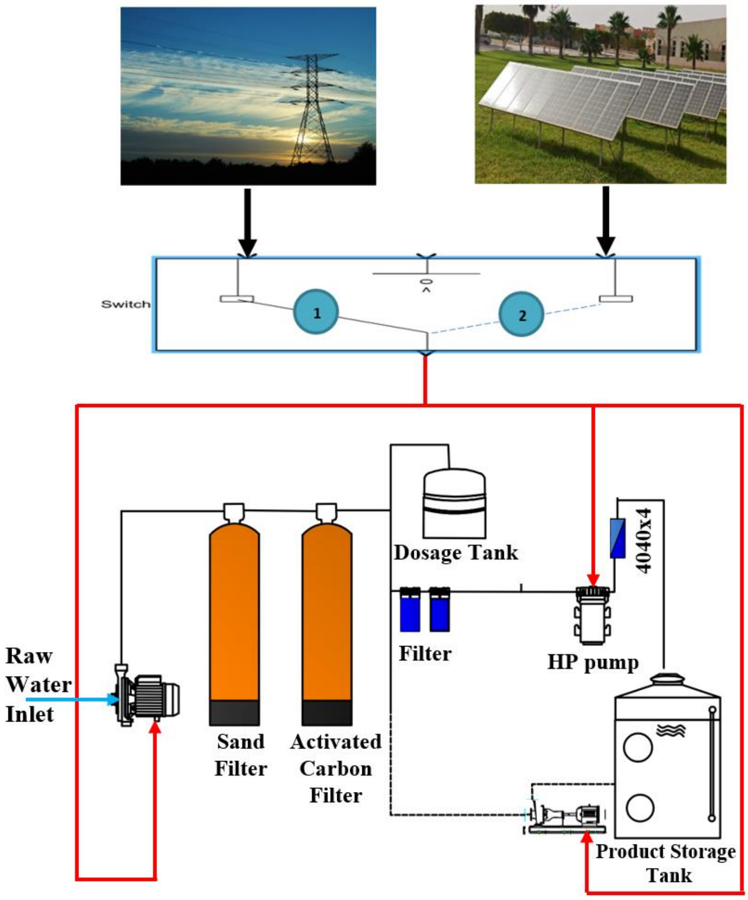

Figure 4.1. Reverse Osmosis Desalination System with Switching Mode for Electrical Network and Photovoltaic Energy Supply.

4.3.Control

In mode 2, as shown in Figure (4.1), a PV generator powers the desalination system. In this configuration, the control part of an RO desalination system powered by PV plays a crucial role in ensuring efficient and reliable operation. The control system monitors various parameters, including water pressure, flow rate, and salinity levels of the water being processed.

Description of the configuration

The control of a PV-RO desalination system involves managing various components to ensure optimal performance and efficient operation. This includes controlling PV panels to maximize energy production, monitoring the RO system to ensure proper water treatment, and managing storage and distribution of fresh water. Effective control of a PV-RO desalination system can improve water supply reliability; reduce energy consumption, and lower operational costs.

This study investigates the performance analysis of a PV-RO desalination system under uniform and non-uniform irradiance conditions. The main objectives are to apply Extremum Seeking Control (ESC) to the PV side to overcome losses in power and water quantity and improve the system's overall performance, and apply Direct Torque Control (DTC) on the motor pump side to achieve fast and precise torque control without the need for a speed or position sensor. Various scenarios, including healthy and shaded conditions, were examined based on real climatic data and parameters (RO desalination’s parameters of TIADS) to obtain results. By studying the system's performance under different conditions, it is possible to improve the system's design and operation for optimal performance.

4.3.1. Control in side of PV generator

As discussed in the previous chapter, the difference between ESC, modified ESC, SM-ESC, and SM-ESC modified lies in the transient regime. Since reverse osmosis desalination systems are not affected by this regime, ESC has been selected as the maximum power point tracking method throughout this chapter.

4.3.2. Control DC bus

To maintain a constant DC bus voltage, irrespective of variations in the $\mathrm{I_{pv}}$ current, a robust controller based on Lyapunov theory was chosen. This technique is often referred to as Lyapunov-type sliding mode control, which guarantees global asymptotic stability of the system. To synthesize the control, the following steps were followed:

The tracking error was defined as follows:

$$\mathrm{e} = \mathrm{V_{dc}} - \mathrm{V_{dc}^{*}} \tag{4.1}$$

The candidate Lyapunov function is defined as positive:

$$\nu = \frac{1}{2}\mathrm{e}^{2} \tag{4.2}$$

Therefore, the gradient of the function ν is derived as follows:

$$\dot{\nu} = \dot{e}e \tag{4.3}$$

To ensure the asymptotic stability of the system, it is necessary to define equation (4.3) as semi-negative. To achieve this, the desired gradient function is selected in the form of decreasing exponential:

$$\dot{\nu} = -ke^2 \tag{4.4}$$

Equating equations (4.3) and (4.4), the closed-loop dynamic error is derived as a first-order equation, with no second number, converging to zero:

$$\dot{e} = -ke \tag{4.5}$$

Using the law of the knot, the equation (4.6) is determined:

$$I_c = I_{dc} - I_{inv} \tag{4.6}$$

Which implies:

$$\dot{V_{dc}} = \frac{I_{dc}}{C} - \frac{I_{inv}}{C} \tag{4.7}$$

The current at the input of the inverter is deduced as follows:

$$I_{inv} = I_{dc} + k.C.e \tag{4.8}$$

4.3.3. Control in side of moto pump

The direct torque control (DTC) for induction machines was first proposed in the mid-1980s by Takahashi [132] and Depenbrock [133]. Compared to vector control, it is less sensitive to parametric variations of the machine [134, 135], and its control algorithm is simpler because it does not require pulse width modulation (PWM), current Controllers, or Park transformations. DTC does not use PI regulation loops, which should improve its dynamic response and eliminate problems related to the saturation of PI regulators. DTC control ensures high-efficiency operation and provides accurate and fast torque dynamics. The principle of DTC is based on the direct application of a control sequence to the switches of the voltage inverter (switching states) placed upstream of the machine [136, 137]. The choice of this sequence is made using a switching table and two hysteresis regulators, which control and regulate the electromagnetic torque and the flux of the machine in a decoupled manner.

Figure (4.2) shows a block diagram of the basic DTC structure. Based on the output of the hysteresis controllers, the inverter switching state can be selected from a predefined look-up table. The torque reference T_e^* is achieved by the Vdc regulator, while the reference of the stator flux magnitude is | φs * |=0.3 Wb. Torque and stator flux estimations are based on the IM model, and torque and flux errors are controlled using the hysteresis controllers. The output of these controllers is the input of the switching selection table of the voltage vector.

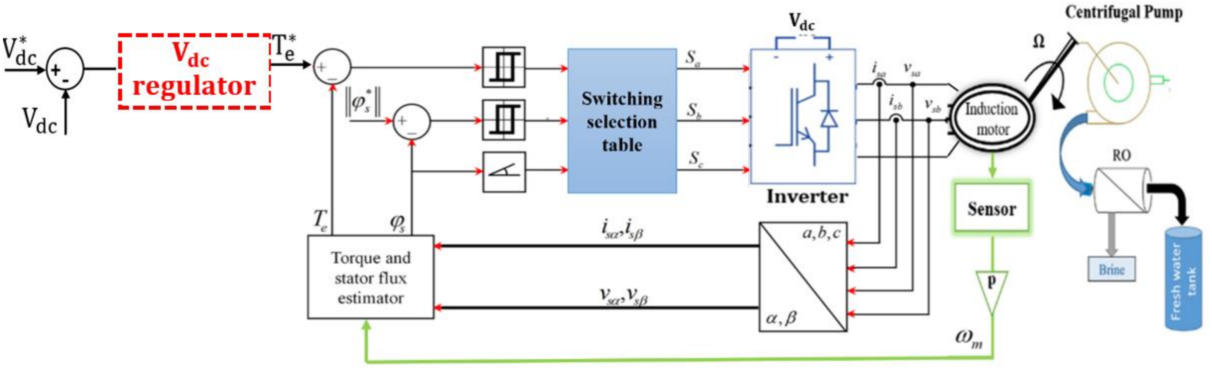

Figure 4.2. Bloc diagram of the DTC technique.

4.3.3.1.Induction Motor Model

The vector expressions of the IM in the stator reference frame are defined in the system of equations (I) with the rotor voltage set to zero $\overline{V_r} = 0$, because the cage IM has a short-circuited rotor.

$$
(\mathrm{I}) \begin{cases} \overline{V_s} = R_s\overline{I_s} + \dfrac{d\overline{\varphi_s}}{dt} & (4.9) \\ \overline{V_r} = 0 = R_r\overline{I_r} + \dfrac{d\overline{\varphi_r}}{dt} - j\omega\overline{\varphi_r} & (4.10) \\ \overline{\varphi_s} = L_s\overline{I_s} + L_m\overline{I_r} & (4.11) \\ \overline{\varphi_r} = L_r\overline{I_r} + L_m\overline{I_s} & (4.12) \end{cases}
$$

The rotor current can be written using the flux expressions (4.11) and(4.12) as follows:

$$
\overline{I_r} = \frac{1}{\sigma}\left[\frac{1}{L_r}\overline{\varphi_r} - \frac{L_m}{L_r L_s}\overline{\varphi_s}\right] \tag{4.13}
$$

Where σ is the dispersion coefficient defined by:

$$
\sigma = 1 - \frac{{L_m}^2}{L_r L_s} \tag{4.14}
$$

By substituting the expression (4.13) into equations (4.9) and (4.10), the system of equation (I) becomes:

$$(\mathrm{II})\begin{cases}\overline{V_s} = R_s\overline{I_s} + \frac{d\overline{\varphi_s}}{dt} & (4.15)\\ \frac{d\overline{\varphi_r}}{dt} + \left(\frac{1}{\sigma\, t_r} - j\,\omega\right)\overline{\varphi_r} = \frac{L_m}{\sigma\, t_r L_s}\overline{\varphi_s} & (4.16)\end{cases}$$

The system of equation (II) shows that:

- It is possible to control vector $\overline{\varphi_s}$ from the stator voltage ($\overline{V_s}$), neglecting the drop $R_s\overline{I_s}$
- The flux $\overline{\varphi_r}$ follows the variations of $\overline{\varphi_s}$ with a time constant ($\sigma\, t_r$)

4.3.3.2.Torque and stator flux estimations

The stator flux and electromagnetic torque are estimated from the stator voltage and current vectors. The expression of the stator flux is written as follows:

$$\overline{\varphi_s}(t) = \int_0^t (\overline{V_s} - R_s\overline{I_s})\, dt \tag{4.17}$$

In the reference (α, β), the flux $\overline{\varphi_s}$ and the current $\overline{I_s}$ are written as follows:

$$\begin{cases}\overline{\varphi_s} = \varphi_{s\alpha} + j\,\varphi_{s\beta}\\ \overline{I_s} = \ \ I_{s\alpha} + j\, I_{s\beta}\end{cases} \tag{4.18}$$

According to the Concordia transformation, we have:

$$\begin{cases} I_{s\alpha} = \sqrt{\frac{2}{3}}\, I_{sa}\\ I_{s\beta} = \frac{1}{\sqrt{2}}\,(I_{sb} - I_{sc})\end{cases} \tag{4.19}$$

$$\begin{cases} V_{s\alpha} = \sqrt{\frac{2}{3}}\, V_{dc}\left[S_a - \frac{1}{2}(S_b + S_c)\right]\\ V_{s\beta} = \frac{1}{\sqrt{2}}\, V_{dc}\,(S_b - S_c)\end{cases} \tag{4.20}$$

The stator flux module is written as:

$$|\overline{\varphi_s}| = \sqrt{\varphi_{s\alpha}^2 + \varphi_{s\beta}^2} \tag{4.21}$$

The angle θ_s of equation (4.22) determines the position of vector $\overline{\varphi_s}$

$$\theta_s = \mathrm{arctg}\left(\frac{\varphi_{s\beta}}{\varphi_{s\alpha}}\right) \tag{4.22}$$

The torque is estimate by:

$$T_e = p\,(\varphi_{s\alpha}\, I_{s\beta} - \varphi_{s\beta}\, I_{s\alpha}) \tag{4.23}$$

4.3.3.3.Switching selection table

Two states per sector in classical DTC provide a torque ambiguity. As a result, they are never used. If the stator flux locus is divided into twelve sectors rather of six, it appears that all six active states will be employed per sector. Figure (4.3) illustrates this unique stator flux location.

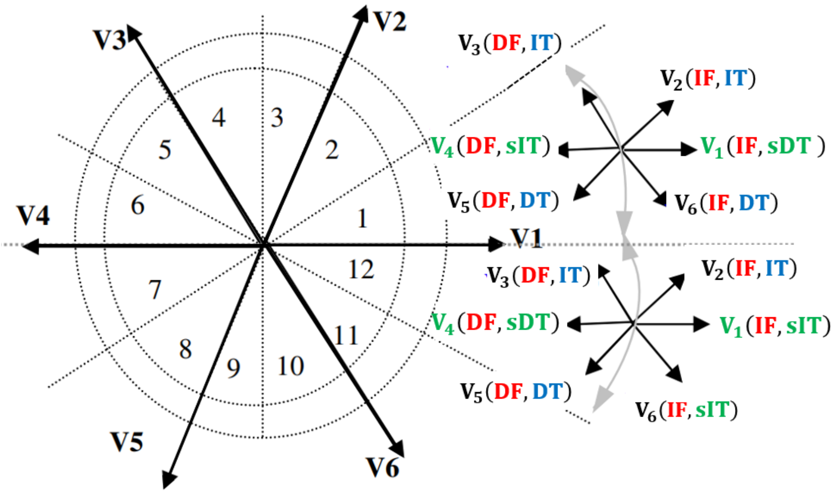

Figure 4.3. Twelve sectors DTC and its voltage vectors. Red IF/DF: Flux large increase/decrease. Blue IT/DT: Torque large increase/decrease. Green sIT/sDT: Torque small increase/decrease.

To analyse the system, it is necessary to define small and large variations. It is obvious that V_1 will produce a large increase in flux and a small increase in torque in sector S_{12}. However, it will also produce a large increase in flux and a small decrease in torque in sector S_1. Table (4.1) shows the cases where the six voltage vectors can be used in the S_1, and S_{12} sectors.

Table (4.1): Effect of voltage vectors for DTC 12 sectors

		Increase	**Decrease**
S_{12}	**Stator flux**	**V_1**, V_2, V_6	V_3, **V_4** , V_5
	Torque	**V_1**, V_2, V_3	**V_4**, V_5 , V_6
S_1	**Stator flux**	**V_1**, V_2, V_6	V_3, **V_4** , V_5
	Torque	V_2, V_3, **V_4**	V_5, V_6 , **V_1**

By using a 4-level hysteresis comparator for torque control (figure (4.4)) and a 2-level hysteresis comparator for the flux, the system can better exploit the available voltages to achieve the desired torque. This approach enables fine-grained control over the motor's torque output, which can help minimize energy consumption and maximize efficiency.

This makes it possible to define the small and large variations of the torque and flux generated by these same voltage vectors according to their phase shift with respect to the limits of the zones [138].

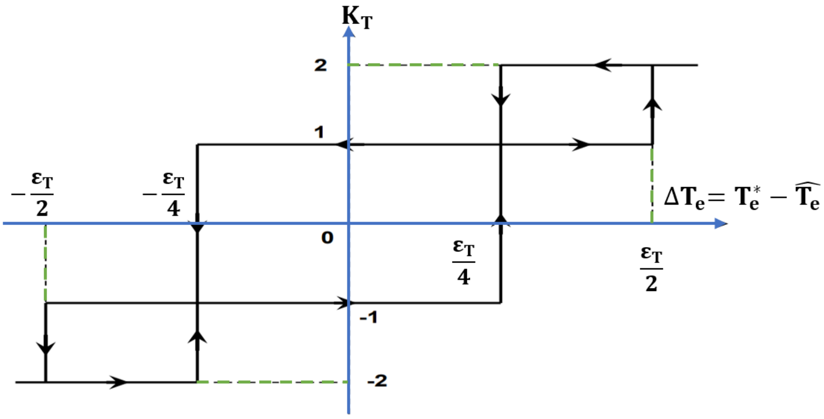

Figure 4.4. Hysteresis comparator used for torque control.

The following algorithm models the comparator:

- $\Delta T_e > +\frac{\varepsilon_T}{2}$ if $K_T = 2$
- $+\frac{\varepsilon_T}{4} < \Delta T_e < +\frac{\varepsilon_T}{2}$ if $K_T = 1$
- $-\frac{\varepsilon_T}{2} < \Delta T_e < -\frac{\varepsilon_T}{4}$ if $K_T = -1$
- $\Delta T_e < -\frac{\varepsilon_T}{2}$ if $K_T = -2$

The voltage vector selection table for the twelve sectors, numbered 1 through 12, is presented in Table (4.2). Each sector corresponds to a specific region of the motor's rotation, and the table lists the available voltage vectors for each sector. This selection table serves as a comprehensive guide for selecting voltage vectors to apply to the motor, allowing the control algorithm to accurately adjust the motor's speed and direction.

Table (4.2): Switching table for 12_ DTC

		Sector S_i											
$K_\emptyset$	K_T	S_1	S_2	S_3	S_4	S_5	S_6	S_7	S_8	S_9	S_{10}	S_{11}	S_{12}
1	2	V_2	V_3	V_3	V_4	V_4	V_5	V_5	V_6	V_6	V_1	V_1	V_2
	1	V_2	V_2	V_3	V_3	V_4	V_4	V_5	V_5	V_6	V_6	V_1	V_1
	-1	V_1	V_1	V_2	V_2	V_3	V_3	V_4	V_4	V_5	V_5	V_6	V_6
	-2	V_6	V_1	V_1	V_2	V_2	V_3	V_3	V_4	V_4	V_5	V_5	V_6
0	2	V_3	V_4	V_4	V_5	V_5	V_6	V_6	V_1	V_1	V_2	V_2	V_3
	1	V_4	V_4	V_5	V_5	V_6	V_6	V_1	V_1	V_2	V_2	V_3	V_3
	-1	V_7	V_5	V_0	V_6	V_7	V_1	V_0	V_2	V_7	V_3	V_0	V_4
	-2	V_5	V_6	V_6	V_1	V_1	V_2	V_2	V_3	V_3	V_4	V_4	V_5

4.3.4. Calculate water quantity

Power losses in PV (photovoltaic) generator systems refer to the reduction in electrical energy that occurs between the point of power generation by the solar panels and the point of delivery to the end user. These losses can occur due to various factors, such as shading of solar panels, temperature variations, and losses due to the inverter conversion process. Shading, in particular, can significantly reduce the overall efficiency of a PV system, and the power losses caused by shading are defined by the difference between the maximum power point (MPP) of the shaded and unshaded panels (equation (4.24)). These power losses result in a decrease in the amount of power available to the end user and can impact the financial viability of the PV system over time.

$$\text{Power losses } (\%) = \frac{[\mathrm{P_{op}(global)} - \mathrm{P_{op}(local)}] \times 100}{\mathrm{P_{op}(global)}} \tag{4.24}$$

Shading also can have a significant impact on the amount of water that can be desalinated by the RO desalination system. When a solar panel is shaded, its energy output decreases, and this reduction in power output can affect the performance of the entire system. This can result in lower water production rates and an increase in the water quantity losses due to a lower production of the electricity needed to power the RO process. Equation (4.25) is defined to estimate the water quantity losses (WQL):

$$\text{WQL } (\%) = \frac{[PWQ(global) - PWQ(local)] \times 100}{PWQ(global)} \tag{4.25}$$

Where:

PWQ is the permeate water quantity obtained by integration of the curve of the permeate flow rate according to the following equation:

$$\mathrm{PWQ} = \int_{SR}^{SS} Q_p \, \mathrm{dt} \tag{4.26}$$

The Feed Water Quantity (FWQ) is calculated as follows:

$$\mathrm{FWQ} = \int_{SR}^{SS} Q_f \, \mathrm{dt} \tag{4.27}$$

Where:

SS is Sunset and SR is Sunrise

4.4.Characteristic of the RO desalination system

There are several characteristics that define an RO desalination system, including:

Efficiency: The efficiency of an RO desalination system refers to its ability to convert seawater or brackish water into fresh water. This is usually measured in terms of the recovery rate, which is the amount of freshwater produced compared to the amount of seawater or brackish water fed into the system. High recovery rates are desirable, as they reduce the amount of water wasted and increase the efficiency of the system.

Capacity: The capacity of an RO desalination system refers to the amount of water it can produce in a given time. This is usually measured in terms of cubic meters per day (m3/day). The capacity of an RO system depends on several factors, including the size of the membrane, the number of membranes, and the flow rate of the water.

Quality: The quality of the water produced by an RO desalination system refers to its purity and the level of impurities it contains. The quality of the water depends on the type and quality of the membranes used, as well as the pre-treatment and post-treatment processes.

Energy consumption: The energy consumption of an RO desalination system refers to the amount of energy required to operate the system. This includes the energy required to pump the water through the membranes, as well as the energy required for pre-treatment and post-treatment processes. The energy consumption of an RO system can vary depending on several factors, including the type of membranes used, the recovery rate, and the size of the system.

4.4.1. Characteristic of the field generator

This part’s test is designed to determine the PV generator characteristic and the maximum power generated under different irradiances in the healthy case. Simulations using MATLAB/Simulink® environment are conducted to test the proposed strategies. The model created in Simulink takes into account the full control system, including the different elements models of the PV desalination system. The PV generator consists of fifteen 162 W PV modules (Annex 1) connected in a 5 (series) × 3 (parallel), with the current-voltage and power-voltage characteristics of the PV array.

Table (4.3) presents the optimum power, voltage, and current of the PV generator for different irradiance levels ranging from 300 to 1000 W/m². The measured power ranges between 2430 W and 645.1 W, while the voltage and current range between 187.4V-159.4V and 13.62A-4.05A, respectively.

Table (4.3) Healthy case with different irradiances

$E(W/m^2)$	1000	900	800	700	600	500	400	300
P_{op} (W)	2430	2165	1903	1644	1387	1135	887	645,1
V_{op} (V)	178,4	177,6	175,2	172,3	171,1	167,7	163,9	159,4
I_{op} (A)	13,62	12,19	10,86	9,54	8,10	6,77	5,41	4,05

4.4.2. Sudden Irradiance Change

The ESC was used as an MPPT to maintain the previous PV generator at the optimal point. This generator powers a reverse osmosis desalination system with the system parameters mentioned in Annex 1. The PV-RO desalination system was subjected to an irradiance profile with various sudden changes. The irradiance was set at 700 W/m² initially and then increased suddenly to 800W/m² after 3.5 seconds. It was again increased suddenly to 900 W/m² after 7 seconds. At 10.5 seconds, the irradiance increased to 1000W/ m² and then abruptly decreased to 700 W/m², while the temperature remained constant at 25 °C. The irradiance profile used in this study is presented in figure (4.5).

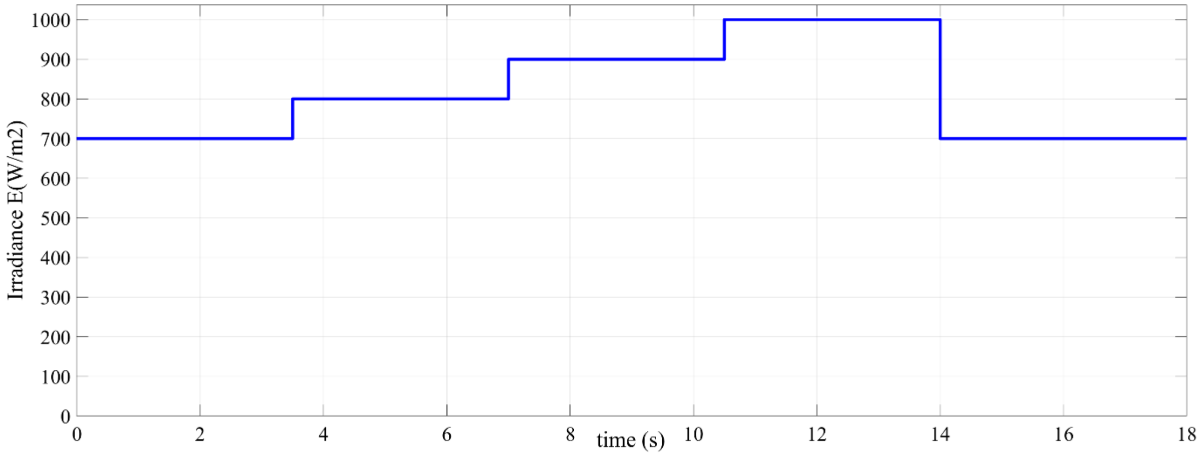

Figure 4.5. The considered irradiance profile.

Figure (4.6) illustrates the power generated by the PV generator as it evolves with the irradiance profile proposed in the previous figure, at a constant temperature of T=25°C. The graph demonstrates that the power output increases as the irradiance level rises from 700W/m² to 1000W/m² and decreases as the irradiance level drops from 1000W/m² to 700W/m².

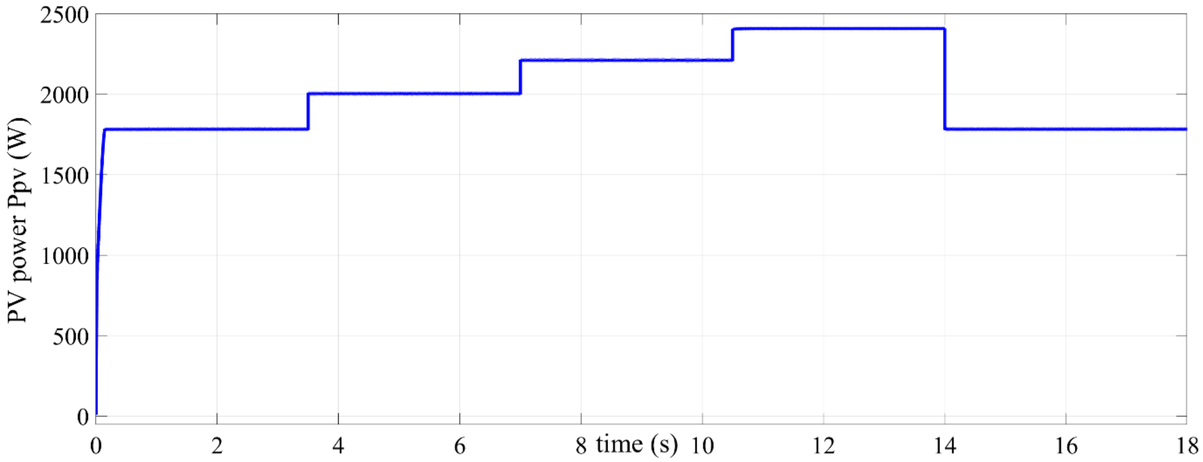

Figure 4.6. Power generated by the PV generator.

Figures (4.7) and (4.8) depict the voltage and current patterns at the input of the PV array matching stage, respectively. The figures demonstrate that the operating points converge rapidly to their optimal points for each irradiance value, without any overshooting. This confirms the effectiveness of the selected MPPT control.

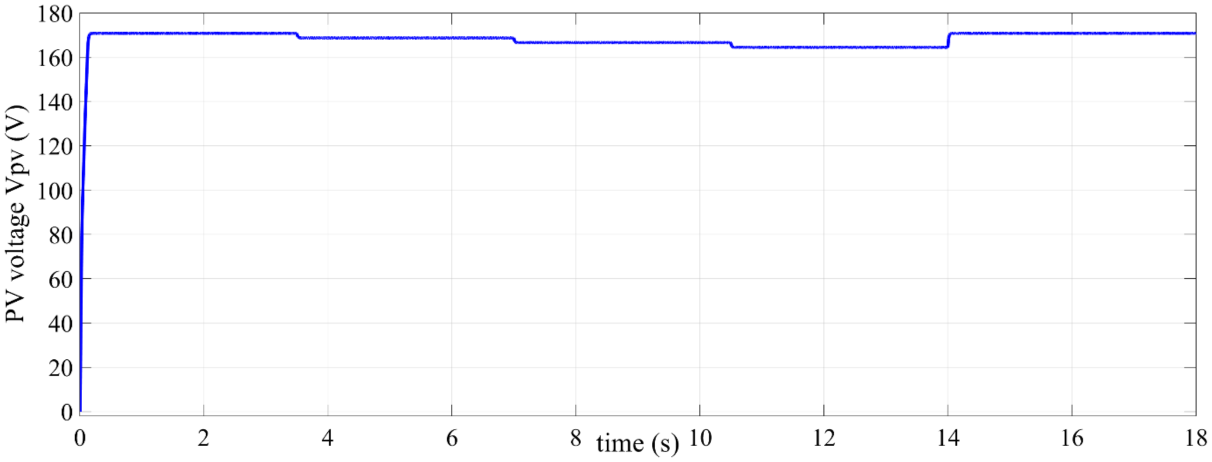

Figure 4.7. The voltage generated by the PV generator.

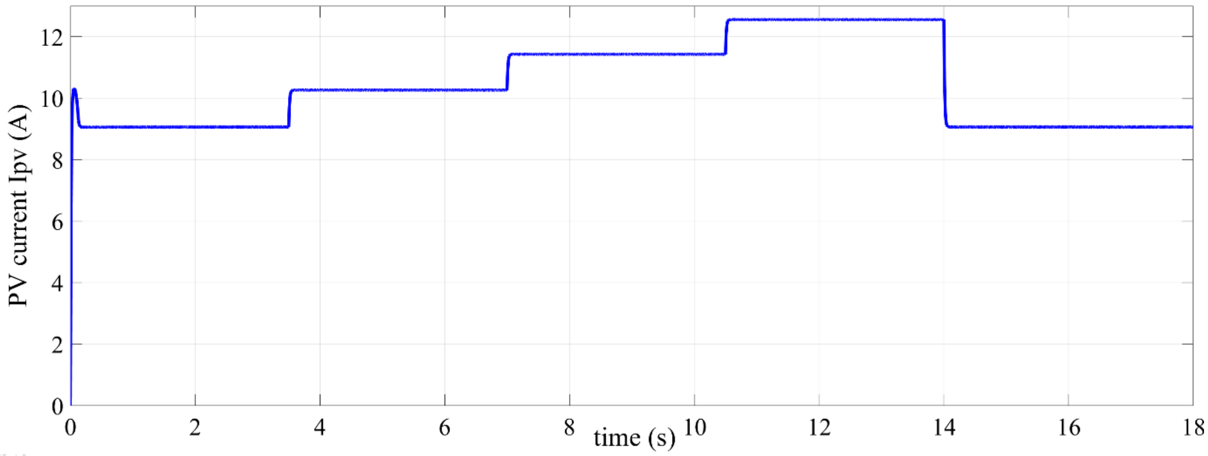

Figure 4.8. The current generated by the PV generator.

Figure (4.9) displays the excellent tracking of the DC bus voltage with its reference value. The graph reveals that the voltage is maintained constant at 300V, despite variations in torque and speed. This observation confirms the effectiveness of the regulator used.

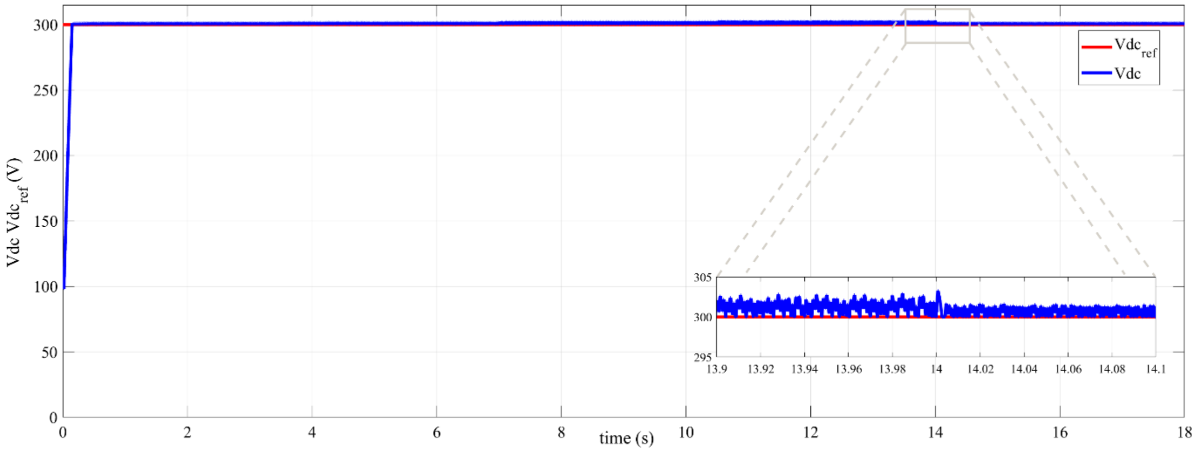

Figure 4.9. The current generated by the PV generator.

When the PV generator experiences sudden changes in irradiance, this can affect the amount of electrical power being supplied to the induction machine, which in turn affects its electromagnetic torque. This can result in changes to the speed and/or direction of the machine's rotation, which can then influence the resistance torque. Figure (4.10) represents the simulation results for the electromagnetic and resistance torque. It is clear that the two torques follow each other with a small overshoot due to friction.

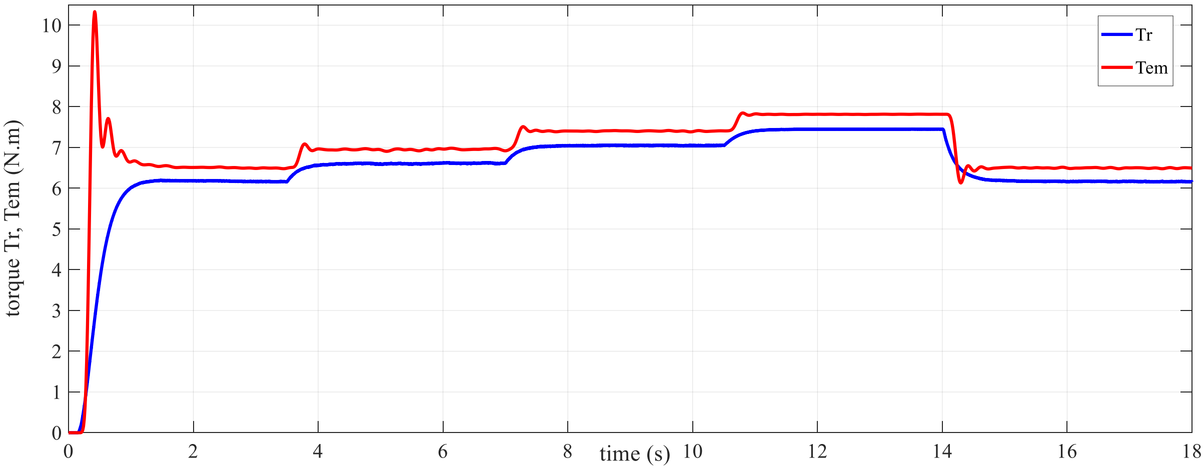

Figure 4.10. Curves of electromagnetic and load torques.

Figure (4.11) represents the stator flux amplitude with its reference estimated value of 0.3 wb. It is found that the stator flux exhibits a smooth response with lesser ripple, resulting in a good current waveforms as presented in Figure (4.11).

Overall, the sinusoidal current waveform and stator flux provide important information about the behavior of the system and can be used to optimize its performance under varying irradiance conditions. By analyzing these signals, adjustments can be made to the system to improve its efficiency, reduce its losses, and ensure its reliable operation.

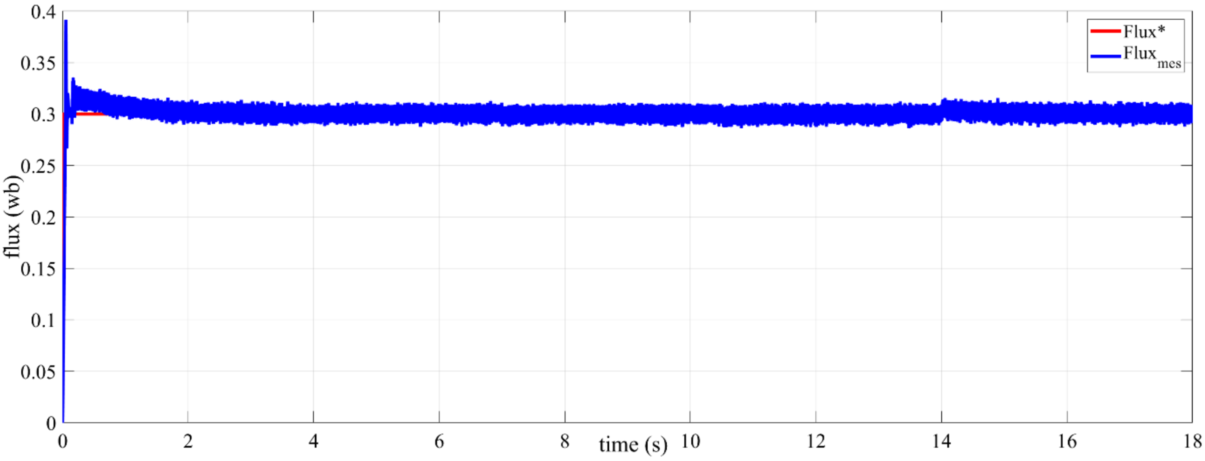

Figure 4.11. Stator flux amplitude with its reference.

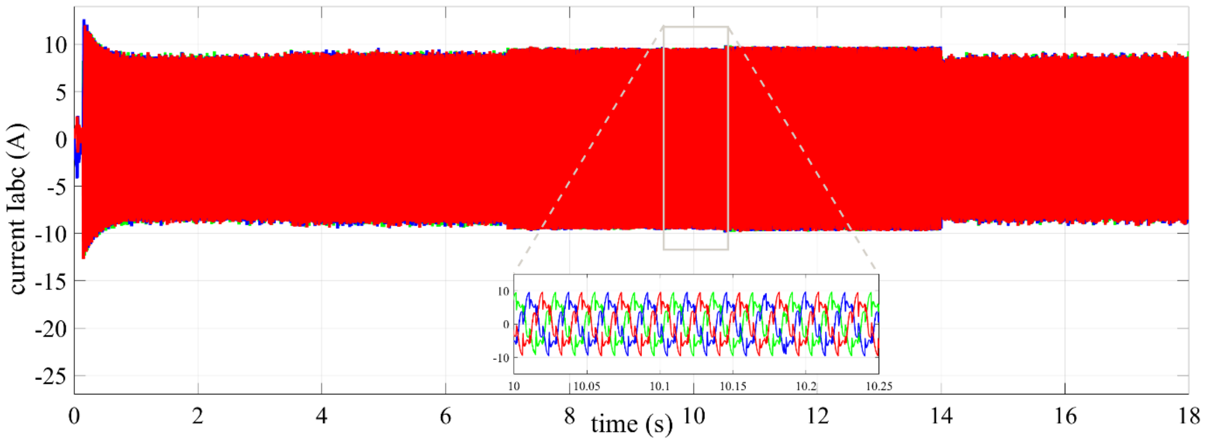

Figure 4.12. Stator currents with zoom waveforms under sudden irradiance variations.

The machine speed is determined by the level of irradiation, where an increase in irradiance results in an increase in speed. At 1000 W/m^2, the speed reaches its maximum value of 130 rad/s. Figure (4.13) displays the speed variation in response to the previously presented irradiance profile.

The speed of the induction machine in a PV-RO desalination system plays an important role in determining the system's performance. Optimal speed control can ensure that the system operates at peak efficiency, while suboptimal speed control can lead to reduced performance and increased energy consumption.

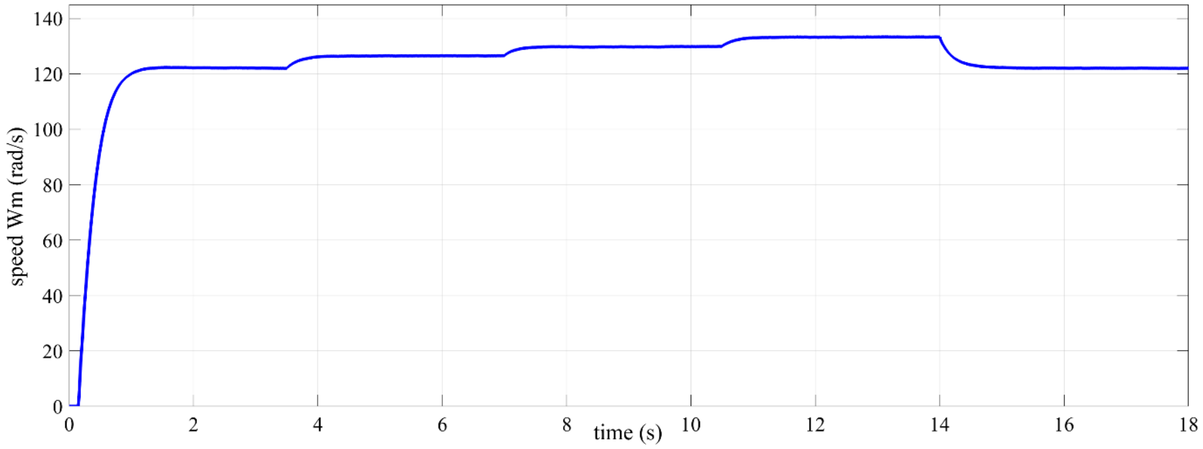

Figure 4.13. The speed variance according to the irradiance profile.

On another side, figure (4.14) presents the hydraulic quantities under sudden variation irradiance. From top to bottom, the curves shown in this figure are: (A) Feed pressure, (B) feed and permeate flow rate, and (C) recovery.

It is clear that the feed flow rate varies with irradiance, ranging from 33 l/min at 1000 W/m² to 27,5 l/min at 700 W/m² due to an increase in the feed pressure. Additionally, the recovery decreased to 25% at 1000 W/m².

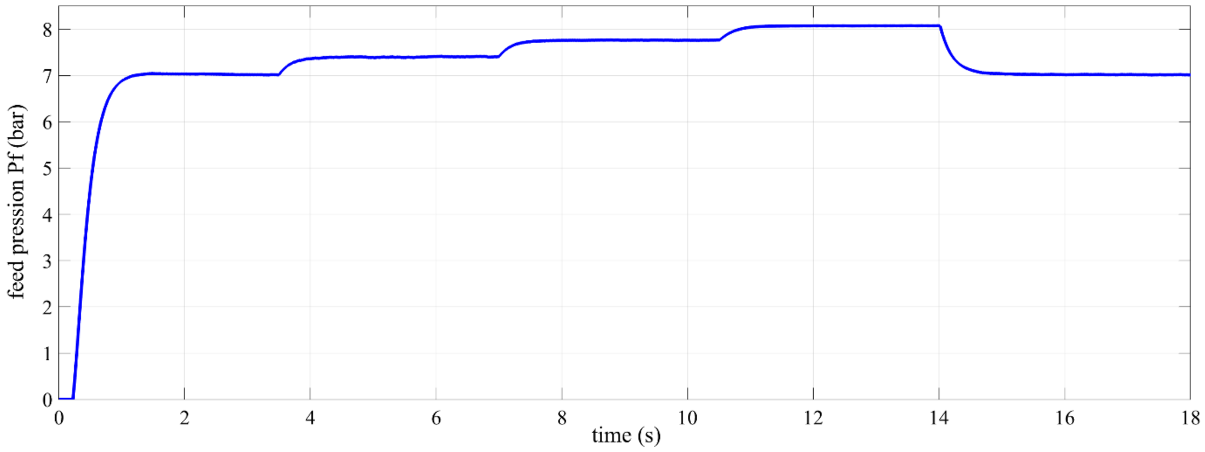

(A)

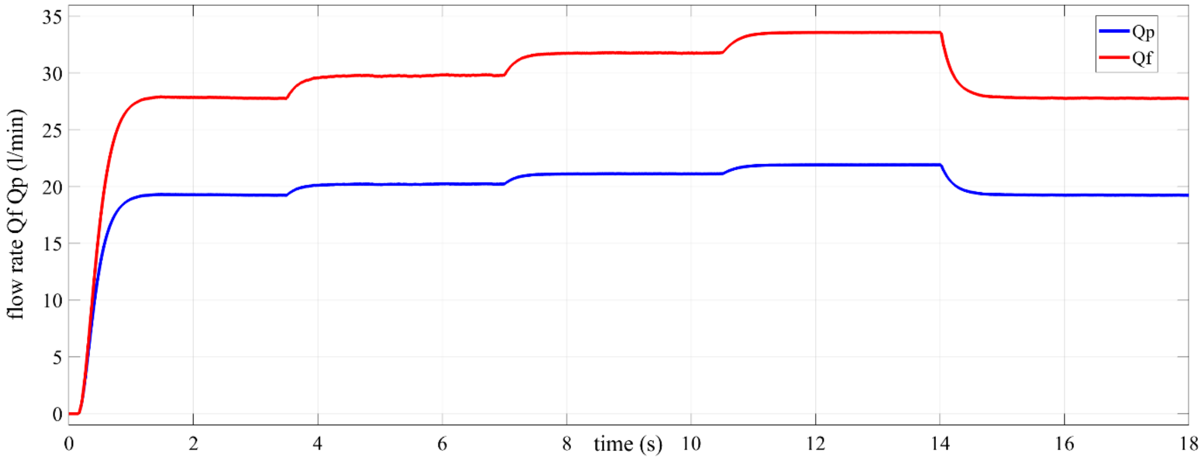

(B)

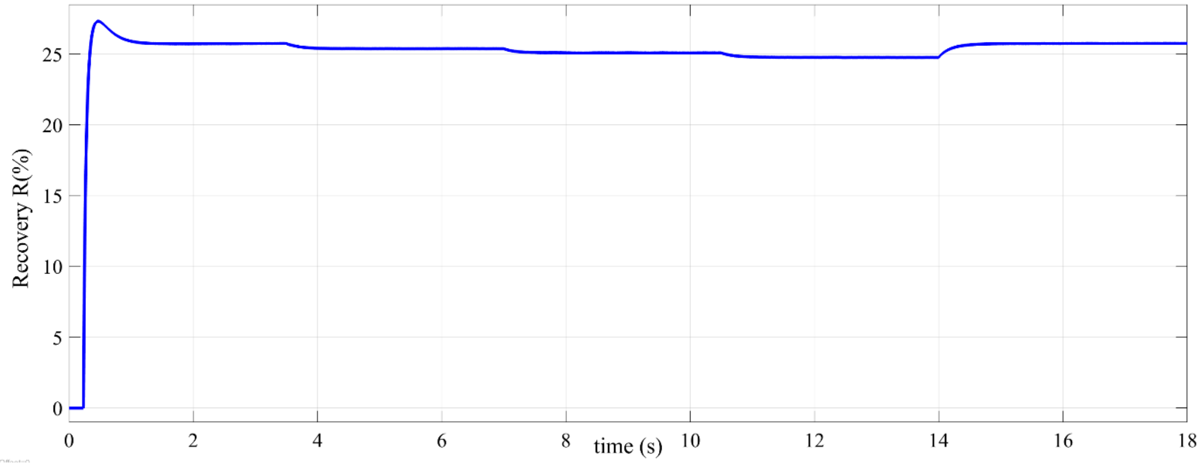

(C)

Figure 4.14. (A) Feed pressure, (B) feed and permeate flow rate, and (C) recovery under sudden irradiance variations.

At higher speeds, the induction machine can drive the high-pressure pump at a faster rate, resulting in increased pressure and flow rate of the feed water. This can lead to an increase in the recovery rate of the system, as more feed water is able to pass through the reverse osmosis membrane and be converted into permeate.

Conversely, at lower speeds, the induction machine drives the pump at a slower rate, resulting in decreased pressure and flow rate of the feed water. This can lead to a decrease in the recovery rate of the system, as less feed water is able to pass through the reverse osmosis membrane and be converted into permeate.

4.4.3. Shading effects on the desalination system

During partial shading, the PV generator may receive different levels of irradiance across its area, resulting in a significant reduction in output power. To address this issue, the

PV generator in the same configuration may be exposed to different irradiances, as shown in figure (4.15). In the first scenario, 47% of the modules (equivalent to 7 modules) receive less irradiance than the rest of the PV generator. In the second scenario, 67% of the area (the equivalent of 10 modules) receives less irradiance than the other modules.

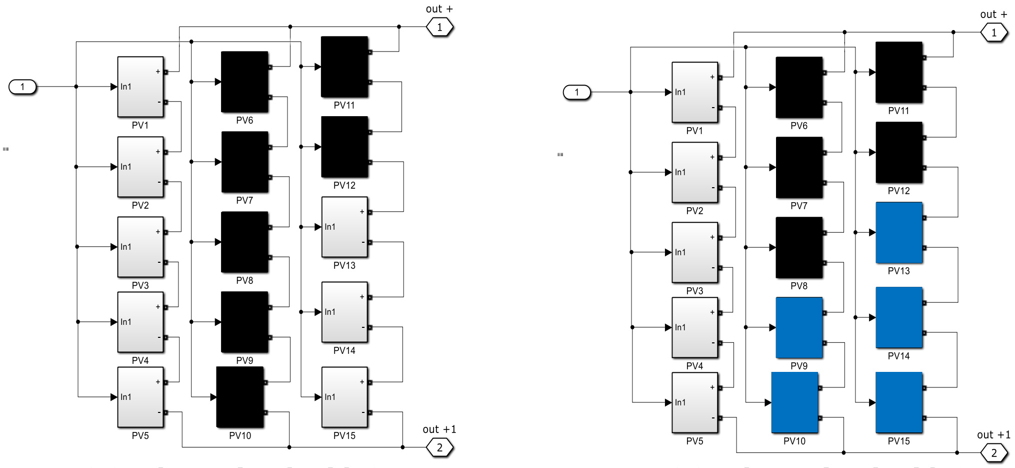

(A) White color (healthy)

Black color (47%shaded area)

(B) White color (healthy)

Black and blue colors (67% shaded area)

Figure 4.15. Different shading scenarios.

To optimize the performance of the RO-PV desalination system in these different scenarios, it is recommended to implement effective maximum power point tracking (MPPT) techniques, such as perturb and observe (PO), sliding mode control (SMC) and extremum seeking control (ESC). Additionally, a comparative study was conducted to evaluate the performance of the RO-PV desalination system using the three MPPT techniques. The study aimed to assess their effectiveness in optimizing the system's output and energy efficiency, as well as identify any differences between the techniques in terms of their hydraulic production or other relevant parameters.

- Scenario A: Eight modules are exposed to a constant irradiance of 1000 W/m^2, while the other seven modules are subjected to variable irradiance levels of 800 W/m^2, 700 W/m^2, 600 W/m^2, 500 W/m^2, and 400 W/m^2.

- Scenario B: Five modules receive 1000 W/m^2 of irradiance, while another five modules receive 800 W/m^2, and the remaining five modules are exposed to variable irradiance levels ranging between 400W/m^2 and 700W/m^2.

4.4.3.1.Scenario A

By applying three MPPT control methods: Perturb and Observe (P&O), Sliding Mode Control (SMC) and Extremum Seeking Control (ESC), it was found that the ESC is more effective than P&O and SMC in converging under the variable irradiance conditions, and it converges to the GMPP. In contrast, the P&O controller converges to LMPP as shown in figure (4.16). As indicated in table (4.4), the first-order sliding mode controller provides more power in the two studied scenarios, but failed to track the global optimum point, and stagnates on the local optimum one in the three other situations. These results indicate that the SMC method is not a desirable choice. Therefore, the next scenario and the following results in this chapter will compare PO and ESC and examine their influence on the desalination system and hydraulic quantities.

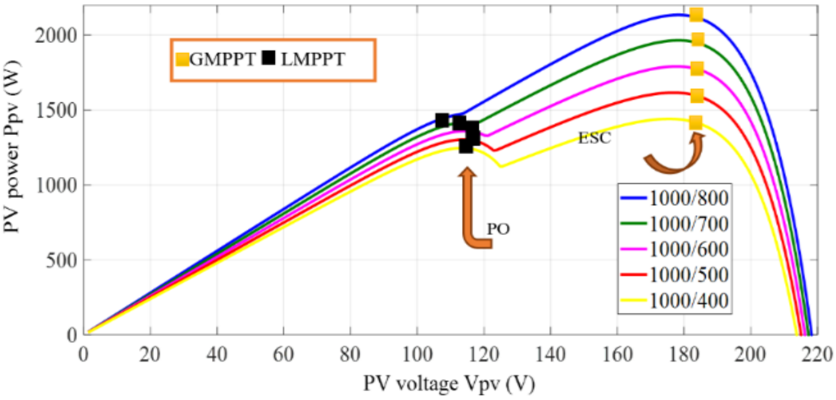

Figure 4.16. P-V characteristics of the shaded case.

The numerical simulation results presented in Table (4.4) were obtained by applying a fixed irradiance of 1000 W/m^2 to eight modules, while the irradiance were varied for the remaining part of the field from 800W/m^2 to 400W/m^2 in five cases. For each case, the voltage, the current, and the power were measured. These results show that the global optimum power ranges from 2135 W to 1441 W, while the local optimum power ranges from 1450 W to 1246 W. The power losses, which correspond to the difference between the global and the local MPPs are expressed as percentages. It was found that the power losses for the first case reached 32% and decreased to 13.5% for the fifth case when the irradiance of the shaded area was 400 W/m^2. Furthermore, the water quantity ranged from 24.7% to 10.3%.

Table 4.4 Shading effect on PV generator

E1	1000 W/m^2														
E2	800 W/m^2			700 W/m^2			600 W/m^2			500 W/m^2			400 W/m^2		
Case	1			2			3			4			5		
Type of the MPPT	PO (local)	ESC(Global)	SMC (local)	PO (local)	ESC (Global)	SMC (local)	PO (local)	ESC (Global)	SMC (local)	PO (local)	ESC (Global)	SMC (local)	PO (local)	ESC (Global)	SMC (local)
Pop (W)	1450	**2135**	**2035**	1418	**1965**	**1945**	1360	**1792**	**1350**	1303	**1616**	**1085**	1246	**1441**	**1245**
Vop (V)	110	**179.2**	**178.2**	115	**179.1**	**155.6**	114.3	**178.3**	**114.1**	114.4	**178.2**	**114**	114.1	**176.8**	**114.1**
Iop (A)	13.18	**11.92**	**11.2**	12.32	**10.97**	**12.5**	11.9	**10.05**	**11.83**	11.39	**9.07**	**9.5**	10.92	**8.15**	**10.91**
PWQ (m^3)	1.9755	**2.625**	**2.5**	1.9611	**2.48**	**2.45**	1.9	**2.3228**	**1.7499**	1.84	**2.1565**	**1.4479**	1.777	**1.982**	**1.7124**
Power Losses (%)															
PO	**32.1**			**27.8**			**24.1**			**19.4**			**13.5**		
SMC	**4.68**			**1.02**			**24.67**			**32.86**			**13.6**		
Water Quantity Losses WQL (%)															
PO	**24.7**			**20.9**			**18.2**			**14.7**			**10.3**		
SMC	**4.76**			**1.2**			**24.66**			**32.86**			**13.6**		

Figures (4.17) and (4.18) represent the percentage of power and water quantity losses for the proposed shaded case using only PO. The degradation of 100 W/m2 of irradiation from one case to another causes about 4.6% of power losses between the two successive cases, and it also causes water quantity losses of 3.6%.

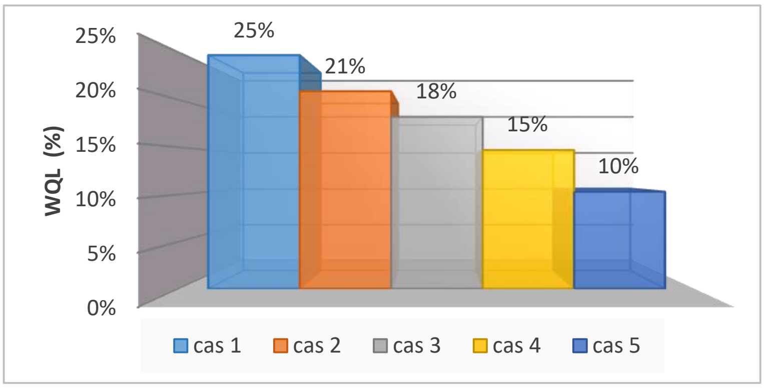

Figure 4.17. Power losses for the shaded case.

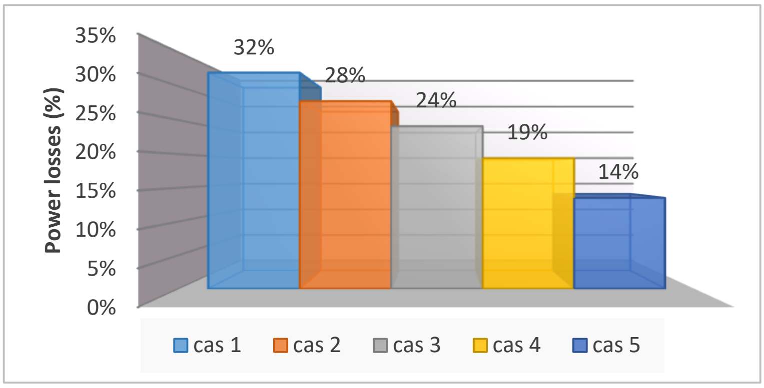

Figure 4.18. Water quantity losses for the shaded case.

4.4.3.2.Scenario B

The following figure presents simulation results obtained from partial shading cases. For scenario B, the P-V characteristics show three Maximum Power Points, of which two are considered as local maximum power points with a value less than the third maximum power point, which is the global maximum power point. It is evident that when the controller converges to the LMPP, the system's efficiency degrades, which negatively impacts the amount of freshwater produced by the system.

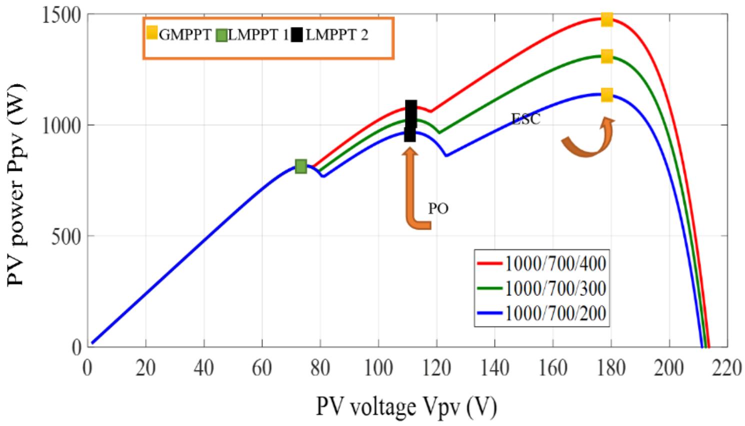

Figure 4.19. P-V Characteristics for Scenario B.

Scenario B contains three peaks corresponding to three different irradiances, as presented in table (4.5). The GMPP varies between 1486W and 1302W, while the power losses range from 15% to 29%.

Table 4.5. Shading effect on PV generator (scenario B)

E1	$1000\ \mathrm{W}/m^2$				
E2	$800\ \mathrm{W}/m^2$	$700\ \mathrm{W}/m^2$		$600\ \mathrm{W}/m^2$	
E3	$400\ \mathrm{W}/m^2$	$400\ \mathrm{W}/m^2$	$200\ \mathrm{W}/m^2$	$900\ \mathrm{W}/m^2$	$300\ \mathrm{W}/m^2$
Case	1	2	3	4	5
Global					
Pop	**1486**	**1478**	**1137**	**1834**	**1302**
Vop	179.6	177.5	177.1	179.6	176.2
Iop	8.27	8.33	6.42	10.21	7.39
Local 1					
Pop	**1135**	**1079**	**966.9**	**1304**	**967.1**
Vop	113.4	112.2	111.5	114.7	111.7
Iop	10	9.62	8.67	11.37	8.66
Local 2					
Pop	891	816.4	816.4	965.7	742.5
Vop	75.18	74.84	74.84	75.85	73.67
Iop	11.85	10.91	10.9	12.73	10.08
Power Losses (%)	**24**	**27**	**15**	**29**	**26**

Figure (4.20) shows the percentage of power losses for different cases in scenario B. The shading in scenario B causes power losses that vary between 15% and 29%.

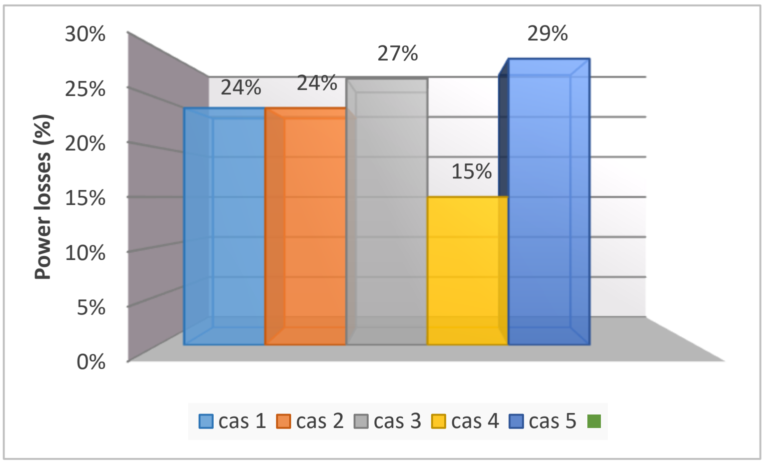

Figure 4.20. Power losses for scenarios B.

4.4.4. Real shading configuration

To study the influence of real data irradiance on the permeate water quantity, another test was conducted using MATLAB/Simulink. The test utilized real data corresponding to typical dates throughout the year as inputs, which were then applied to the entire PV-RO system.

4.4.4.1.Data and weather station

The weather data used in this study was collected from the Capricorn FLX station, which is located in the renewable energy laboratory at Biskra University. The weather station diagram used, based on several sensors including as Mechanical Wind Direction and Speed, Relative Humidity, Barometric Pressure (inside the Control Module), and Solar Radiation (up to two total), is shown in figure (4.21).

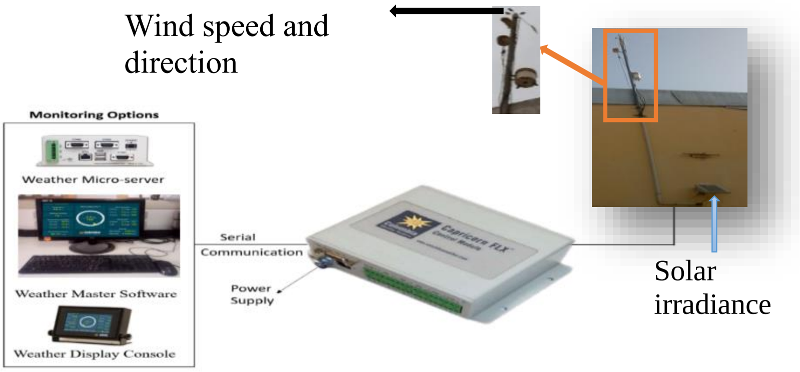

Figure 4.21. System diagram of Capricorn FLX Weather Station.

This station is used for spot measurements of temperature and irradiance, which are carried out in a similar way in the station. These measurements are taken every minute throughout the year. Figure (4.22) shows the profiles of solar irradiance and ambient temperature in minutes (525 600 min), over the year 2020. These profiles offer an important opportunity to study seasonal and long-term climate variations in this part of Algeria.

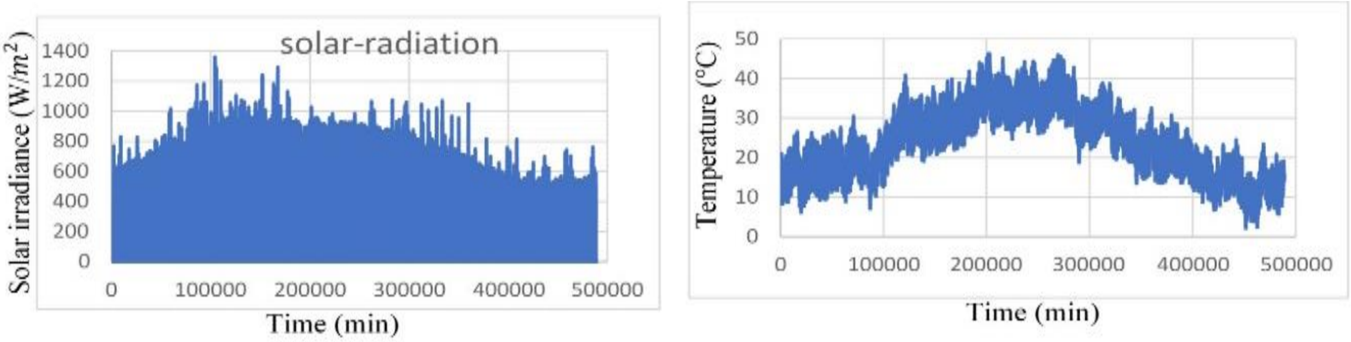

Figure 4.22. Meteorological parameters for Biskra over a year (2020).

Figure (4.23.a) and figure (4.23.b) show the monthly average temperature and monthly average solar irradiance data during the measurement period (2020). It can be noticed that the coldest month is December with an average temperature of 13.6 ∘C, and the warmest month is July with 35.3 ∘C. On the other hand, the maximum monthly mean irradiance is 497.6 W/m2 corresponding to July and the minimum mean irradiance is 268.7W/m²corresponding to December.

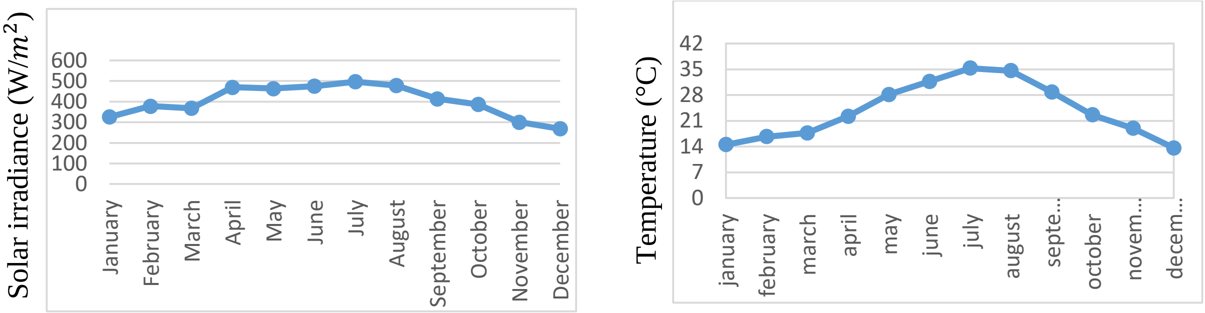

(a) Mean monthly solar irradiance

(b) Mean monthly air temperatures

Figure 4.23. Mean monthly values of meteorological parameters for Biskra over a year (2020)

4.4.4.2.Simulation of real shading configuration

The simulation was conducted for 16 hours with a sampling rate of 1e-5 s. To determine the quantity of water obtained, five days were selected from two seasons: three days from winter (January) and two days from summer (June).

- **RO unit performances for scenario 1**

For the first scenario, two days of June (08/06/2020 and 29/06/2020) are taken as inputs for the simulation. Figure (4.24) represents the evolution of the irradiances (a), the PV power (b), the feed water pressure (c), the feed water flow (d), the freshwater flow (e), and the recovery (f). By analyzing the results at the true solar noon, it can be seen that the irradiance level is around 900W/m² during the healthy day while it drops under 700 W/m² during the shaded day. Consequently, the PV power achieves the value of 2200 W during a sunny day and stays under 1500 W in presence of clouds. The hydraulic performances of the RO unit for these two days show that the feed water pressure can reach 8 bar for one day and don't exceed 6.5 bar during the other day. The impact on the feed water flow is correlative to the results. While for a sunny day, the feed water flow is approaching the peak of 9 l/min, it stagnates at 7 l/min for a clouded day.

The freshwater flow is found to be less than 2 l/min when the GPV is shaded while it can give more than 2.5 l/min during a sunny day. The recovery is around 30% without shading and less than this value in presence of shading conditions.

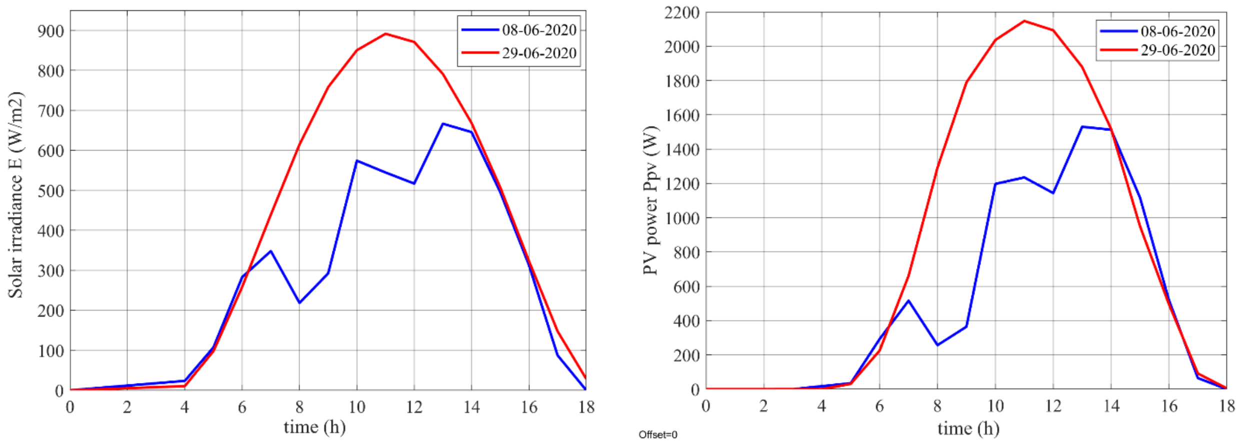

(a) (b)

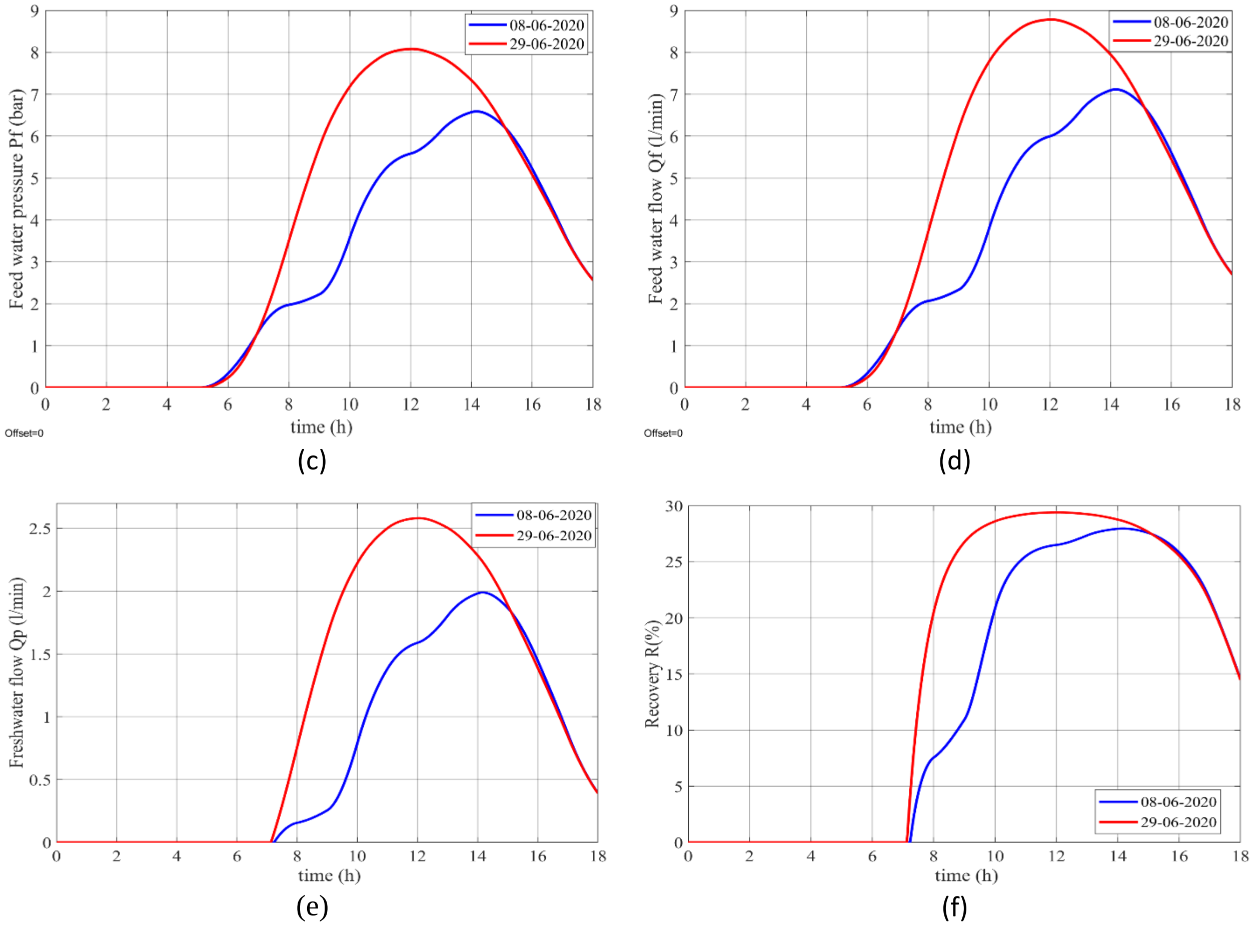

(c) (d) (e) (f)

Figure 4.24. Simulation results of the first scenario

(a) Hourly irradiance of two days in July. (b) The energy delivered by the GPV.

Hourly hydraulic quantities:

(c) Feed water pressure (d) Feed water flow (e) freshwater flow (f) Recovery

➢ RO unit performances for scenario 2

The second scenario includes two days in January, which are 25/01/2020 and 27/01/2020. Accordingly, figure (4.25) are represented the hourly irradiance (a), the energy delivered by the GPV (b), and the hourly hydraulic quantities: feed water pressure (c), feed water flow (d), fresh water flow (e) and recovery (f). By analyzing the results at the true solar noon, the irradiance level is around 600 W/m^2during the healthy day and consequently, the generated PV power is 1100 W while during the shaded day it drops under 300 W/m^2 generating a PV power under 400 W. Hence, the water quantity loss is about 82.91%, corresponding to a severe shading of 50%. The hydraulic performances of the RO unit for these two days show that the feed water pressure can reach upper to 5 bar on a sunny day and does not attend 3 bar on a cloudy day. The feed water flow is stagnating at the peak of 6 l/min for one day and is a rounding of 3 l/min for the other day.

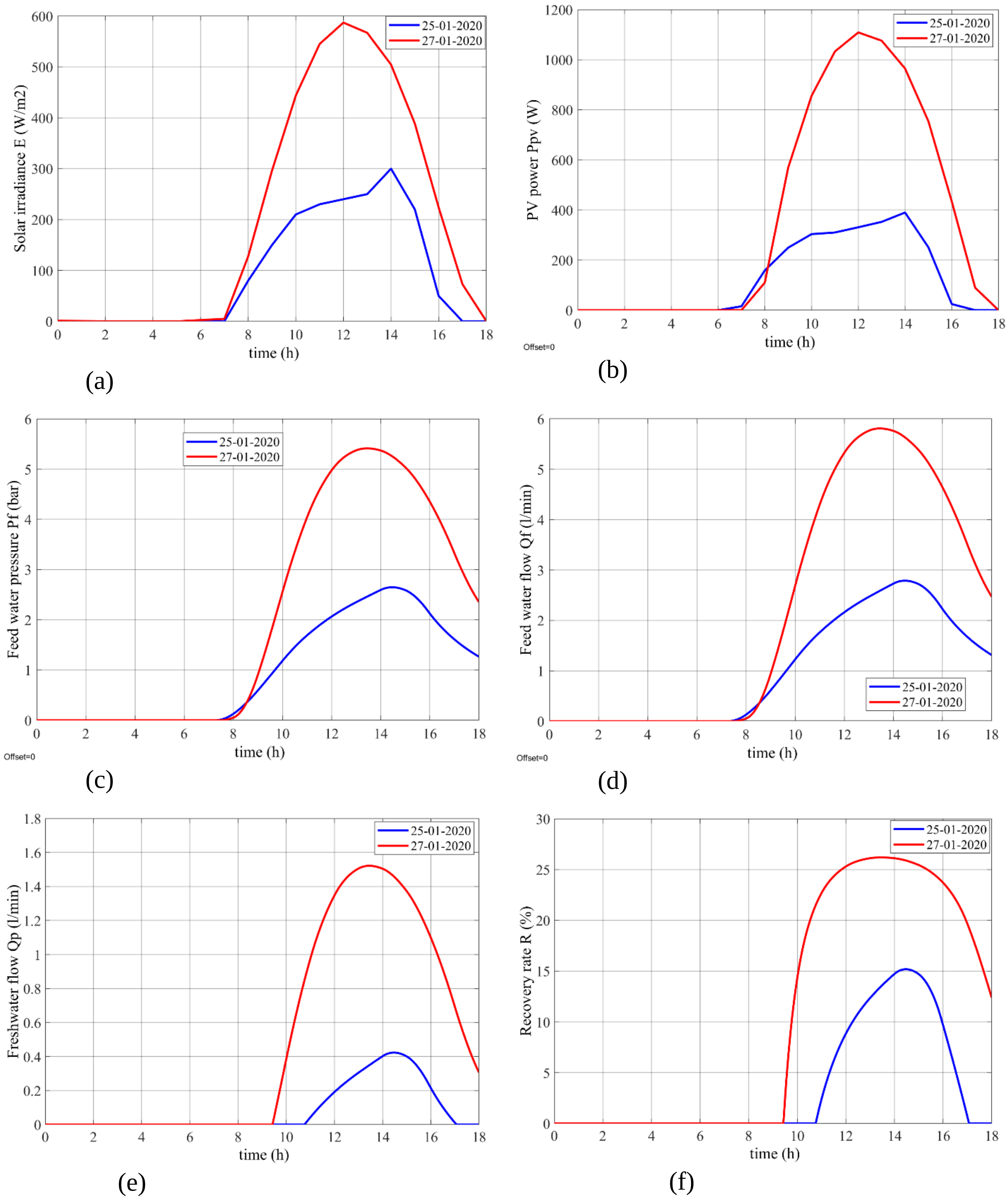

Figure 4.25. Simulation results of the second scenario

(a) Hourly solar irradiance for two days in January. (b) The energy delivered by the GPV.

Hourly hydraulic quantities:

(c) Feed water pressure (d) Feed water flow (e) freshwater flow (f) Recovery

- **RO unit performances for scenario 3**

The third scenario includes two days in January, which are 26/01/2020 and 27/01/2020. Figure (4.26) represents the hourly irradiance (a), the PV power (b), and the hourly hydraulic quantities: feed water pressure (c), feed water flow (d), fresh water flow (e), and recovery (f). It is a shading case of 8%. During the day, the curve of January 27, 2020, represents one global MPP at the solar irradiance of 560 W/m^2 and the maximum PV power point is 1100 W. The second curve attends the local MPP at the value of 5 hours for a solar irradiance of 450 W/m^2 and the PV power generated is 750W. Consequently, the feed water pressure achieves the value of 5.5 bar during the healthy day and is under 5.3 bar in presence of clouds. Meanwhile, the freshwater flow can reach 1.5 l/min for one day and does not exceed 1.4 l/min during the other day. These two typical days correspond to a recovery of 25%.

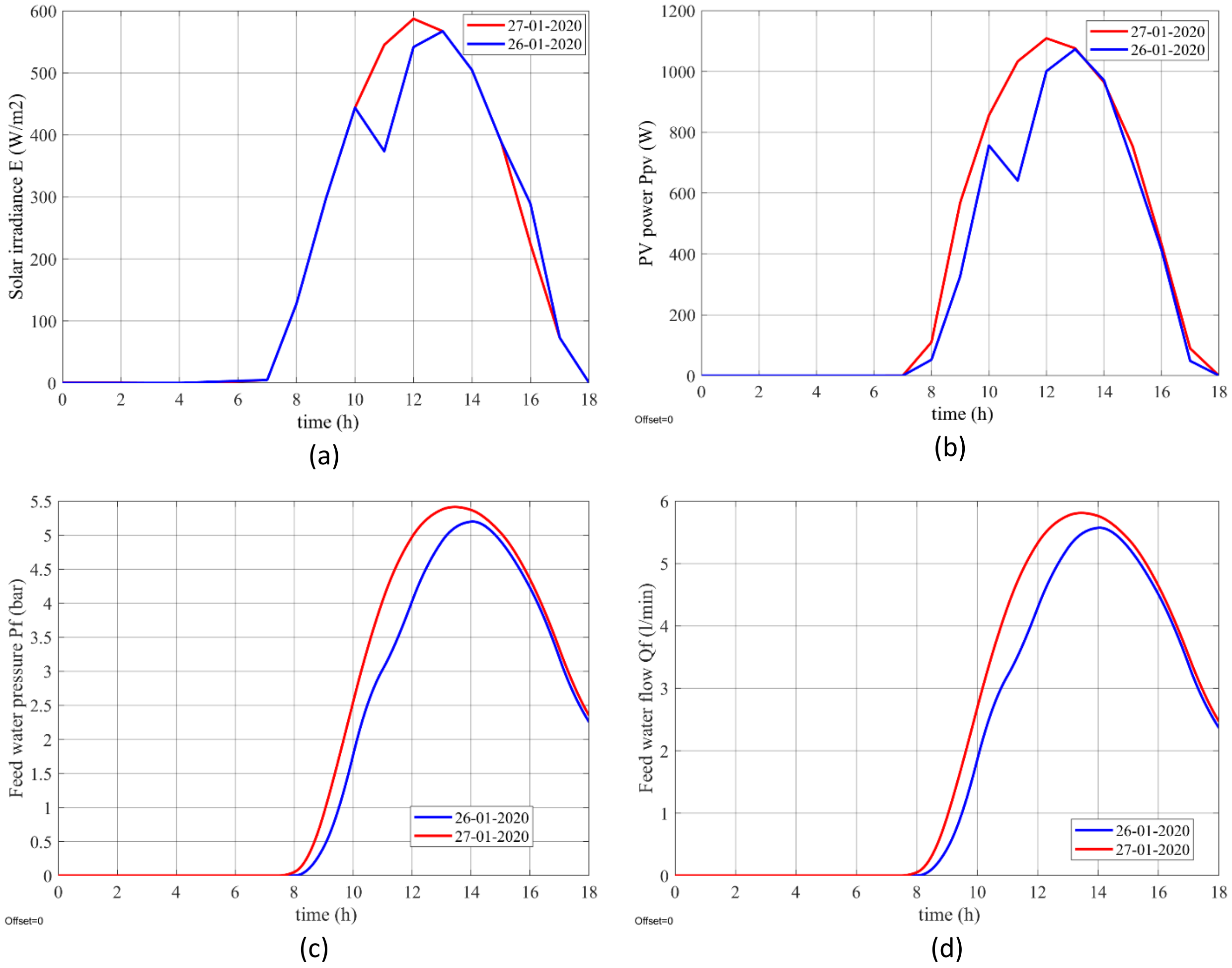

(a)

(b)

(c)

(d)

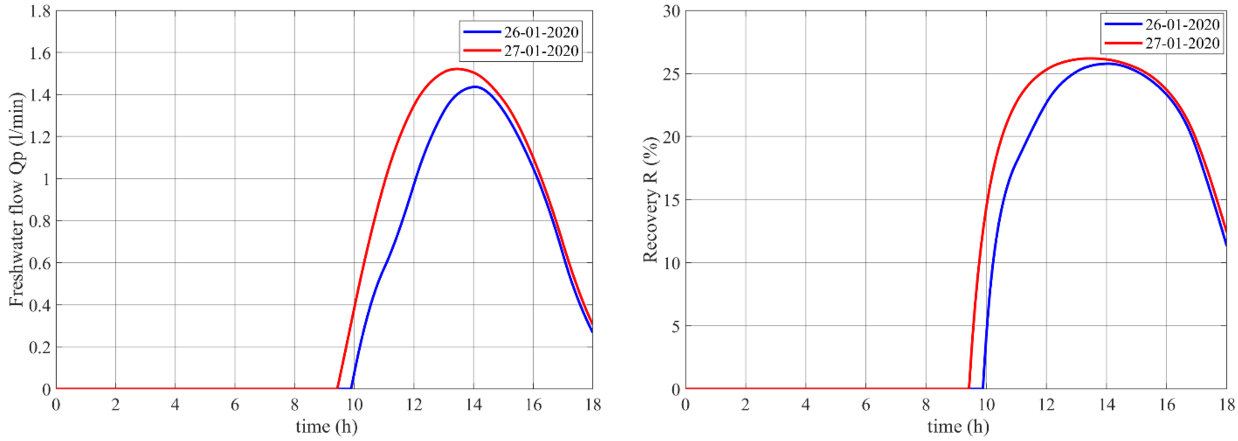

(e) (f)

Figure 4.26. Simulation results of the third scenario:

(a) Hourly solar irradiance for two days of January. (b) The energy delivered by the GPV.

Hourly hydraulic quantities:

(c) Feed water pressure (d) Feed water flow (e) freshwater flow (f) Recovery

Table (4.6) shows the water quantities and losses for the three real scenarios. On summer days, the sky is clear, and consequently, the percentage of losses is less than the winter days.

Table 4.6. Feed, permeate, and lose water quantity for different scenarios

day	08/06/2020	29/06/2020	25/01/2020	27/01/2020	26/01/2020
FWQ	$3.3077m^3$	$4.3850m^3$	$1.2318m^3$	$2.6805m^3$	$2.3878m^3$
PWQ	$0.7567m^3$	$1.1468m^3$	$0.0946m^3$	$0.5535m^3$	$0.4636m^3$
R (%)	22.88	26.15	7.68	20.65	19.42

Scenario	S_1	S_2	S_3
WQL (%)	34.02	82.91	16.24

The permeate water quantities corresponding to the profiles of 08/06/2020 and 29/06/2020 are $0.7567m^3$ and $1.1468m^3$ respectively, while the feed water quantities are 3.3077 m^3 and $4.3850m^3$ respectively. Consequently, the water quantity losses represent 34.02 % for the chosen days. By analyzing the table results, it can be seen that the water quantity losses are ranging from 16.24% to 82.91%.

4.5. Conclusion

This chapter has proposed a high-performance control scheme for a PV desalination system based on an induction motor (IM), with an improved MPPT (Extremum Seeking Control). The control scheme uses a DTC algorithm with twelve sectors to control the IM drive, with a Lyapunov control to maintain the DC-link voltage constant at the desired reference value.

This study has been carried out using MATLAB/Simulink software under uniform, non-uniform irradiance conditions and real shading configuration. According to the simulation results presented in this chapter, the following major conclusions can be summarized:

- 13% to 32% of power losses occur during the real shading case equivalent to 10% to 25% of water quantity losses.
- During a sunny day, the freshwater quantity produced by the RO unit is $2{,}6805\ m^3$, but the shading conditions affect widely the production, which drops to $1{,}2318\ m^3$ for the shaded case.
- By using the extremum-seeking controller, which has proven its ability to converge to the GMPP compared with the PO controller, the savings of power are ranging between 195 W and 685 W.

In the next chapter, we intend to investigate the experimental implementation of the whole system investigated in this chapter.

Chapter 05

Experimental Results

Chapter 05: Experimental results

5.1. Introduction

The realization of a RO desalination unit powered by renewable energies without batteries requires the development of a control law to allow, on the one hand, to stabilize the DC bus voltage. On the other hand, it will allow controlling the variation of the hydro-mechanical quantities via the moto pump and the RO membrane while respecting the various technological constraints. The combination of the DC control law with the AC control law will allow the optimization of the global system operation and maximize the water-produced quantity.

Four modules have been used in a series, which gives us a very high power compared to the rated power of the used machine (IM). To solve this problem, the boost converter is put in power regulation. This allows us to extract the power required by the load and at the same time maintain the bus voltage constant.

The two main objectives are the application of the power regulation to the GPV side in order to overcome the load-requested power and maintain the DC bus voltage constant. On the moto-pump side, the DTC control (12 vectors) is applied to convert the extracted PV power to mechanical energy at the motor shaft and then to hydraulic power at the level of the RO unit. As the pump was not available, a pump emulator with the parameters of a real pump was realized by a buck chopper, which is connected to the RO membrane model.

This chapter is arranged as follows: Following the introduction, Section 2 presents the test bench description (PV generator, DC/DC and DC/AC converters, moto pump, and RO unit) involved in this study. In Section 3, the LQR (linear quadratic regulator) is explained as a technic to extract the reference speed that occurs in real time. In this section, the PV power and the DC bus regulation are also explained. In the last section, the experimental results are done using Dspace 1104, then taken and interpreted. Finally, this chapter is ended with a conclusion.

5.2. Test bench Description:

A small-scale test bench, represented in figure (5.1), has been set up in the Laboratory of Electrical Engineering of Biskra (LGEB). The test bench mainly comprises the following parts:

- A PV generator (PVG) is formed by the association of four modules connected in series, branded SHARP. Each module is of mono-crystalline type, made up of 72 cells in series, producing a peak power of 175 Wp under standard conditions (STC: 1000 W/ m², 25°C), at an optimal voltage of 35.4 V. The photovoltaic field is fixed on the roof of the laboratory, oriented due south, with an inclination equal to the latitude of the place (34°).
- A boost-type DC/DC converter, consisting of an IGBT switch and an antiparallel diode, is provided with galvanic isolation. Two 10 mH inductances connected in series are used to filter currents.
- A three-phase inverter, branded SEMIKRON, consists of three IGBT arms and is equipped with a filter capacitor C of 1100 μF.
- Hall sensors carry out various current and voltage measurements.
- Pump emulator: is built from a buck chopper fed by a DC machine. The buck chopper is connected to a variable resistor through a capacitor of 2200 μF.
- Three phase induction machine of 270 W.
- DC source of excitation and three phase power supply.
- A rectifier is an electrical device that converts alternating current (AC) to direct current (DC). It is used to adapt a three-phase power supply to feed an induction machine.
- An incremental encoder speed sensor.
- A DSpace 1104 board is used for the implementation of the control algorithms, where the compilation is performed directly from the algorithm in MATLAB/Simulink. An interface board that adapts the control signal levels realizes the connection between the dSpace board and the power converters.
- Two 5/15 adaptation cards are interface cards that enable communication between devices or systems that use 5V or 15V logic levels. They provide level-shifting functionality to ensure compatibility between the two voltage levels.
- Two scopes to visualize the results.

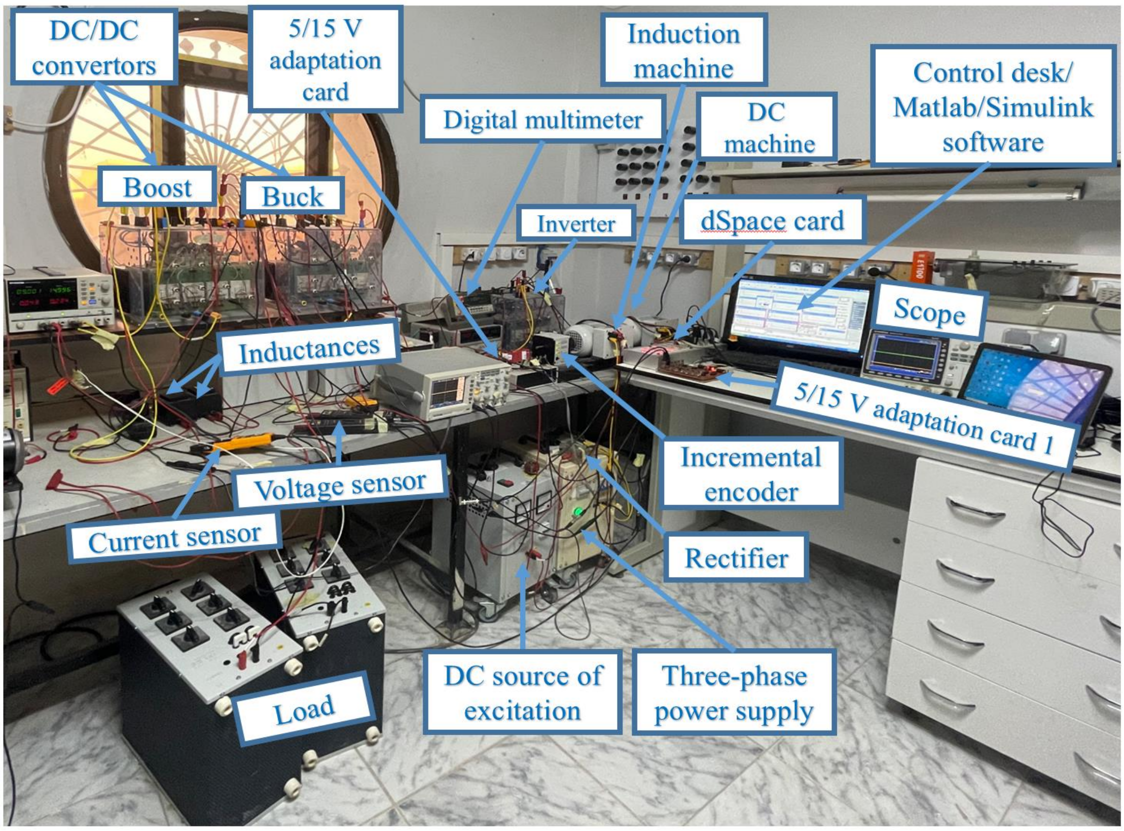

Figure 5.1: Experimental test bench.

5.3. Control scheme proposed:

The complete control scheme of the proposed PV/RO desalination system is depicted in Figure (5.2). The system requires regulation for the following functions:

- Regulating the PV generator is necessary to ensure that the load receives the required power, and for regulating the Vdc voltage.
- Electromechanical power conversion for IM drive, which is assured by the DTC control with 12 vectors
- Linear Quadratic Regulator (LQR) for good control of the hydraulic quantities.

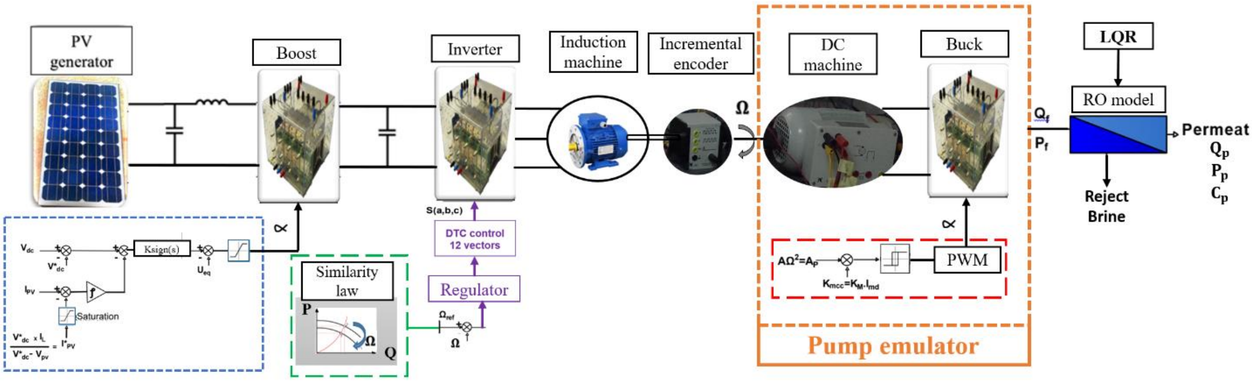

Figure 5.2: Synoptic of the proposed control scheme for the PV-RO desalination system.

5.3.1. Sliding Mode Control (SMC) of the boost chopper linked to the PV generator:

We used four 175 W modules with an optimal voltage of 35 V to achieve the desired voltage. With these four modules, we obtained an optimal voltage of 140 V, which can be increased to 250 V, the desired bus voltage. The four modules provide an optimal power of 700 W, which is more than the load demand and therefore we cannot operate on MPPT. In this case, the use of SMC serves two purposes: first, to adjust the PVG power according to the load demand, and second, to maintain a constant bus voltage (Vdc). The corresponding system configuration is shown in figure (5.2).

The sliding mode control is known as a variable structure control technique, which alters the nonlinear system dynamics by applying a discontinuous control input and forces the state trajectories to be along the sliding boundaries. The sliding mode method is insensitive to uncertainties due to rapid switching between the continuous structures. The motion of the nonlinear system sliding along these boundaries is called the sliding mode. The geometrical locus consisting of the predetermined boundaries is known as the sliding manifold [139].

The sliding manifold for the used boost converter is determined by:

$$\mathrm{S} = (\mathrm{V}_{\mathrm{DC}} - \mathrm{V}_{\mathrm{DC}}^{*}) + \rho\left(\mathrm{I}_{\mathrm{pv}} - \mathrm{I}_{\mathrm{pv}}^{*}\right) \tag{5.1}$$

Desired sliding manifold performance is accomplished by tuning the sliding coefficient ρ. To achieve the reachability condition, Equation (5.2) must be satisfied:

$$S.\dot{S} < 0 \tag{5.2}$$

The inductor current is highly dependent on the load and output reference voltage. The desired voltage at the output is achieved when $\mathrm{S} = (\mathrm{V}_{\mathrm{DC}} - \mathrm{V}_{\mathrm{DC}}^{*}) = 0$, and $\dot{S}$ becomes zero $\dot{S} = \dot{\mathrm{V}}_{\mathrm{dc}} = 0$.

From the second chapter:

$$\begin{cases} \frac{\mathrm{dV_{dc}}}{\mathrm{dt}} = \frac{1-\alpha}{\mathrm{C}}\, \mathrm{I_{pv}} - \frac{1}{\mathrm{C\,R_L}}\, \mathrm{V_{dc}} & (5.3) \\ \frac{\mathrm{dI_{pv}}}{\mathrm{dt}} = -\frac{(1-\alpha)}{\mathrm{L}}\, \mathrm{V_{dc}} + \frac{1}{\mathrm{L}}\, \mathrm{V_{pv}} & (5.4) \end{cases}$$

$$\frac{\mathrm{dV_{dc}}}{\mathrm{dt}} = 0 \xRightarrow{\text{implies}} \alpha = 1 - \frac{\mathrm{V_{dc}}}{\mathrm{R_L\, I_{pv}}} \tag{5.5}$$

By replacing (5.5) in the equation (5.4):

$$\frac{dI_{pv}}{dt} = \frac{1}{L} V_{dc} \left(1 - \frac{V_{dc}}{R_L I_{pv}}\right) \tag{5.6}$$

Therefore, the reference inductor current is given by:

$$I_{pv}^{*} = \frac{V_{DC}^{*}}{V_{DC}^{*} - V_{pv}} \times I_L \tag{5.7}$$

The first-order sliding mode control has been used; while the control u consists of u_{eq} and u_s, and can be defined as:

$$\alpha = \alpha_{eq} + \alpha_s \tag{5.8}$$

The equivalent control α_{eq} is solved from $\dot{S} = 0$.

$$\dot{S} = \frac{dV_{dc}}{dt} + f\frac{dI_{pv}}{dt} - f\frac{dI_{pv}^{*}}{dt} = 0 \tag{5.9}$$

By replaying $\frac{dV_{dc}}{dt}$, $\frac{dI_{pv}}{dt}$, I_{pv}^{*} with their equations (5.3), (5.4), (5.7), respectively α_{eq} is defined by:

$$\alpha_{eq} = \frac{f\left[\frac{V_{DC} - V_{pv}}{L}\right] + f\frac{d(I_{pv}^{*})}{dt} - \left[\frac{1}{C}\left(I_{pv} - I_L\right)\right]}{\frac{f}{L} V_{DC} - \frac{1}{C} I_{pv}} \tag{5.10}$$

α_s is the switching control:

$$\alpha_s = \begin{cases} -k_0 \, \mathrm{sgn}(S), & \text{if } S > \left|\frac{S}{S_0}\right| \\ -k_0 \, \frac{S}{S_0} \, , & \text{if } S < \left|\frac{S}{S_0}\right| \end{cases} \tag{5.11}$$

Where $S_0 = 10$, and k_0 is a positive constant and the signum function sgn(S) is defined as:

$$\mathrm{sgn}(S) = \begin{cases} 1 & S > 0 \\ 0 & S = 0 \\ -1 & S < 0 \end{cases} \tag{5.12}$$

5.3.2. Control of the buck chopper of the pump emulator:

The experimental bench used to simulate the pump associated with the asynchronous cage machine is shown in Figure (5.3). To generate a torque resistance similar to that of a centrifugal pump, a torque simulator was utilized. The simulator is designed to control the buck converter so that the separately excited DC motor generates a torque resistance ($K_{mcc} =$

$K_m\, I_{ind}$) similar to that of a pump in the form of $A\,\Omega^2$, where w is the mechanical speed measured by the incremental encoder, I_{ind} is the current measured at the armature output, and A, K are constants. This control is achieved using hysteresis to assure the equality of the two following torques ($K_{mcc} = A_p$):

$$A_p = A\,\Omega^2 \tag{5.13}$$

$$K_{mcc} = K_m\, I_{ind} \tag{5.14}$$

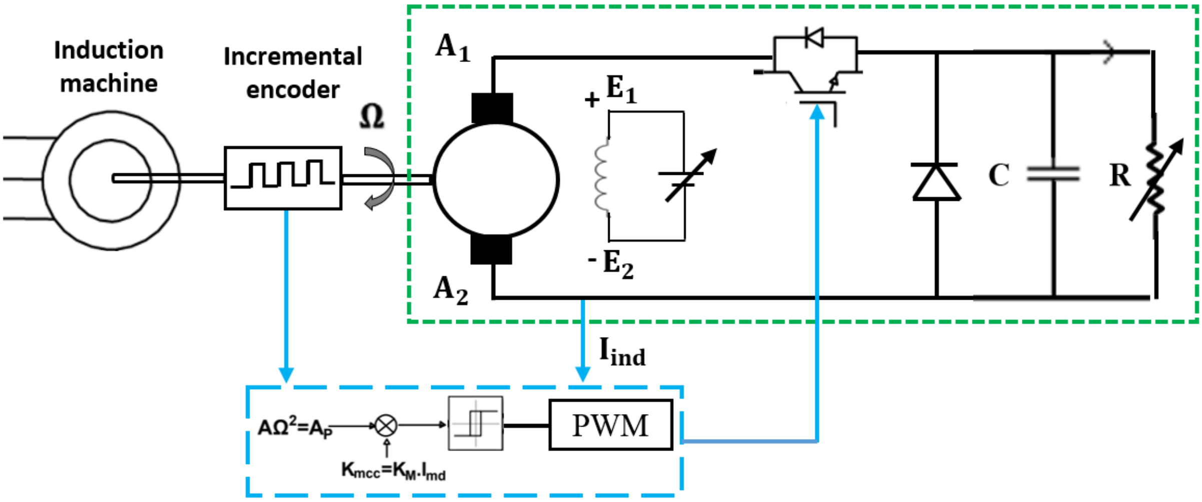

Figure 5.3: Experimental configuration of the pump emulator.

The pump parameters used in this chapter are parameters of a centrifugal pump, type LVS(R)3. It has a nominal flow rate of 50 l/min and a maximum pressure of 24 bar with a power of 370 W and a maximum efficiency of 55%. The characteristic curves of the pump (H=f(Q)) is shown in Annex 3 for different values of speed (157 rad/s, 100 rad/s, and 130 rad/s) and pump parameters.

5.3.3. LQR control of the membrane:

The general RO model was originally presented by the dynamical system given by [140]. This is a multi-input–multi-output (MIMO) model that represents a small-scale brackish water desalination unit. The feed water is pumped into the membrane module with high pressure. This pressure is in excess of the osmosis pressure and forces part of the feed water to permeate through the membrane array to become fresh water. By properly controlling the motor pump speed, one can get product water with the desired flow and concentration. The model equation describing the dynamical behaviors of the desalination system is given in [141].

Many variables need to be monitored and/or controlled such as operating temperature, permeate pressure (Pp), and concentration... The main variables that are controlled for the accurate performance of the RO membrane are the permeate flow rate (Qp), the permeate conductivity (Cp), the feed pressure (Pf), and the brine (feed) flow rate (Qb or Qf). The RO membrane is modeled as a dynamic coupled MIMO system, formulated as:

$$\begin{bmatrix} Q_p \\ C_p \end{bmatrix} = \begin{bmatrix} G_{11}(s) & G_{12}(s) \\ G_{21}(s) & G_{22}(s) \end{bmatrix} \begin{bmatrix} \Omega_r \\ \theta_r \end{bmatrix} \tag{5.15}$$

Where the parameter values provided by the identification procedure is shown in Table 5.1:

Parameters	K_{11}	K_{12}	K_{21}	K_{22}	τ_{11}	τ_{22}	ω_{01}	ω_{02}	ξ_1	ξ_2
Values	0.1242	0.1228	0.1278	0.1144	1	1	1.5	2.15	0.5	0.75

$$G_{11}(s) = \frac{K_{11}}{\tau_{11}s+1} \tag{5.16}$$

$$G_{12}(s) = \frac{K_{12}\omega_{01}^2}{p^2+2\xi_1\omega_{01}s+\omega_{01}^2} \tag{5.17}$$

$$G_{21}(s) = \frac{K_{21}\omega_{02}^2}{p^2+2\xi_2\omega_{02}s+\omega_{02}^2} \tag{5.18}$$

$$G_{22}(s) = \frac{K_{22}}{\tau_{22}s+1} \tag{5.19}$$

This model is obtained as an emulated system, which fits the performances of the TM700 membrane, described in Annex 03.

This model was inspired by a dynamic model identification given in [139,140], deduced via various speed and brine valve position steps.

As a contribution of the RO membrane, the famous Linear Quadratic Controller (LQR) is proposed to adequately control both the permeate flow rate Q_p and the fresh water concentration C_p close the set values Q_{p-ref} and C_{p-ref}.

To do so, the membrane model (5.15) is first described in a MIMO state space representation, given by:

$$\dot{X} = A\,X + B\,U \tag{5.20}$$

Where the state vector X and the control vector U are defined:

$$X = \begin{bmatrix} Q_p \\ \dot{Q}_p \\ C_p \\ \dot{C}_p \end{bmatrix}, U = \begin{bmatrix} \Omega_r \\ \theta_r \end{bmatrix}$$

The constants matrices A and B are defined as:

$$A = \begin{bmatrix} -\frac{1}{\tau_{11}} & 1 & 0 & 0 \\ -\omega_{01}^2 & -2\xi_1\omega_{01} & 0 & 0 \\ 0 & 0 & -\frac{1}{\tau_{21}} & 1 \\ 0 & 0 & -\omega_{02}^2 & -2\xi_2\omega_{02} \end{bmatrix}$$

$$B = \begin{bmatrix} \frac{K_{11}}{\tau_{11}} & 0 \\ 0 & K_{12}\omega_{01}^2 \\ 0 & \frac{K_{22}}{\tau_{22}} \\ K_{21}\omega_{02}^2 & 1 \end{bmatrix}$$

To track perfectly the set values of the Q_{p-ref} and C_{p-ref} additional states are considered as:

$$x_5 = \int_0^t (x_1 - x_{1ref})\,dt \tag{5.21}$$

$$x_6 = \int_0^t (x_3 - x_{3ref})\,dt \tag{5.22}$$

Where

$$x_{1ref} = Q_{pref}\ ,\ x_{3ref} = C_{pref}$$

So

$$x_5^{\cdot} = x_1 - x_{1ref}\ ,\ x_6^{\cdot} = x_3 - x_{3ref}$$

The augmented dynamic system is now formulated as:

$$\dot{X}_{aug} = A_{aug}\,X_{aug} + B_{aug}\,U + D\,Z \tag{5.23}$$

Where

$$A_{aug} = \begin{bmatrix} -\frac{1}{\tau_{11}} & 1 & 0 & 0 & 0 & 0 \\ -\omega_{01}^2 & -2\xi_1\omega_{01} & 0 & 0 & 0 & 0 \\ 0 & 0 & -\frac{1}{\tau_{21}} & 1 & 0 & 0 \\ 0 & 0 & -\omega_{02}^2 & -2\xi_2\omega_{02} & 0 & 0 \\ 1 & 0 & 0 & 0 & 0 & 0 \\ 0 & 0 & 1 & 0 & 0 & 0 \end{bmatrix}$$

$$B_{aug} = \begin{bmatrix} \frac{K_{11}}{\tau_{11}} & 0 \\ 0 & K_{12}\omega_{01}^2 \\ 0 & \frac{K_{22}}{\tau_{22}} \\ K_{21}\omega_{02}^2 & 1 \\ 0 & 0 \\ 0 & 0 \end{bmatrix}$$

$$D_{aug} = \begin{bmatrix} 0 & 0 & 0 & 0 & 0 & 0 \\ 0 & 0 & 0 & 0 & 0 & 0 \\ 0 & 0 & 0 & 0 & 0 & 0 \\ -1 & 0 & 0 & 0 & 0 & 0 \\ 0 & 0 & -1 & 0 & 0 & 0 \end{bmatrix}$$

After that, the reference motor speed Ω_{r-ref} and brine value position θ_{r-ref} are now deduced, via the minization of an infinite quadratic cost function, related to the augmented state X_{aug}, as follows:

$$J = \int_0^\infty \left[X_{aug}^T(t)\, Q\, X_{aug}(t) + U^T(t)\, R\, U(t)\right] dt \qquad (5.24)$$

Where Q and R denote weight matrixes, chosen as two liberty degrees to adjust a trade-off between dynamic response and the counted effort.

Q is a [n x n] squarted positive definite matrix, chosen as follows:

$$Q = \sigma \begin{bmatrix} 1 & 0 & 0 & 0 & 0 & 0 \\ 0 & 1 & 0 & 0 & 0 & 0 \\ 0 & 0 & 1 & 0 & 0 & 0 \\ 0 & 0 & 0 & 1 & 0 & 0 \\ 0 & 0 & 0 & 0 & 1 & 0 \\ 0 & 0 & 0 & 0 & 0 & 1 \end{bmatrix} \qquad (5.25)$$

Where σ is adjusted to obtain the desired dynamic performance

The R matrix penalizes the unwanted control inputs during transient state.

In the present study, R is chosen a positive definite matrix as:

$$\mathrm{R} = \begin{bmatrix} 1 & 0 \\ 0 & 1 \end{bmatrix} \tag{5.26}$$

The control inputs are then deduced as a stat feedback according to the state famous Ricatti theory:

$$\mathrm{U} = -\mathrm{R}^{-1}\,\mathrm{B}_{\mathrm{aug}}^{\mathrm{T}}\,\overline{\mathrm{P}}\,\mathrm{X}_{\mathrm{aug}} \tag{5.27}$$

$$\mathrm{U} = -\overline{\mathrm{K}}\,\mathrm{X}_{\mathrm{aug}} \tag{5.28}$$

Where $\overline{\mathrm{P}}$ and $\overline{\mathrm{K}}$ denote the static Ricatti matrix and gain respectively:

$$\overline{\mathrm{K}} = \mathrm{R}^{-1}\,\mathrm{B}_{\mathrm{aug}}^{\mathrm{T}}\,\overline{\mathrm{P}} \tag{5.29}$$

The Ricatti matrix $\overline{\mathrm{P}}$ is [n x n] symmetric positive definite matrix, solution of the algebraic equation:

$$\overline{\mathrm{P}}\,\mathrm{A}_{\mathrm{aug}} + \mathrm{A}_{\mathrm{aug}}^{\mathrm{T}}\,\overline{\mathrm{P}} - \overline{\mathrm{P}}\,\mathrm{B}_{\mathrm{aug}}\,\mathrm{R}^{-1}\,\mathrm{B}_{\mathrm{aug}}^{\mathrm{T}}\,\overline{\mathrm{P}} + \mathrm{Q} = 0 \tag{5.30}$$

In the present work, both $\overline{\mathrm{P}}$ and $\overline{\mathrm{K}}$ and obtained using the MATLAB instruction:

$$[\mathrm{K,S,e}]=\mathrm{LQR}(\mathrm{A}_{\mathrm{aug}}, \mathrm{B}_{\mathrm{aug}},\mathrm{Q,R}) \tag{5.31}$$

Where S= $\overline{\mathrm{P}}$

And e denotes the closed-loop eigenvalues, solution of $\left|\mathrm{eq.}(5.15) - \left(\mathrm{A}_{\mathrm{aug}} - \mathrm{B}_{\mathrm{aug}}.\overline{\mathrm{K}}\right)\right|$:

$$\mathrm{e} = \begin{bmatrix} -33.5020 \\ -0.3332 \\ -12.9249 \\ -36.8308 \\ -13.5559 \\ -0.2302 \end{bmatrix} \tag{5.32}$$

The closed loop can now expressed as:

$$\dot{\mathrm{X}}_{\mathrm{aug}} = (\mathrm{A}_{\mathrm{aug}} - \mathrm{B}_{\mathrm{aug}}.\overline{\mathrm{K}})\,\mathrm{X}_{\mathrm{aug}} \tag{5.33}$$

So the control input can be now deduced as:

$$\begin{bmatrix}\Omega_{ref}\\ \theta_{ref}\end{bmatrix} = -\begin{bmatrix} 1.1153 & 0.5924 & -0.0000 & -0.0000 & 4.4721 & 0.0000\\ -0.0000 & -0.0000 & 0.6648 & 0.7273 & -0.0000 & 4.4721\end{bmatrix}\begin{bmatrix}x_1\\ x_2\\ x_3\\ x_4\\ x_5\\ x_6\end{bmatrix} \quad (5.34)$$

The infinite horizon LQR control can efficiently applied if the system given in (5.23) should be fully controlled.

Control ability test:

This condition can be checked if the following matrix equation

$$\text{Rank}\left|A_{aug} \quad A_{aug}^{T}B_{aug} \quad A_{aug}^{2}B_{aug} \quad A_{aug}^{3}B_{aug} \ldots\ldots A_{aug}^{(n-1)}B_{aug}\right| = n \quad (5.35)$$

The rank of the previous matrix equals 6, which the dimension of the augment state vector X_{aug}, and consequently, all the state variables converge to the set values in a finite time.

5.4. Experimental results:

Two tests were carried out in the laboratory on Tuesday, December 20, 2022, on a clear day. The first test presents the results of the whole system for a fixed state, to determine the hydraulic production obtained by the PV generator. The second test involves a variation in the flow rate Qp, to observe the influence of this variation throughout the chain.

5.4.1. Case one:

This section presents the experimental results obtained for a constant freshwater flow, where the hydraulic quantities are fixed. Figure (5.4) shows the plot of the PV generator power for the entire test period, along with the useful power delivered by the induction machine. The PV power oscillates around 250 W, while the useful power remains fixed at 188.4 W.

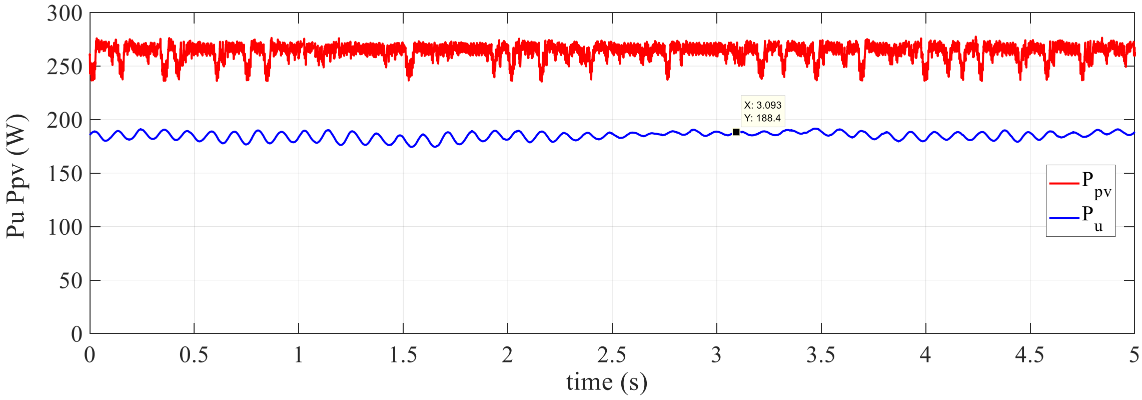

Figure 5.4: Experimental curves of the power Ppv and Pu.

For a PV-generated power of 250W and a fresh water flow rate of 1 l/min (figure (5.5)), the machine works with a power of 188.4 W and a speed of 140 rad/s. This section ensures a regulated and fixed DC bus at 250 V with a sinusoidal stator current. At these values, the flux is 0.8 Wb, and the resistant torque follows Tem (0.8 N.m).

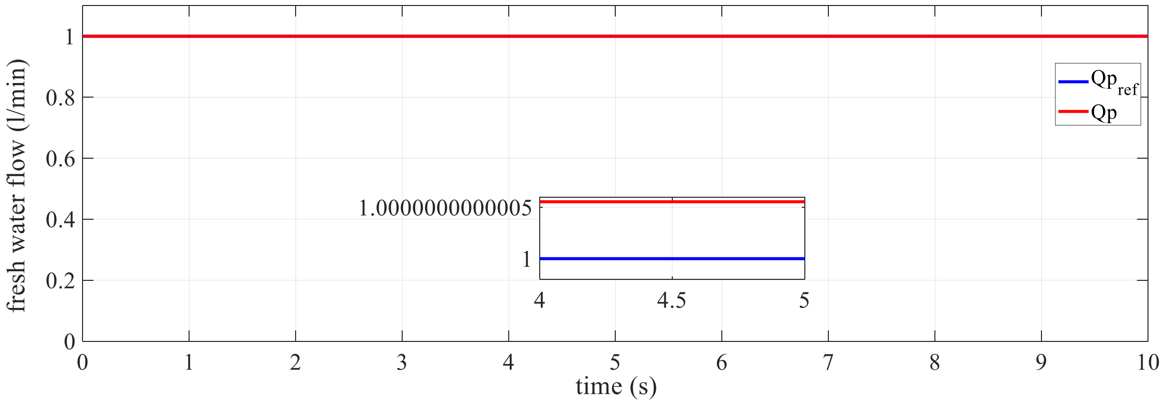

Figure 5.5: Experimental curves of the freshwater flow and its reference with zoom.

Figures (5.6), (5.7), and (5.8) illustrate freshwater concentration, pressure, and recovery, respectively. Additionally, it can be observed that at a pressure of 15 bar and a concentration of 6mg/l, the flow rate is 0.8 l/min and the recovery is 21.6%.

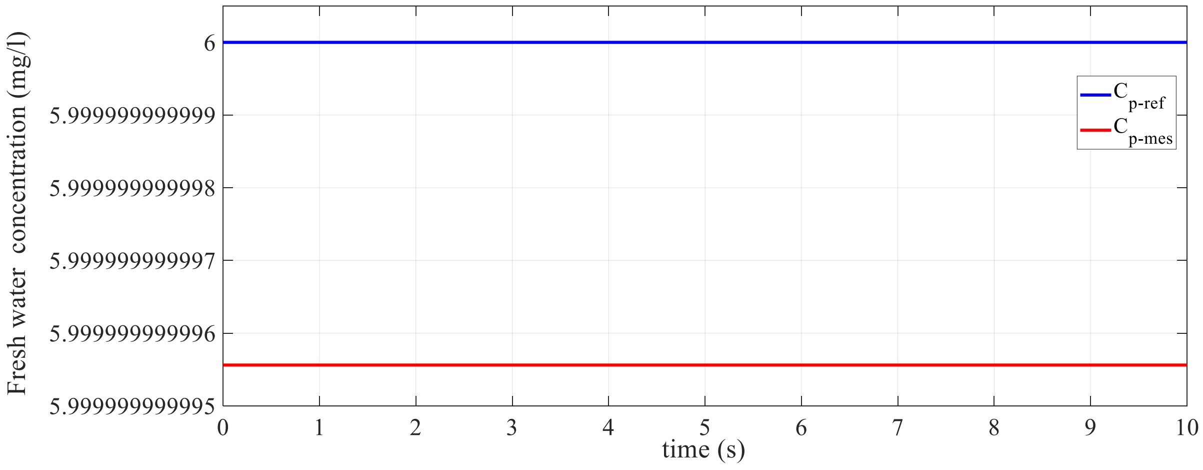

Figure 5.6: Experimental curves of the freshwater concentration and its reference.

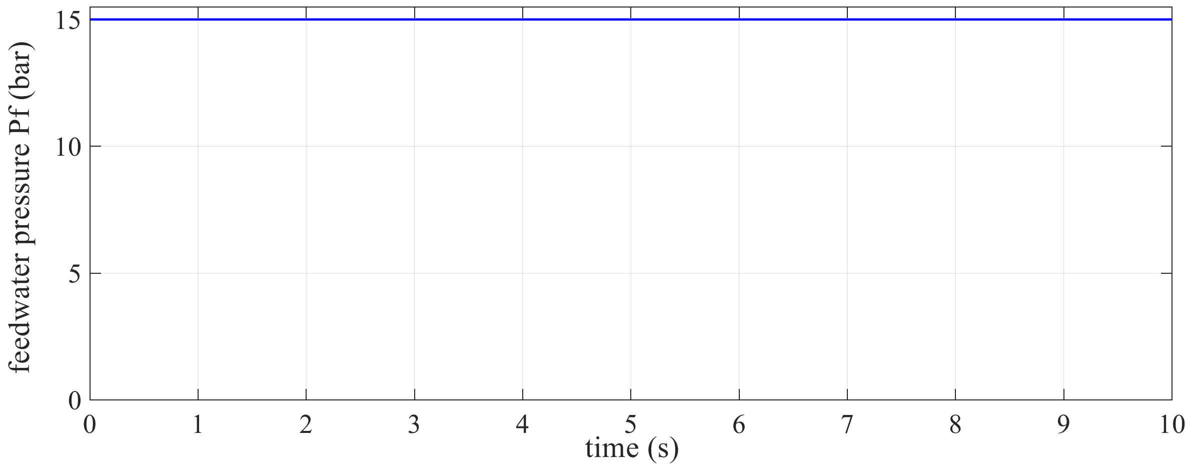

Figure 5.7: Experimental curves of the freshwater pressure.

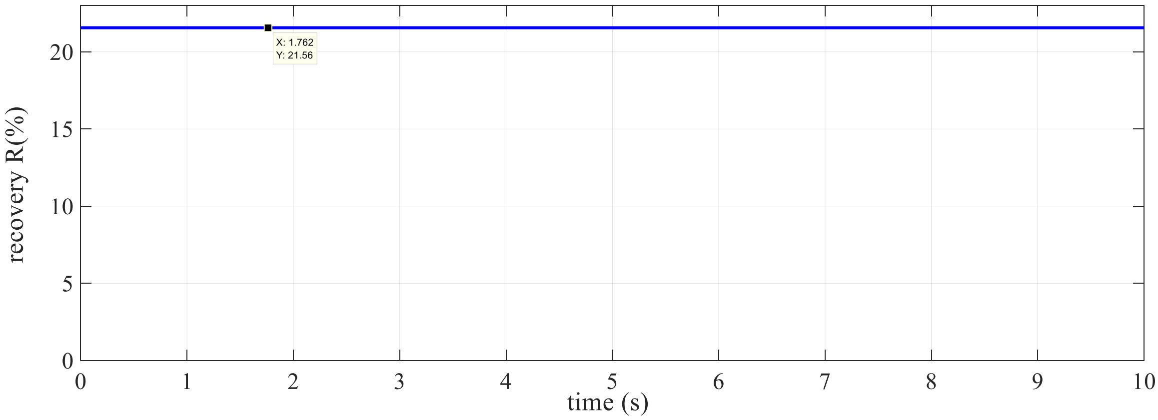

Figure 5.8: Experimental curves of the recovery.

Figures (5.9) illustrate the current pattern of the GPV with its reference (around 1.5 A).

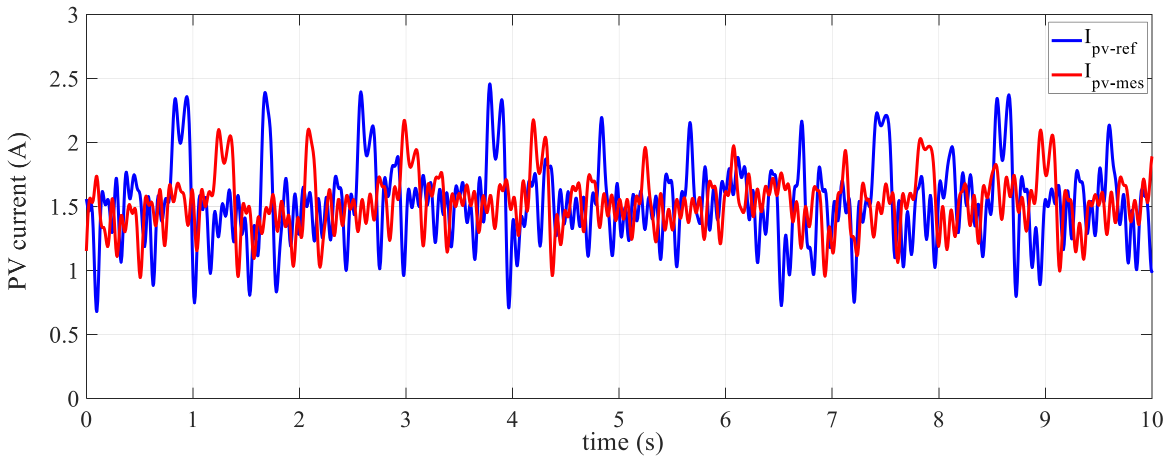

Figure 5.9: Experimental curves of the PV generator current and its reference.

Figure (5.10) shows the experimental curves of the measured DC bus voltage and its reference. It is evident that the DC bus voltage remains constant at its reference value of 250V, with small chattering around this value.

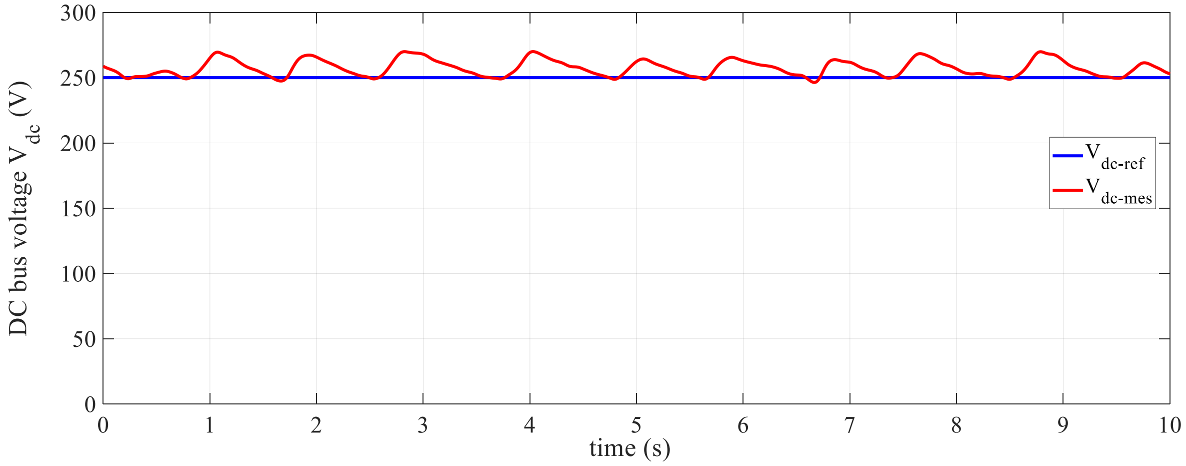

Figure 5.10: Experimental curves of the DC bus voltage measured and its reference.

Figure (5.11) shows the curves of the measured speed and its reference, which was obtained using the Linear Quadratic Regulator (LQR). The zoomed-in section of this figure reveals that the measured speed oscillates within a band of 5 rad/s (+2.5 and -2.5rad/s) around the reference value of 140 rad/s.

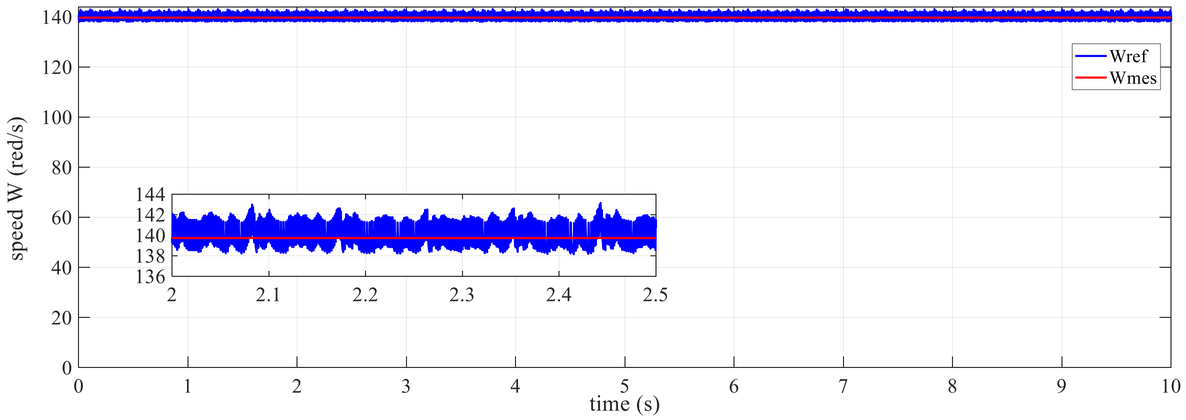

Figure 5.11: Measured speed curve and its reference with zoom.

Figure (5.12) depicts the experimental curves of the stator current Isa, Isb, and Isc, along with their zoomed. The stator current waveform is practically sinusoidal, with a maximum value of 0.5 A.

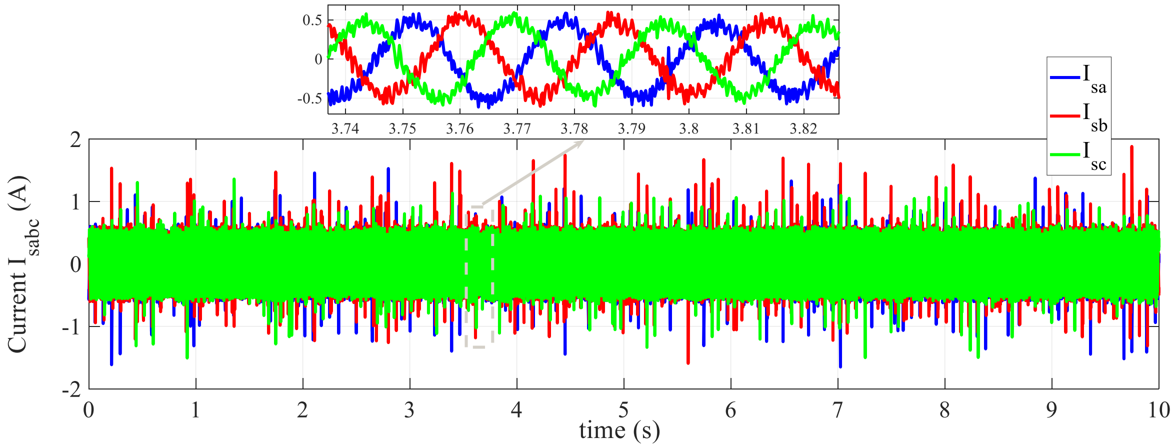

Figure 5.12: Stator current Isa, Isb, and Isc with zoom.

Figure (5.13) displays the magnitude of the estimate stator flux, which follows its reference value of 0.8 Wb. Furthermore, the employed DTC control mechanism provides excellent torque tracking, as depicted in Figure (5.14). It is clear that both the electromagnetic and resistance torque have the same value of 0.8 N.m. Figure (5.15) demonstrates the excellent tracking of the two torque values, Ap and Kmcc.

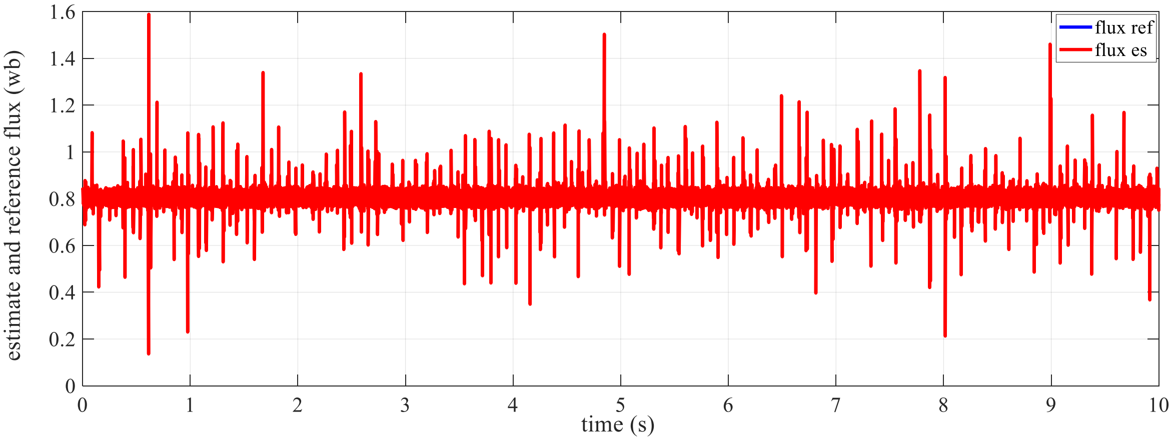

Figure 5.13: Estimated stator flux magnitude and its reference.

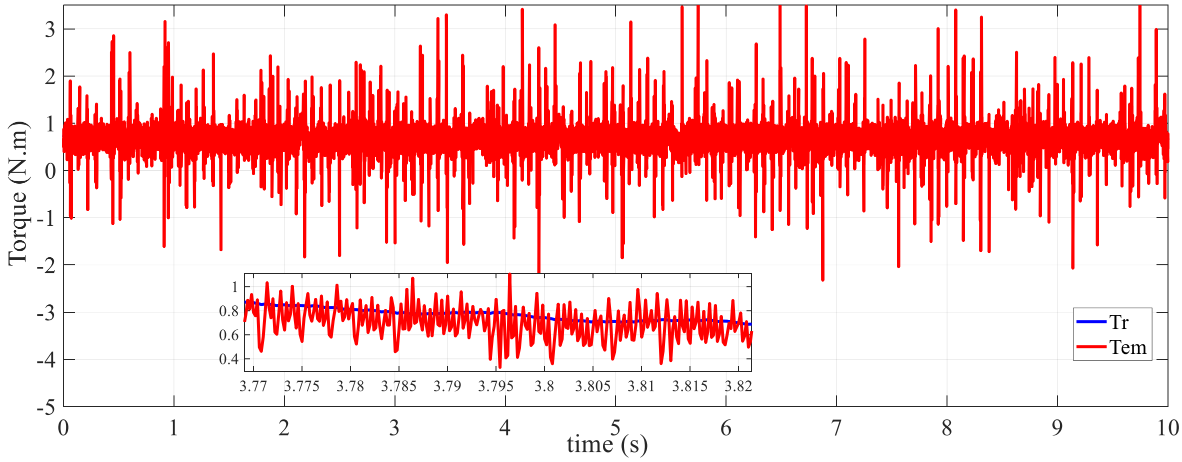

Figure 5.14: Electromagnetic and resistance torque with their zoom.

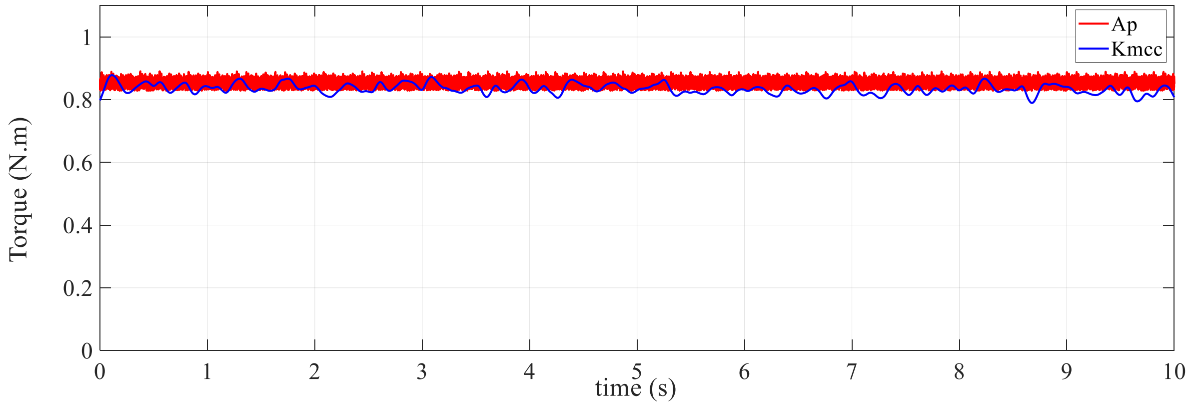

Figure 5.15: Experimental curves of the pump torques.

5.4.2. Case two:

After having seen the hydraulic production obtained by our prototype in fixed conditions, this test is a continuation to observe the influence of the sudden variation in Qp (freshwater flow). Figures (5.16), (5.17), (5.18), and (5.19) represent hydraulic quantities: permeate concentration Cp in mg/l, freshwater pressure Pf in bar, freshwater flow Qp in l/min, and recovery R in %, respectively. The freshwater concentration is maintained at a constant level of 6mg/l throughout the test. When the freshwater flow rate is 1.1 l/min and the freshwater pressure is 13.4 bar, the recovery rate is 23%. Decreases in freshwater flow cause corresponding decreases in both freshwater pressure and recovery rate. The freshwater flow variation takes 4 seconds to stabilize at 0.8 l/min, while the freshwater pressure stabilizes at 10 bar in just 2s.

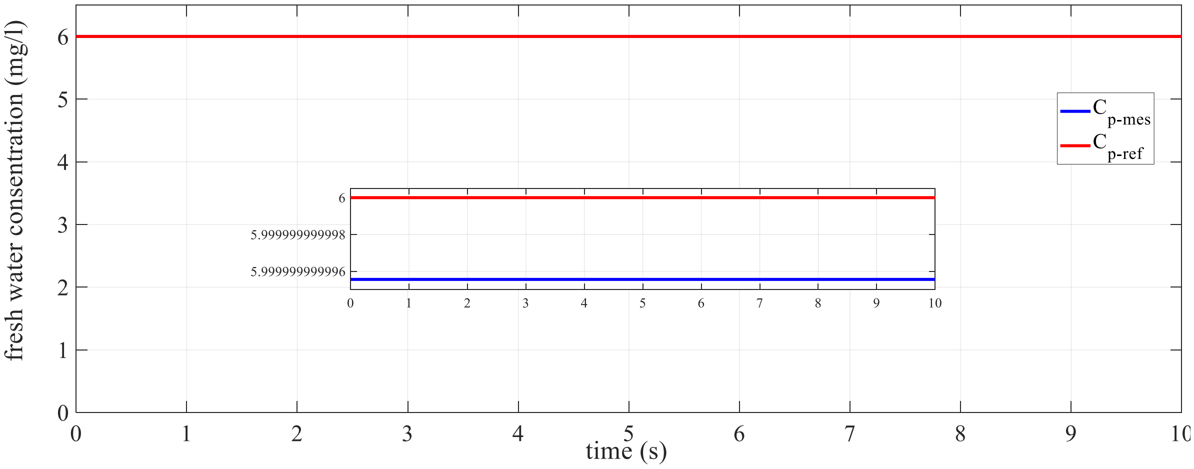

Figure 5.16: Experimental curves of the freshwater concentration and its reference with zoom.

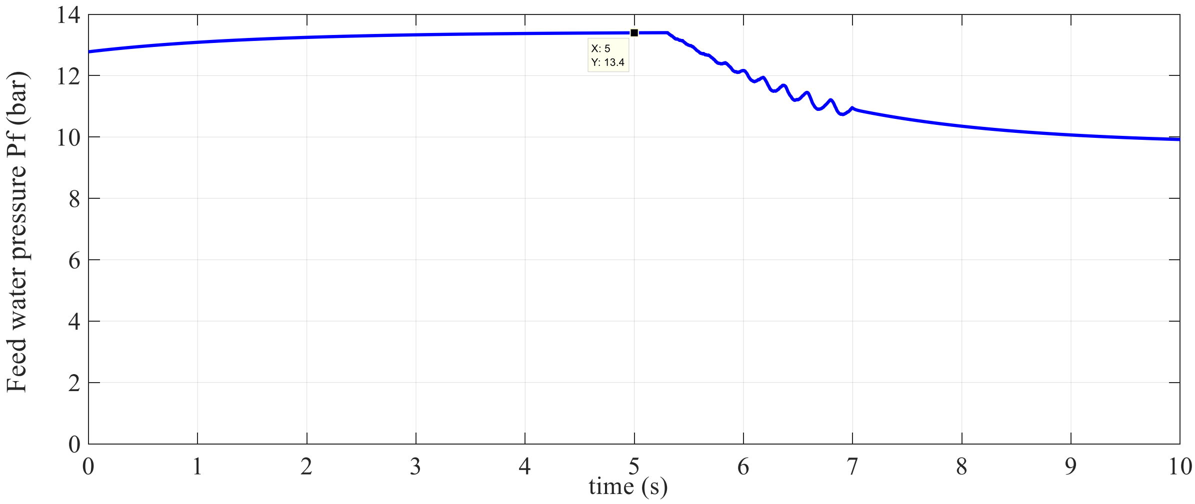

Figure 5.17: Experimental curves of the freshwater pressure.

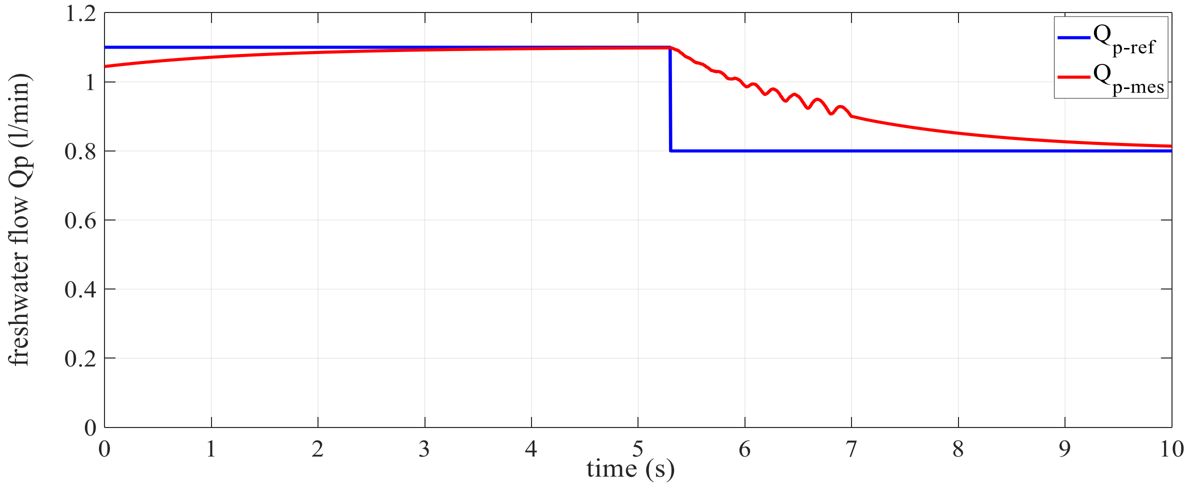

Figure 5.18: Experimental curves of the freshwater pressure.

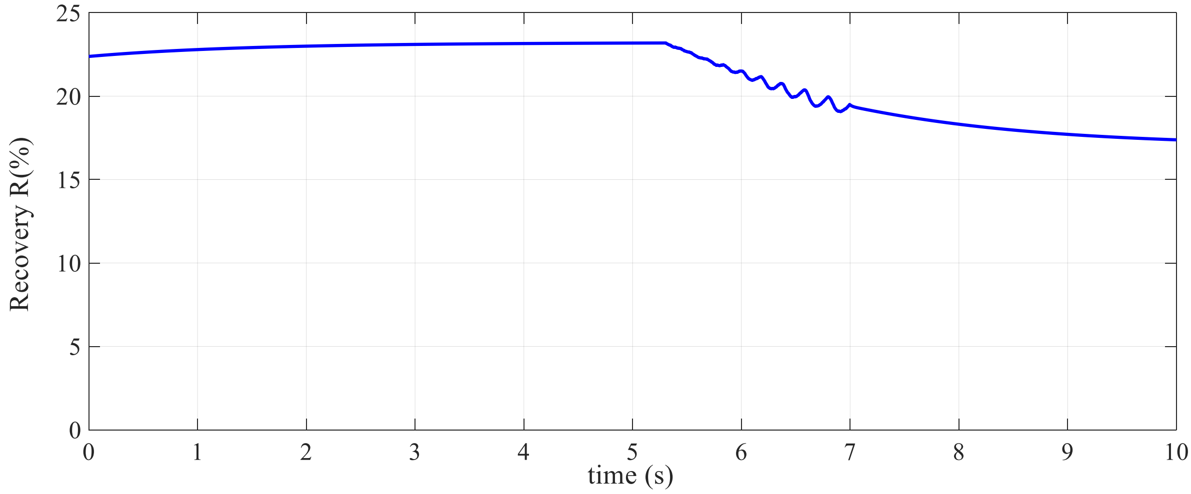

Figure 5.19: Experimental curves of the recovery.

Figures (5.20) and (5.21) display the waveforms of PV current and DC bus voltage, respectively, along with their references. It is clear that the variation in freshwater flow did not have any impact on either the PV current or the DC bus voltage.

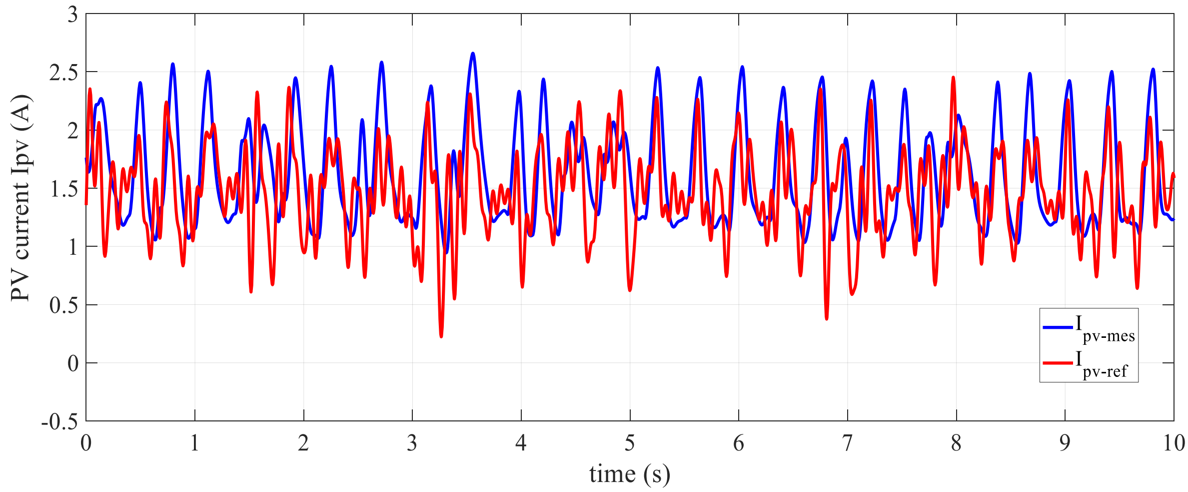

Figure 5.20: PV current waveform and its reference.

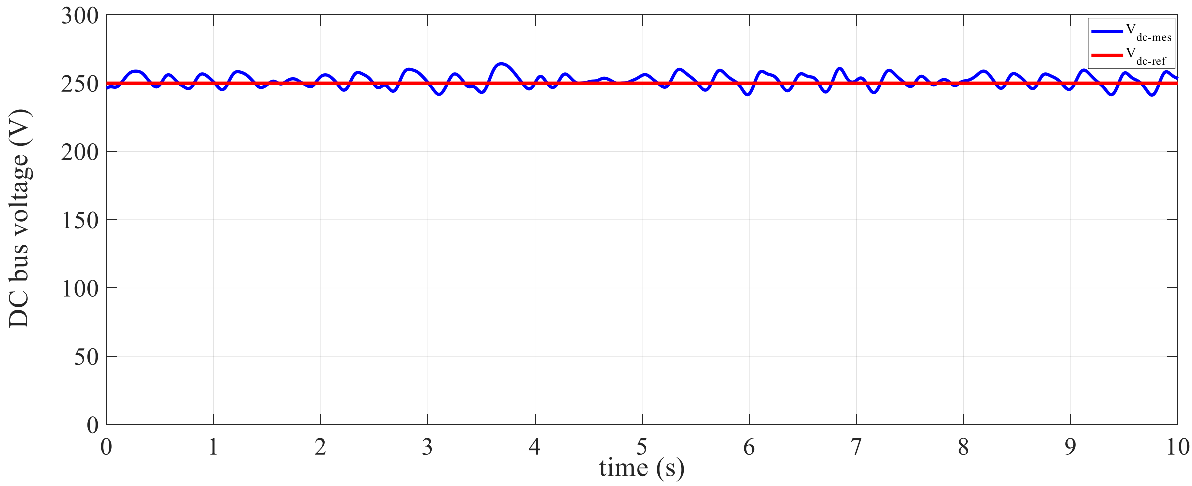

Figure 5.21: DC bus voltage waveform and its reference.

On the other hand, the proposed control scheme utilizing DTC proves high dynamic and static performances for IM drive. However, it produces relatively large flux ripples (figure (5.23)) due to the harmonics present in the stator currents, as shown in Figure (5.22).

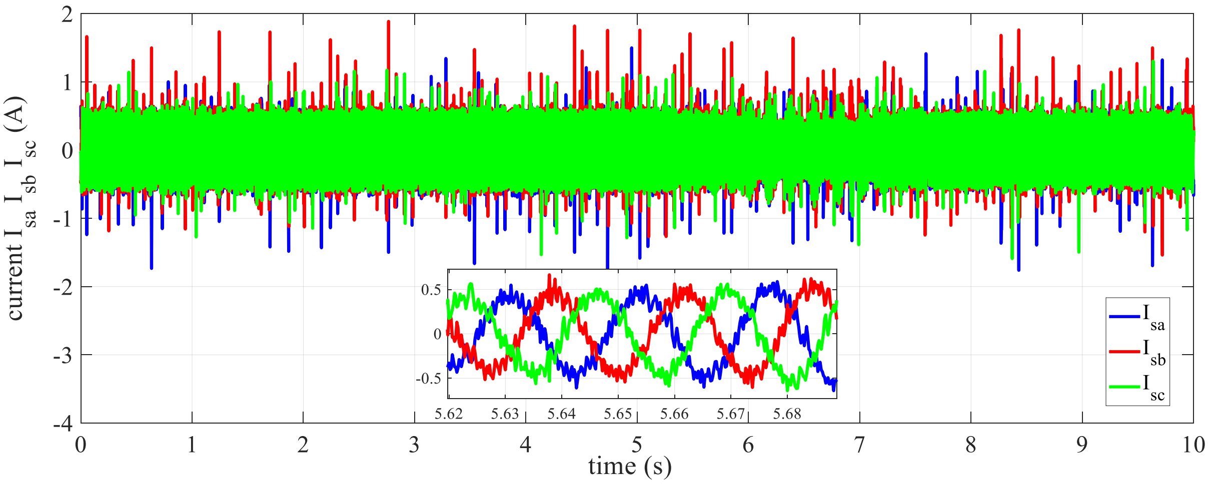

Figure 5.22: Stator currents with zoom waveforms.

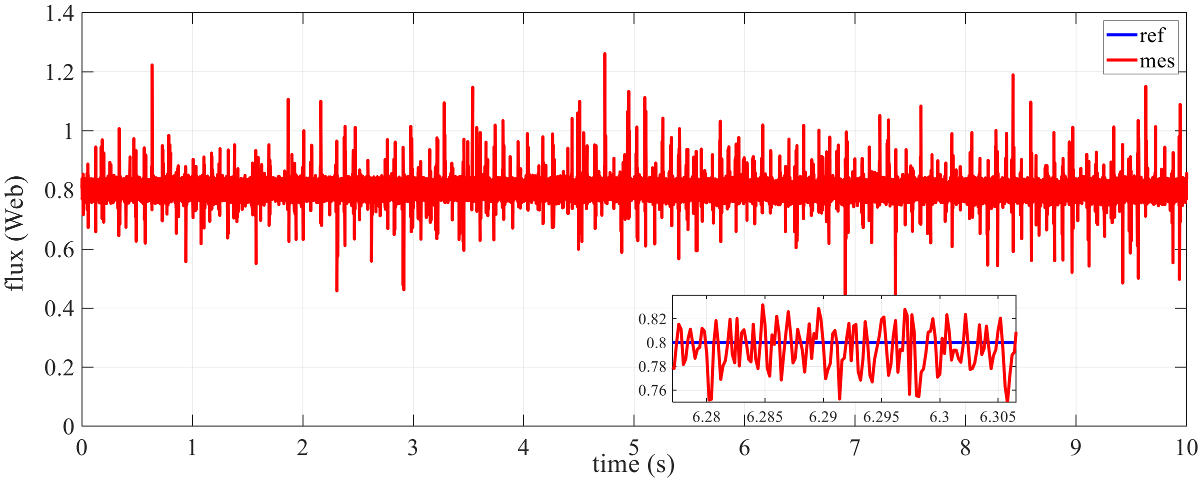

Figure 5.23: Stator flux magnitude and its reference.

Regardless of the variation, the two torques of the pump follow each other. These torques exhibit a response time of 2 seconds to the variation, as shown in figure (5.24). It is clear that the torques decrease from 0.75 N.m to 0.6 N.m.

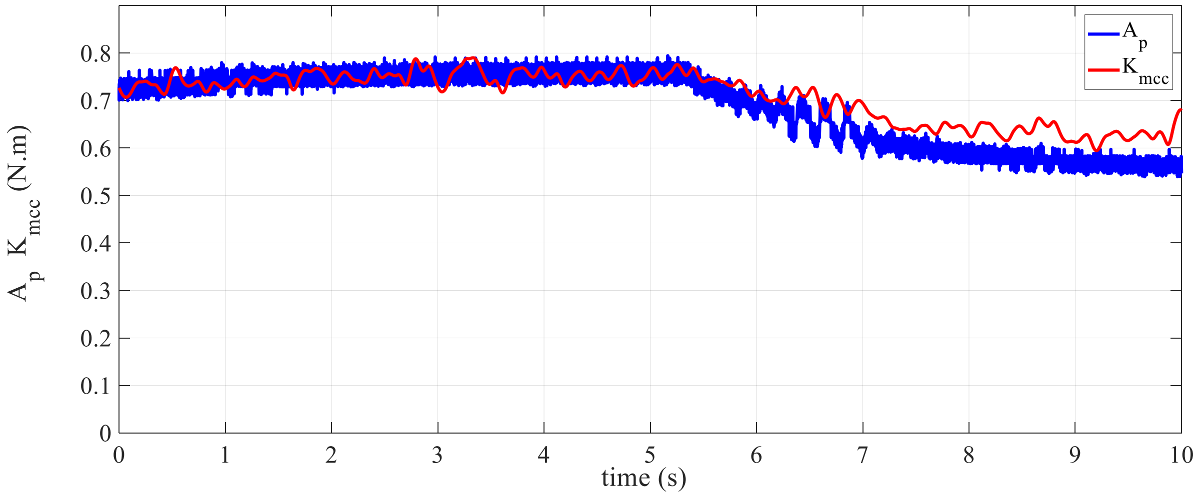

Figure 5.24: Experimental curves of the pump torques.

The figures below depict the results obtained when a load torque (pump) was introduced after a variation in the hydraulic magnitude (Qp) at time t=5.4s. The resisting torque follows the electromagnetic torque with an overshot of 0.5 N.m due to the influence of induction machine friction, as shown in figure (5.28). Figure (5.29) illustrates the speed evolution following these conditions. The speed decreases from 130 rad/s to 115 rad/s with a response time of 1.6 s.

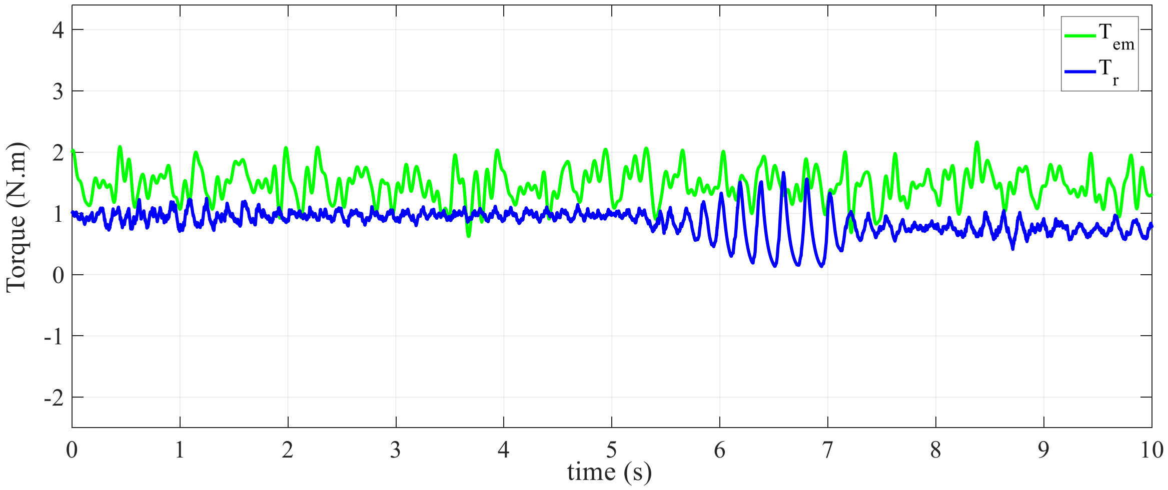

Figure 5.28: Electromagnetic and resistance torque waveforms.

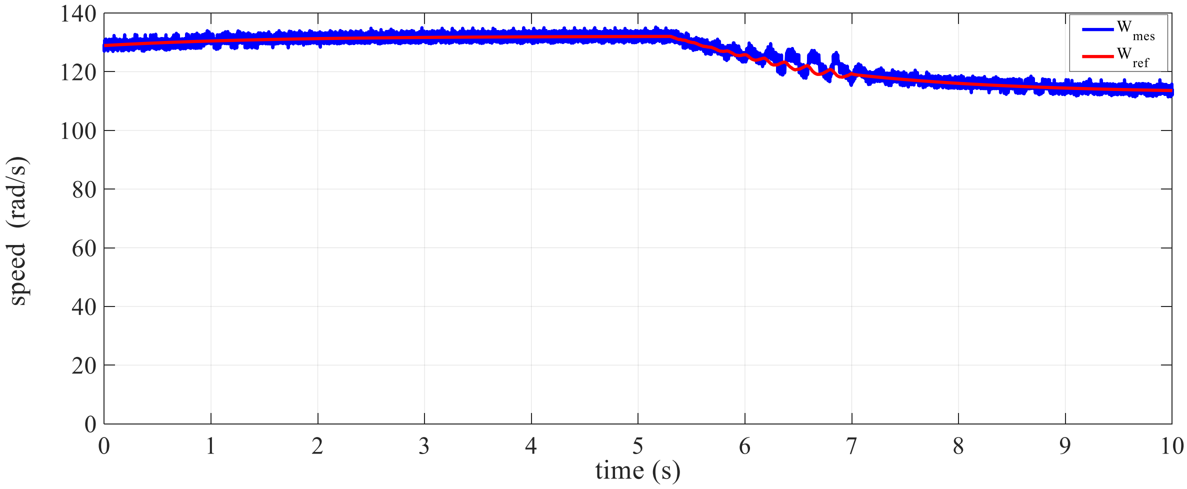

Figure 5.29: Measured speed and its reference curves.

5.5. Conclusion:

Based on the experimental results of the freshwater flow variation effect on a motor pump fed with a PV generator and connected with an RO desalination system, it can be concluded that the integrated system provides a promising solution for off-grid, sustainable freshwater production.

The experiments showed that the motor pump's output power increased with an increase in freshwater flow rate, which resulted in a higher pumping rate and increased production of freshwater by the RO desalination system. The use of a PV generator as a power source for the motor pump and the RO desalination system was found to be highly effective, providing reliable and efficient power.

Additionally, the results suggest that the integrated system could be a practical and sustainable solution for freshwater production in remote areas with limited access to freshwater sources.

CONCLUSION
GENERALE
ET PERSPECTIVES

General Conclusion and perspectives

This work was carried out with funding from the Algerian General Direction of Research (DGRSDT) under grant no A01L07UN0701201180014. Its aim to investigate and improve the performance of a water desalination system powered by a photovoltaic source. The study employs experimental and simulation techniques to evaluate the system's performance and develop strategies to enhance its efficiency.

The findings of the study suggest several methods to improve the performance of the water desalination system. One way is to enhance the photovoltaic source's efficiency by using MPPT, which would increase the energy available for the desalination process. Another promising approach is to integrate Direct Torque Control (DTC) with an induction machine into Photovoltaic-Reverse Osmosis (PV-RO) desalination systems. This integration leads to significant improvements in the system's energy efficiency, resulting in lower operating costs and a reduced environmental impact. Finally, optimizing and controlling the operating conditions of the system, such as the flow rate, would also increase efficiency.

The results also show that the use of renewable energy sources, such as photovoltaic sources, is a promising approach to reducing the energy consumption and environmental impact of the desalination process.

In conclusion, this work provides valuable insights into the performance of water desalination systems powered by photovoltaic sources and offers practical solutions to improve their efficiency. The study contributes to the development of sustainable and environmentally friendly water desalination technologies, which are crucial for addressing the increasing demand for clean water worldwide.

Perspectives:

The entirety of these works has incited us to propose perspectives that can contribute to the improvement of the PV-RO desalination system chain. Among these perspectives, we consider:

- Explore the effects and reliability of implementing additional artificial intelligence techniques on the desalination system, and compare the results.
- Enhance hydraulic production by adding multiple sources and implementing effective management strategies.

REFERENCES BIBLIOGRAPHIQUES

References

[1] J. Rigali, J. E. Miller, S. J. Altman, L. Biedermann, P. V. Brady, M. M. Hightower, S. P. Kuzio, T. M. Nenoff, and S. Rempe, "Desalination and water treatment research at Sandia national laboratories," *Sandia report,* 2016.

[2] E. Borgomeo, A. Jagerskog, A. Talbi, M. Wijnen, M. Hejazi, and F. Miralles-Wilhelm, "The Water-Energy-Food Nexus in the Middle East and North Africa," 2018.

[3] M. Elimelech and W. A. Phillip, "The future of seawater desalination: energy, technology, and the environment," *science,* vol. 333, pp. 712-717, 2011.

[4] M. T. Ali, H. E. Fath, and P. R. Armstrong, "A comprehensive techno-economical review of indirect solar desalination," *Renewable and Sustainable Energy Reviews,* vol. 15, pp. 4187-4199, 2011.

[5] B. D. Richter, D. Abell, E. Bacha, K. Brauman, S. Calos, A. Cohn, C. Disla, S. F. O'Brien, D. Hodges, and S. Kaiser, "Tapped out: how can cities secure their water future?," *Water Policy,* vol. 15, pp. 335-363, 2013.

[6] M. Sepehr, S. Fatemi, A. Danehkar, and A. M. Moradi, "Application of Delphi method in site selection of desalination plants," *Global Journal of Environmental Science and Management,* vol. 3, p. 89, 2017.

[7] M. Nair and D. Kumar, "Water desalination and challenges: The Middle East perspective: a review," *Desalination and Water Treatment,* vol. 51, pp. 2030-2040, 2013.

[8] S. J. Judd, "Membrane technology costs and me," *Water research,* vol. 122, pp. 1-9, 2017.

[9] J. Nriagu, F. Darroudi, and B. Shomar, "Health effects of desalinated water: Role of electrolyte disturbance in cancer development," *Environmental research,* vol. 150, pp. 191-204, 2016.

[10] W. He and J. Wang, "Feasibility study of energy storage by concentrating/desalinating water: Concentrated Water Energy Storage," *Applied energy,* vol. 185, pp. 872-884, 2017.

[11] H. Frank, E. Rahav, and E. Bar-Zeev, "Short-term effects of SWRO desalination brine on benthic heterotrophic microbial communities," *Desalination,* vol. 417, pp. 52-59, 2017.

[12] E. DeNicola, O. S. Aburizaiza, A. Siddique, H. Khwaja, and D. O. Carpenter, "Climate change and water scarcity: The case of Saudi Arabia," *Annals of global health,* vol. 81, pp. 342-353, 2015.

[13] O. Rabinowitz, "Nuclear energy and desalination in Israel," *Bulletin of the Atomic Scientists,* vol. 72, pp. 32-38, 2016.

[14] A. Blanco-Marigorta, A. Lozano-Medina, and J. Marcos, "The exergetic efficiency as a performance evaluation tool in reverse osmosis desalination plants in operation," *Desalination,* vol. 413, pp. 19-28, 2017.

[15] M. H. Sellami, H. Bouguettaia, D. Bechki, M. Zeroual, S. Kachi, S. Boughali, B. Bouchekima, and H. Mahcene, "Effect of absorber coating on the performance of a solar still in the region of Ouargla (Algeria)," *Desalination and Water Treatment,* vol. 51, pp. 6490-6497, 2013.

[16] D. Bechki, H. Bouguettaia, J. Blanco-Galvez, S. Babay, B. Bouchekima, S. Boughali, and H. Mahcene, "Effect of partial intermittent shading on the performance of a simple basin solar still in south Algeria," *Desalination,* vol. 260, pp. 65-69, 2010.

[17] N. Ghemmit-Doulache and N. Ouslimani, "WATER QUALITY CONTROL OF THREE SITES AT KEDARRA BARRAGE," *Journal of Fundamental and Applied Sciences,* vol. 13, pp. 965-981, 2021.

[18] A. M. Hamiche, A. B. Stambouli, S. Flazi, and A. Tayeb, "Desalination in Algeria: Photovoltaic Power Plant for TMM (Tahlyat Myah Magtaa) of Oran as a Case Study," *Water Resources in Algeria-Part II: Water Quality, Treatment, Protection and Development,* pp. 285-315, 2020.

[19] P. Xu, T. Y. Cath, A. P. Robertson, M. Reinhard, J. O. Leckie, and J. E. Drewes, "Critical review of desalination concentrate management, treatment and beneficial use," *Environmental Engineering Science,* vol. 30, pp. 502-514, 2013.

[20] H. B. Harandi, M. Rahnama, E. J. Javaran, and A. Asadi, "Performance optimization of a multi stage flash desalination unit with thermal vapor compression using genetic algorithm," *Applied Thermal Engineering,* vol. 123, pp. 1106-1119, 2017.

[21] V. Eveloy, P. Rodgers, and L. Qiu, "Hybrid gas turbine–organic Rankine cycle for seawater desalination by reverse osmosis in a hydrocarbon production facility," *Energy Conversion and Management,* vol. 106, pp. 1134-1148, 2015.

[22] S. Jiang, Y. Li, and B. P. Ladewig, "A review of reverse osmosis membrane fouling and control strategies," *Science of the Total Environment,* vol. 595, pp. 567-583, 2017.

[23] J. Kämpf and B. Clarke, "How robust is the environmental impact assessment process in South Australia? Behind the scenes of the Adelaide seawater desalination project," *Marine Policy,* vol. 38, pp. 500-506, 2013.

[24] A. D. Khawaji, I. K. Kutubkhanah, and J.-M. Wie, "Advances in seawater desalination technologies," *Desalination,* vol. 221, pp. 47-69, 2008.

[25] B. A. Kamaluddin, S. Khan, and B. M. Ahmed, "Selection of optimally matched cogeneration plants," *Desalination,* vol. 93, pp. 311-321, 1993.

[26] A. M. El-Nashar, "Cogeneration for power and desalination—state of the art review," *Desalination,* vol. 134, pp. 7-28, 2001.

[27] M. Al-Shammiri and M. Safar, "Multi-effect distillation plants: state of the art," *Desalination,* vol. 126, pp. 45-59, 1999.

[28] A. Ophir and F. Lokiec, "Advanced MED process for most economical sea water desalination," *Desalination,* vol. 182, pp. 187-198, 2005.

[29] T. Michels, "Recent achievements of low temperature multiple effect desalination in the western areas of Abu Dhabi. UAE," *Desalination,* vol. 93, pp. 111-118, 1993.

[30] R. Saidur, E. Elcevvadi, S. Mekhilef, A. Safari, and H. A. Mohammed, "An overview of different distillation methods for small scale applications," *Renewable and Sustainable Energy Reviews,* vol. 15, pp. 4756-4764, 2011.

[31] K. El-Khatib, A. Abd El-Hamid, A. Eissa, and M. Khedr, "Transient model, simulation and control of a single-effect mechanical vapour compression (SEMVC) desalination system," *Desalination,* vol. 166, pp. 157-165, 2004.

[32] A. Porteous, *Desalination technology: developments and practice*: Applied Science Publishers, 1983.

[33] O. Hamed, A. Zamamiri, S. Aly, and N. Lior, "Thermal performance and exergy analysis of a thermal vapor compression desalination system," *Energy Conversion and Management,* vol. 37, pp. 379-387, 1996.

[34] M. Lucas and S. Hessemans, "Advantages of the ejectocompression process in sea water desalination," *Desalination,* vol. 38, pp. 57-63, 1981.

[35] P.-K. Park, S. Lee, J.-S. Cho, and J.-H. Kim, "Full-scale simulation of seawater reverse osmosis desalination processes for boron removal: Effect of membrane fouling," *Water research,* vol. 46, pp. 3796-3804, 2012.

[36] A. Malek, M. Hawlader, and J. Ho, "Design and economics of RO seawater desalination," *Desalination,* vol. 105, pp. 245-261, 1996.

[37] P. Goh, W. Lau, M. Othman, and A. Ismail, "Membrane fouling in desalination and its mitigation strategies," *Desalination,* vol. 425, pp. 130-155, 2018.

[38] S. Burn and S. Gray, *Efficient Desalination by Reverse Osmosis: A guide to RO practice*: IWA publishing London, UK, 2016.

[39] T. Y. Cath, A. E. Childress, and M. Elimelech, "Forward osmosis: principles, applications, and recent developments," *Journal of membrane science,* vol. 281, pp. 70-87, 2006.

[40] J. P. Chen, E. S. Chian, P.-X. Sheng, K. N. Nanayakkara, L. K. Wang, and Y.-P. Ting, "Desalination of seawater by reverse osmosis," in *Membrane and Desalination Technologies*, ed: Springer, 2011, pp. 559-601.

[41] P. Pal, J. Sikder, S. Roy, and L. Giorno, "Process intensification in lactic acid production: A review of membrane based processes," *Chemical Engineering and Processing: Process Intensification,* vol. 48, pp. 1549-1559, 2009.

[42] S. S. Hosseini, J. A. Dehkordi, and P. K. Kundu, "Gas permeation and separation in asymmetric hollow fiber membrane permeators: mathematical modeling, sensitivity analysis and optimization," *Korean Journal of Chemical Engineering,* vol. 33, pp. 3085-3101, 2016.

[43] T. Melin and R. Rautenbach, *Membranverfahren: Grundlagen der Modul-und Anlagenauslegung*: Springer-Verlag, 2007.

[44] H. Strathmann, "Electrodialytic membrane processes and their practical application," in *Studies in Environmental Science*. vol. 59, ed: Elsevier, 1994, pp. 495-533.

[45] A. Menadi, "Commande Par Les Techniques Intelligentes D'un Système Photovoltaïque Connecté Au Réseau," UNIVERSITE MOHAMED KHIDER BISKRA, 2016.

[46] N. Ghaffour, J. Bundschuh, H. Mahmoudi, and M. F. Goosen, "Renewable energy-driven desalination technologies: A comprehensive review on challenges and potential applications of integrated systems," *Desalination,* vol. 356, pp. 94-114, 2015.

[47] P. Byrne, L. Fournaison, A. Delahaye, Y. A. Oumeziane, L. Serres, P. Loulergue, A. Szymczyk, D. Mugnier, J.-L. Malaval, and R. Bourdais, "A review on the coupling of cooling, desalination and solar photovoltaic systems," *Renewable and Sustainable Energy Reviews,* vol. 47, pp. 703-717, 2015.

[48] E. Delyannis, "Historic background of desalination and renewable energies," *Solar Energy,* vol. 75, pp. 357-366, 2003.

[49] S. Gato, "Forecasting urban residential water demand," *School of Civil, Environmental and Chemical Engineering,* 2006.

[50] A. AMMAR, "Improvement of Direct Torque Control Performances

for Asynchronous Machine Using Non-Linear

Techniques," 2017.

[51] E. Muljadi, C. Butterfield, J. Chacon, and H. Romanowitz, "Power quality aspects in a wind power plant," in *2006 IEEE Power Engineering Society General Meeting*, 2006, p. 8 pp.

[52] A. Efraty, "Hydraulic wind farms for grid electricity and desalination," ed: Google Patents, 2014.

[53] A. E. Al-Rawajfeh, S. Jaber, and H. Etawi, "Desalination by renewable energy: A mini review of the recent patents," *Hemijska industrija,* vol. 71, pp. 451-460, 2017.

[54] A. Sarria, "Deep sea thermal energy mining," ed: Google Patents, 2015.

[55] A. Z. Al-Garni and W. G. Abdelrahman, "Water desalination system using geothermal energy," ed: Google Patents, 2016.

[56] V. G. Gude, N. Nirmalakhandan, and S. Deng, "Renewable and sustainable approaches for desalination," *Renewable and Sustainable Energy Reviews,* vol. 14, pp. 2641-2654, 2010.

[57] M. F. Goosen, H. Mahmoudi, and N. Ghaffour, "Today's and future challenges in applications of renewable energy technologies for desalination," *Critical Reviews in Environmental Science and Technology,* vol. 44, pp. 929-999, 2014.

[58] M. A. Khan, S. Rehman, and F. A. Al-Sulaiman, "A hybrid renewable energy system as a potential energy source for water desalination using reverse osmosis: A review," *Renewable and Sustainable Energy Reviews,* vol. 97, pp. 456-477, 2018.

[59] T. Espino, B. Peñate, G. Piernavieja, D. Herold, and A. Neskakis, "Optimised desalination of seawater by a PV powered reverse osmosis plant for a decentralised coastal water supply," *Desalination,* vol. 156, pp. 349-350, 2003.

[60] M. M. Mahmoud and I. H. Ibrik, "Techno-economic feasibility of energy supply of remote villages in Palestine by PV-systems, diesel generators and electric grid," *Renewable and Sustainable Energy Reviews,* vol. 10, pp. 128-138, 2006.

[61] S. A. Kalogirou, "Seawater desalination using renewable energy sources," *Progress in energy and combustion science,* vol. 31, pp. 242-281, 2005.

[62] E. Mathioulakis, V. Belessiotis, and E. Delyannis, "Desalination by using alternative energy: Review and state-of-the-art," *Desalination,* vol. 203, pp. 346-365, 2007.

[63] J. F. Sklarew and D. M. Sklarew, "Empowering Resilience in Energy and Water Systems: Addressing Barriers to Implementation of Urban Hydroelectric Micro-turbines," *The CIP Report,* 2017.

[64] C. Sommariva, "State of the art and future applications of desalination technologies in the Middle East," *Water, energy & food sustainability in the Middle East,* pp. 107-124, 2017.

[65] T. Tezer, R. Yaman, and G. Yaman, "Evaluation of approaches used for optimization of stand-alone hybrid renewable energy systems," *Renewable and Sustainable Energy Reviews,* vol. 73, pp. 840-853, 2017.

[66] K. Bourouni, T. B. M'Barek, and A. Al Taee, "Design and optimization of desalination reverse osmosis plants driven by renewable energies using genetic algorithms," *Renewable energy,* vol. 36, pp. 936-950, 2011.

[67] B. Yang, J. Wang, X. Zhang, T. Yu, W. Yao, H. Shu, F. Zeng, and L. Sun, "Comprehensive overview of meta-heuristic algorithm applications on PV cell parameter identification," *Energy Conversion and Management,* vol. 208, p. 112595, 2020.

[68] S. Chander, A. Purohit, A. Sharma, S. Nehra, and M. Dhaka, "Impact of temperature on performance of series and parallel connected mono-crystalline silicon solar cells," *Energy Reports,* vol. 1, pp. 175-180, 2015.

[69] K. Masuko, M. Shigematsu, T. Hashiguchi, D. Fujishima, M. Kai, N. Yoshimura, T. Yamaguchi, Y. Ichihashi, T. Mishima, and N. Matsubara, "Achievement of more than 25% conversion efficiency with crystalline silicon heterojunction solar cell," *IEEE Journal of Photovoltaics,* vol. 4, pp. 1433-1435, 2014.

[70] D. Micheli, S. Alessandrini, R. Radu, and I. Casula, "Analysis of the outdoor performance and efficiency of two grid connected photovoltaic systems in northern Italy," *Energy Conversion and Management,* vol. 80, pp. 436-445, 2014.

[71] F. Schindler, A. Fell, R. Müller, J. Benick, A. Richter, F. Feldmann, P. Krenckel, S. Riepe, M. C. Schubert, and S. W. Glunz, "Towards the efficiency limits of multicrystalline silicon solar cells," *Solar Energy Materials and Solar Cells,* vol. 185, pp. 198-204, 2018.

[72] B. Tripathi, P. Yadav, S. Rathod, and M. Kumar, "Performance analysis and comparison of two silicon material based photovoltaic technologies under actual climatic conditions in Western India," *Energy Conversion and Management,* vol. 80, pp. 97-102, 2014.

[73] A. Tihane, M. Boulaid, A. Elfanaoui, M. Nya, and A. Ihlal, "Performance analysis of mono and poly-crystalline silicon photovoltaic modules under Agadir climatic conditions in Morocco," *Materials Today: Proceedings,* vol. 24, pp. 85-90, 2020.

[74] M. Imamzai, M. Aghaei, Y. H. M. Thayoob, and M. Forouzanfar, "A review on comparison between traditional silicon solar cells and thin-film CdTe solar cells," in *Proceedings of National Graduate Conference (Nat-Grad*, 2012, pp. 1-5.

[75] B. K. Dey, I. Khan, N. Mandal, and A. Bhattacharjee, "Mathematical modelling and characteristic analysis of Solar PV Cell," in *2016 IEEE 7th Annual Information Technology, Electronics and Mobile Communication Conference (IEMCON)*, 2016, pp. 1-5.

[76] A. I. Ali, M. A. Sayed, and E. E. Mohamed, "Modified efficient perturb and observe maximum power point tracking technique for grid-tied PV system," *International Journal of Electrical Power & Energy Systems,* vol. 99, pp. 192-202, 2018.

[77] F. L. Luo and H. Ye, *Advanced dc/dc converters*: crc Press, 2016.

[78] A. Lashab, D. Sera, J. M. Guerrero, L. Mathe, and A. Bouzid, "Discrete model-predictive-control-based maximum power point tracking for PV systems: Overview and evaluation," *IEEE Transactions on Power Electronics,* vol. 33, pp. 7273-7287, 2017.

[79] Y. Pankow, "Etude de l'intégration de la production décentralisée dans un réseau basse tension. Application au générateur photovoltaïque," *National School Superior of Art and Trades, Lille,* 2004.

[80] P. Vas, *Electrical machines and drives: a space-vector theory approach* vol. 1: Clarendon press Oxford, 1992.

[81] L. Baghli, *Modélisation et commande de la machine asynchrone*: Les Éditions du Net, 2015.

[82] N. Abu-Tabak, "Stabilité dynamique des systèmes électriques multimachines: modélisation, commande, observation et simulation," Ecole Centrale de Lyon, 2008.

[83] F. Giri, *AC electric motors control: advanced design techniques and applications*: John Wiley & Sons, 2013.

[84] M. ATIG, "Différentes structures mras pour l'estimation de la vitesse du moteur asynchrone," Université Mohamed Boudiaf des Sciences et de la Technologie-Mohamed Boudiaf …, 2011.

[85] O. Messouci, "Commande sans capteur d'un machine asynchrone a cage: application sur la plateforme temps réel NI CompactRIO cRIO 9022," 2015.

[86] M. Turki, J. Belhadj, and X. Roboam, "Control strategy of an autonomous desalination unit fed by PV-wind hybrid system without battery storage," *Journal of Electrical Systems,* vol. 4, pp. 187-200, 2008.

[87] J. G. Wijmans and R. W. Baker, "The solution-diffusion model: a review," *Journal of membrane science,* vol. 107, pp. 1-21, 1995.

[88] R. W. Baker, *Membrane technology and applications*: John Wiley & Sons, 2012.

[89] C. L. Ritt, J. R. Werber, M. Wang, Z. Yang, Y. Zhao, H. J. Kulik, and M. Elimelech, "Ionization behavior of nanoporous polyamide membranes," *Proceedings of the National Academy of Sciences,* vol. 117, pp. 30191-30200, 2020.

[90] Z. M. S. Elbarbary and M. A. Alranini, "Review of maximum power point tracking algorithms of PV system," *Frontiers in Engineering and Built Environment,* 2021.

[91] R. Balraj and A. A. Stonier, "A novel PV array interconnection scheme to extract maximum power based on global shade dispersion using grey wolf optimization algorithm under partial shading conditions," *Circuit World,* 2020.

[92] J. Ahmed and Z. Salam, "An improved perturb and observe (P&O) maximum power point tracking (MPPT) algorithm for higher efficiency," *Applied Energy,* vol. 150, pp. 97-108, 2015.

[93] A. O. Baba, G. Liu, and X. Chen, "Classification and evaluation review of maximum power point tracking methods," *Sustainable Futures,* vol. 2, p. 100020, 2020.

[94] J. P. Ram, T. S. Babu, and N. Rajasekar, "A comprehensive review on solar PV maximum power point tracking techniques," *Renewable and Sustainable Energy Reviews,* vol. 67, pp. 826-847, 2017.

[95] F. Belhachat and C. Larbes, "A review of global maximum power point tracking techniques of photovoltaic system under partial shading conditions," *Renewable and Sustainable Energy Reviews,* vol. 92, pp. 513-553, 2018.

[96] L. L. Jiang, R. Srivatsan, and D. L. Maskell, "Computational intelligence techniques for maximum power point tracking in PV systems: A review," *Renewable and Sustainable Energy Reviews,* vol. 85, pp. 14-45, 2018.

[97] A. Mohapatra, B. Nayak, P. Das, and K. B. Mohanty, "A review on MPPT techniques of PV system under partial shading condition," *Renewable and Sustainable Energy Reviews,* vol. 80, pp. 854-867, 2017.

[98] M. A. Ramli, S. Twaha, K. Ishaque, and Y. A. Al-Turki, "A review on maximum power point tracking for photovoltaic systems with and without shading conditions," *Renewable and Sustainable Energy Reviews,* vol. 67, pp. 144-159, 2017.

[99] B. Yang, L. Zhong, X. Zhang, H. Shu, T. Yu, H. Li, L. Jiang, and L. Sun, "Novel bio-inspired memetic salp swarm algorithm and application to MPPT for PV systems considering partial shading condition," *Journal of cleaner production,* vol. 215, pp. 1203-1222, 2019.

[100] J. Ahmed and Z. Salam, "An enhanced adaptive P&O MPPT for fast and efficient tracking under varying environmental conditions," *IEEE Transactions on sustainable energy,* vol. 9, pp. 1487-1496, 2018.

[101] A. D. Martin, J. R. Vazquez, and J. Cano, "MPPT in PV systems under partial shading conditions using artificial vision," *Electric Power Systems Research,* vol. 162, pp. 89-98, 2018.

[102] D. P. Winston, B. P. Kumar, S. C. Christabel, A. J. Chamkha, and R. Sathyamurthy, "Maximum power extraction in solar renewable power system-a bypass diode scanning approach," *Computers & Electrical Engineering,* vol. 70, pp. 122-136, 2018.

[103] A. Ashouri-Zadeh, M. Toulabi, A. S. Dobakhshari, S. Taghipour-Broujeni, and A. M. Ranjbar, "A novel technique to extract the maximum power of photovoltaic array in partial shading conditions," *International Journal of Electrical Power & Energy Systems,* vol. 101, pp. 500-512, 2018.

[104] V. M. Hoang, N. V. Nguyen, and M. T. Pham, "Extremum Seeking Control based MPPT for photovoltaic array under uniform and non-uniform irradiances," 2016.

[105] H. Li, D. Yang, W. Su, J. Lü, and X. Yu, "An overall distribution particle swarm optimization MPPT algorithm for photovoltaic system under partial shading," *IEEE transactions on industrial electronics,* vol. 66, pp. 265-275, 2018.

[106] K. Kaced, C. Larbes, S. M. Ait-Chikh, M. Bounabi, and Z. E. Dahmane, "FPGA implementation of PSO based MPPT for PV systems under partial shading conditions," in *2017 6th International Conference on Systems and Control (ICSC)*, 2017, pp. 150-155.

[107] Y.-H. Liu, C.-L. Liu, J.-W. Huang, and J.-H. Chen, "Neural-network-based maximum power point tracking methods for photovoltaic systems operating under fast changing environments," *Solar Energy,* vol. 89, pp. 42-53, 2013.

[108] S. Mohanty, B. Subudhi, and P. K. Ray, "A new MPPT design using grey wolf optimization technique for photovoltaic system under partial shading conditions," *IEEE Transactions on sustainable energy,* vol. 7, pp. 181-188, 2015.

[109] Y. Shaiek, M. B. Smida, A. Sakly, and M. F. Mimouni, "Comparison between conventional methods and GA approach for maximum power point tracking of shaded solar PV generators," *Solar Energy,* vol. 90, pp. 107-122, 2013.

[110] O. Bingöl and B. ÖZKAYA, "A comprehensive overview of soft computing based MPPT techniques for partial shading conditions in PV systems," *Mühendislik Bilimleri ve Tasarım Dergisi,* vol. 7, pp. 926-939, 2019.

[111] M. Mao, L. Cui, Q. Zhang, K. Guo, L. Zhou, and H. Huang, "Classification and summarization of solar photovoltaic MPPT techniques: A review based on traditional and intelligent control strategies," *Energy Reports,* vol. 6, pp. 1312-1327, 2020.

[112] Ö. Çelik and A. Teke, "A Hybrid MPPT method for grid connected photovoltaic systems under rapidly changing atmospheric conditions," *Electric Power Systems Research,* vol. 152, pp. 194-210, 2017.

[113] S. Mohanty, B. Subudhi, and P. K. Ray, "A grey wolf-assisted perturb & observe MPPT algorithm for a PV system," *IEEE Transactions on Energy Conversion,* vol. 32, pp. 340-347, 2016.

[114] S. Hanafiah, A. Ayad, A. Hehn, and R. Kennel, "A hybrid MPPT for quasi-Z-source inverters in PV applications under partial shading condition," in *2017 11th IEEE International Conference on Compatibility, Power Electronics and Power Engineering (CPE-POWERENG)*, 2017, pp. 418-423.

[115] K. Sundareswaran and S. Palani, "Application of a combined particle swarm optimization and perturb and observe method for MPPT in PV systems under partial shading conditions," *Renewable energy,* vol. 75, pp. 308-317, 2015.

[116] K. Lian, J. Jhang, and I. Tian, "A maximum power point tracking method based on perturb-and-observe combined with particle swarm optimization," *IEEE Journal of Photovoltaics,* vol. 4, pp. 626-633, 2014.

[117] M. Makhloufi, M. Khireddine, Y. Abdessemed, and A. Boutarfa, "Maximum power point tracking of a photovoltaic system using a fuzzy logic controller on DC/DC boost converter," *International Journal of Computer Science Issues (IJCSI),* vol. 11, p. 1, 2014.

[118] S. Thakran, J. Singh, R. Garg, and P. Mahajan, "Implementation of P&O algorithm for MPPT in SPV system," in *2018 International Conference on Power Energy, Environment and Intelligent Control (PEEIC)*, 2018, pp. 242-245.

[119] L. Djilali, E. N. Sanchez, and M. Belkheiri, "First and high order sliding mode control of a dfig-based wind turbine," *Electric Power Components and Systems,* vol. 48, pp. 105-116, 2020.

[120] J.-J. E. Slotine, "Sliding controller design for non-linear systems," *International Journal of control,* vol. 40, pp. 421-434, 1984.

[121] D. Menaga and V. Sankaranarayanan, "A novel nonlinear sliding mode controller for a single stage grid-connected photovoltaic system," *ISA transactions,* vol. 107, pp. 329-339, 2020.

[122] R. Pradhan and B. Subudhi, "Double integral sliding mode MPPT control of a photovoltaic system," *IEEE transactions on control systems technology,* vol. 24, pp. 285-292, 2015.

[123] K. B. Ariyur and M. Krstic, *Real-time optimization by extremum-seeking control*: John Wiley & Sons, 2003.

[124] K. J. Astrom and B. Wittenmark, "A survey of adaptive control applications," in *Proceedings of 1995 34th IEEE Conference on Decision and Control*, 1995, pp. 649-654.

[125] M. Krstić, "Performance improvement and limitations in extremum seeking control," *Systems & Control Letters,* vol. 39, pp. 313-326, 2000.

[126] A. Kebir, L. Woodward, and O. Akhrif, "Extremum-seeking control with adaptive excitation: Application to a photovoltaic system," *IEEE transactions on industrial electronics,* vol. 65, pp. 2507-2517, 2017.

[127] A. N. Mahmod Mohammad, M. A. Mohd Radzi, N. Azis, S. Shafie, and M. A. Atiqi Mohd Zainuri, "A Novel Hybrid Approach for Maximizing the Extracted Photovoltaic Power under Complex Partial Shading Conditions," *Sustainability,* vol. 12, p. 5786, 2020.

[128] A. F. Tchouani Njomo, G. Kenne, R. M. Douanla, and L. L. Sonfack, "A modified ESC algorithm for MPPT applied to a photovoltaic system under varying environmental conditions," *International Journal of Photoenergy,* vol. 2020, 2020.

[129] M. S. Shadlu, "Comparison of maximum power point tracking (MPPT) algorithms to control DC-DC converters in photovoltaic systems," *Recent Advances in Electrical & Electronic Engineering (Formerly Recent Patents on Electrical & Electronic Engineering),* vol. 12, pp. 355-367, 2019.

[130] H.-T. Yau, C.-J. Lin, and C.-H. Wu, "Sliding mode extremum seeking control scheme based on PSO for maximum power point tracking in photovoltaic systems," *International Journal of Photoenergy,* vol. 2013, 2013.

[131] L. Hu, F. Xue, Z. Qin, J. Shi, W. Qiao, W. Yang, and T. Yang, "Sliding mode extremum seeking control based on improved invasive weed optimization for MPPT in wind energy conversion system," *Applied energy,* vol. 248, pp. 567-575, 2019.

[132] I. Takahashi and T. Noguchi, "A new quick-response and high-efficiency control strategy of an induction motor," *IEEE Transactions on Industry applications,* pp. 820-827, 1986.

[133] M. Depenbrock, "Direct self-control (DSC) of inverter fed induktion machine," in *1987 IEEE Power Electronics Specialists Conference*, 1987, pp. 632-641.

[134] N. El Ouanjli, A. Derouich, A. El Ghzizal, A. Chebabhi, and M. Taoussi, "A comparative study between FOC and DTC control of the Doubly Fed Induction Motor (DFIM)," in *2017 International Conference on Electrical and Information Technologies (ICEIT)*, 2017, pp. 1-6.

[135] M. V. Kazemi, M. Moradi, and R. V. Kazemi, "Minimization of powers ripple of direct power controlled DFIG by fuzzy controller and improved discrete space vector modulation," *Electric Power Systems Research,* vol. 89, pp. 23-30, 2012.

[136] F. BonnetFrancois, P.-E. Vidal, and M. Pietrzak-David, "Dual direct torque control of doubly fed induction machine," *IEEE transactions on industrial electronics,* vol. 54, pp. 2482-2490, 2007.

[137] J. Beerten, J. Verveckken, and J. Driesen, "Predictive direct torque control for flux and torque ripple reduction," *IEEE transactions on industrial electronics,* vol. 57, pp. 404-412, 2009.

[138] H. REGHIOUI, "Amélioration des performances de la commande directe de couple (DTC) appliquée à une machine asynchrone triphasée," Université Mohamed Khider–Biskra, 2017.

[139] M. Gursoy, G. Zhuo, A. G. Lozowski, and X. Wang, "Photovoltaic energy conversion systems with sliding mode control," *Energies,* vol. 14, p. 6071, 2021.

[140] A. B. Chaaben, R. Andoulsi, A. Sellami, and R. Mhiri, "MIMO modeling approach for a small photovoltaic reverse osmosis desalination system," *Journal of Applied Fluid Mechanics,* vol. 4, pp. 35-41, 2012.

[141] V. Feliu-Batlle, R. Rivas-Perez, and A. Linares-Saez, "Fractional order robust control of a reverse osmosis seawater desalination plant," *IFAC-PapersOnLine,* vol. 50, pp. 14545-14550, 2017.

ANNEXE 01

➢ Monocrystalline photovoltaic module :

Paramètres : (STC)*	
Module efficiency	**13.5%**
Efficiency of the encapsulated cell	**16.4%**
Optimal power P_{op}	**162,0 W**
Short circuit voltage V_{sc}	**44V**
Optimal voltage V_{op}	**36V**
Short circuit curent I_{cc}	**5 A**
Courant à puissance maximale (crête) I_{op}	**4.5 A**
Coefficients de température	
Coefficient de variation du courant de court-circuit en fonction de la température	**+0,053% / °C**
Coefficient de variation de la tension du circuit ouvert en fonction de la température	**-156 mV / °C**

➢ System parameters:

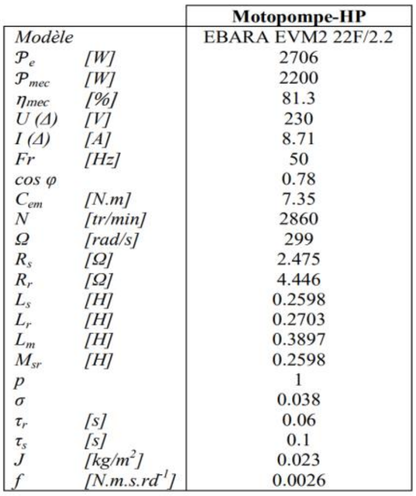

		Motopompe-HP
Modèle		EBARA EVM2 22F/2.2
$\mathcal{P}_e$	*[W]*	2706
$\mathcal{P}_{mec}$	*[W]*	2200
η_{mec}	*[%]*	81.3
$U\ (\Delta)$	*[V]*	230
$I\ (\Delta)$	*[A]*	8.71
Fr	*[Hz]*	50
$\cos\varphi$		0.78
C_{em}	*[N.m]*	7.35
N	*[tr/min]*	2860
Ω	*[rad/s]*	299
R_s	*[Ω]*	2.475
R_r	*[Ω]*	4.446
L_s	*[H]*	0.2598
L_r	*[H]*	0.2703
L_m	*[H]*	0.3897
M_{sr}	*[H]*	0.2598
p		1
σ		0.038
τ_r	*[s]*	0.06
τ_s	*[s]*	0.1
J	$[kg/m^2]$	0.023
f	$[N.m.s.rd^{-1}]$	0.0026

HP pump parameters	
Type	EBARA EVM2 22F/2.2
Rated power	2200 W
Rated current	8.71 A
Rated voltage	230 V
a	0,0002317
b	-0,0005198
c	-0,002427

ANNEXE 02

« TIADS description »

1. TIADS’s schematic description:

Figure 1 illustrates the schematic of TIADS. To provide a better understanding of this system, the following description is provided:

1. Intake: a pipeline draw the salt water that enters the station's intake system, where it passes through screens to remove large debris and other particles.
2. Pre-treatment: The salt water is then subject to pre-treatment to remove suspended particles, algae, and other impurities. This stage includes processes such as sedimentation and ultrafiltration.
3. High-pressure pumps: The pre-treated water is then pumped through high-pressure pumps to increase the water's pressure.
4. Reverse osmosis (RO) system: The pressurized water enters the RO system, where it is passed through a semi-permeable membrane that filters out dissolved salts and other minerals. The membrane allows water molecules to pass through while rejecting salt and other impurities, producing clean, fresh water.
5. Post-treatment: The RO permeate is then subject to post-treatment to adjust its pH, add disinfectants such as chlorine, and remineralize the water to improve its taste and quality.
6. Distribution: The treated water is ultimately distributed to researchers for agricultural testing purposes. Among these involves, is the application of water to various plant species, such as garlic, feverfew, and black cumin, both prior to and following the process of desalination. The objective of these tests is to evaluate the impact of desalination on agricultural production.

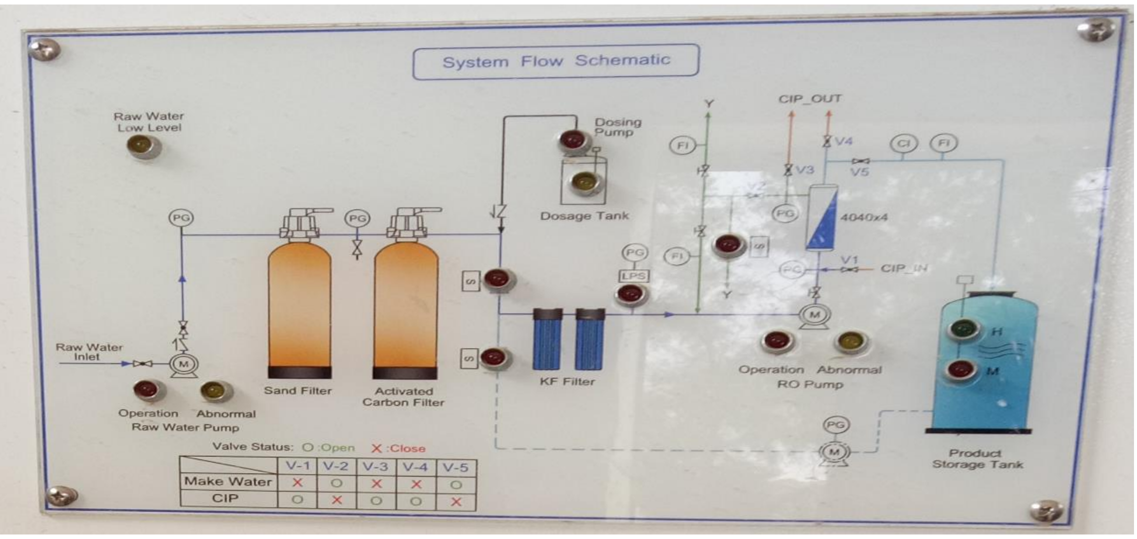

Valve Status: O :Open X :Close

	V-1	V-2	V-3	V-4	V-5
Make Water	X	O	X	X	O
CIP	O	X	O	O	X

Figure 1. System flow schematic of TIADS

2. Testing the effect of reverse osmosis treated irrigation water on leguminous and condiment crops

Figure 2 displays a photo of feverfew, garlic, and black cumin irrigated with RO-treated water, while Figure 3 illustrates the same leguminous crops irrigated with regular water.

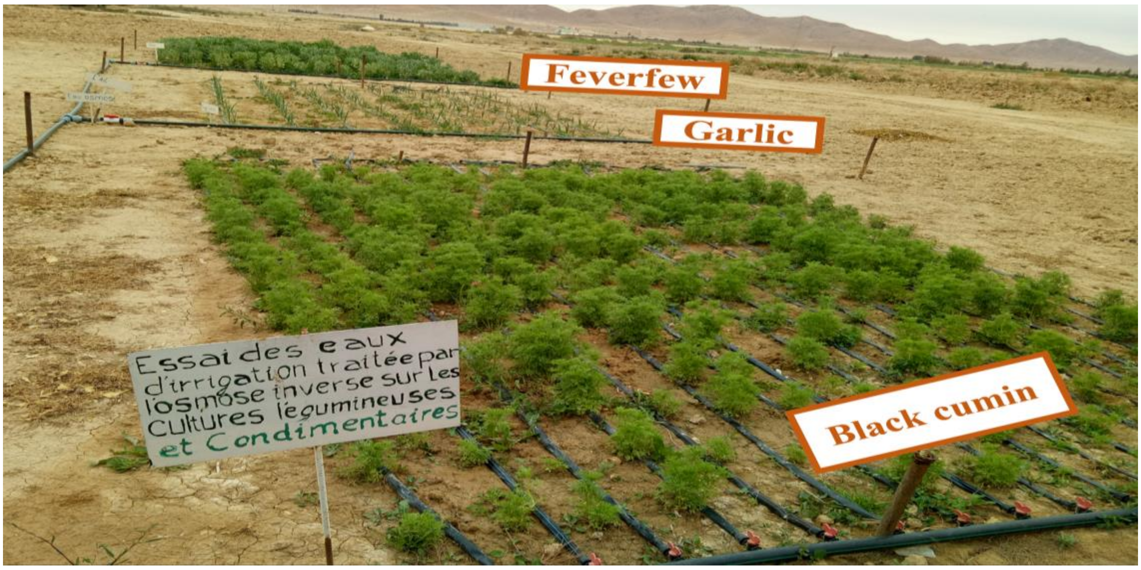

Figure 2. Feverfew, garlic, and black cumin were irrigated with RO-treated water.

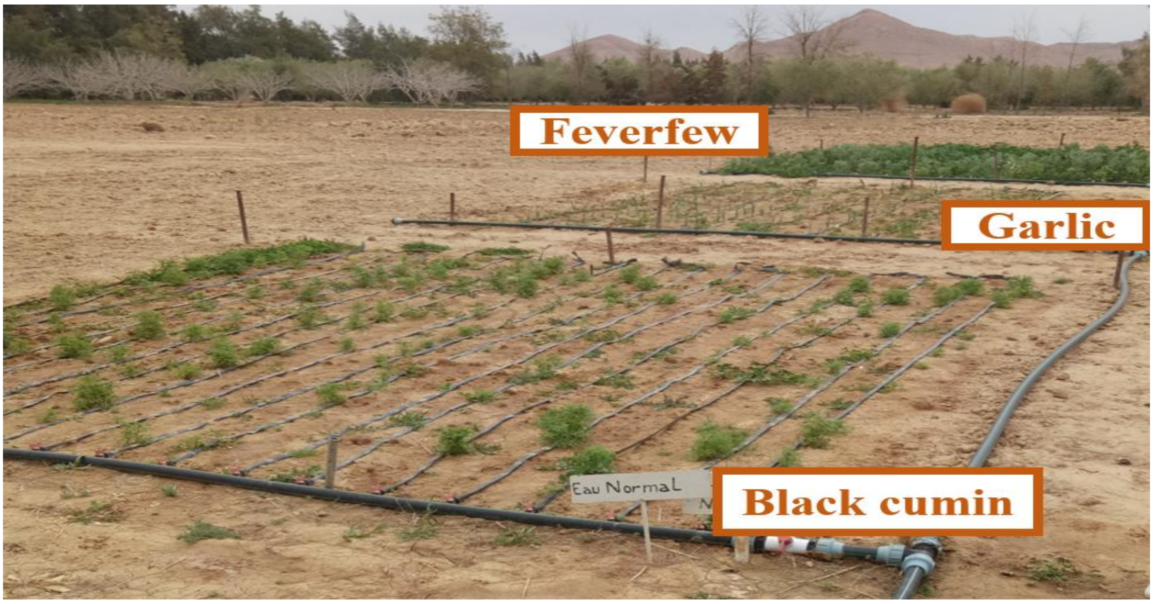

Figure 3. Feverfew, garlic, and black cumin were irrigated with normal water.

ANNEXE 03

« pump parameters»

The following figure shows the characteristic curves of the pump (H = f(Q)) for different values of the speed (157 rad/s, 100 rad/s, and 130 rad/s). The pump parameters are defined as: a=0.000218, b=0.000011, and c=-0.000046.

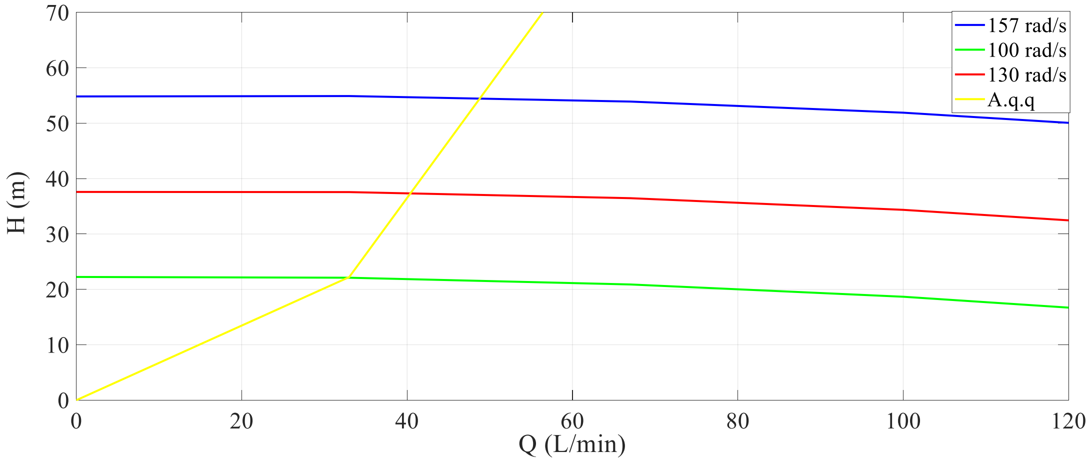

Figure 5.4: Characteristic curves of the pump.

A Toray-type membrane (TM710) was used in this work which is characterized by a feed water pressure of 1.55 MPa ($P_{fn} = 15.5$ bar), $Q_{fn} = 35.8134$ l/min a feed water temperature of $25^0 C$, a feed water concentration of 2g/l (Nacl), and recovery Rate of 15%. Under nominal conditions, the membrane exhibits the following quantities:

$$\begin{cases} P_{fn} = 15.5 \text{ bar} \\ Q_{pn} = 1.0533\ 10^{-4}\ m^3/s = 6.3198\ l/min \\ R = 15\% \\ Q_{fn} = 5.9689\ 10^{-4}\ m^3/s = 35.8134\ l/min \end{cases} \tag{5.21}$$

- ➢ Calculate nominal permeate concentration (C_{pn})

$$Y = 1 - \frac{C_{pn}}{C_{fn}} \Rightarrow \quad C_{pn} = (1 - Y)\ C_{fn} \tag{5.22}$$

Where $C_{fn} = 2000 \frac{mg}{l} (Nacl)$ and Y=99.7%

So
$$C_{pn} = 6\ mg/l \tag{5.23}$$